Saint Venant’s Torsion
by the Finite-Volume Method

A Thesis
Presented to
the Faculty of
the Department of Engineering Systems and Environment
School of Engineering and Applied Science
University of Virginia
Charlottesville, VA, 22903

In Partial Fulfillment
of the Requirements for the Degree

Master of Science
by
Heze Chen

August
2019

APPROVAL SHEET

The Thesis
is submitted in partial fulfillment of the requirements
for the degree of
Master of Science

Heze Chen

This Thesis has been read and approved by the examining committee:

Jose P. Gomez
Co-advisor

Marek-Jerzy Pindera
Co-advisor

Baoxing Xu
Chair

Accepted for the School of Engineering and Applied Science:
Craig H. Benson, Dean, School of Engineering and Applied Science

August
2019

Abstract

Torsion introduces additional shearing in the structural element's cross section, which may potentially produce failure in structures or damage their serviceability. Thus, the torsional deformation mode, characterized by the twisting of a structural element about its axis, plays an important role in structural engineering design. In this thesis, a new approach to Saint Venant's torsion problems has been developed for the first time based on the finite-volume method. The approach employs the displacement formulation expressed in terms of the warping function subject to Neumann-type boundary condition to ensure traction-free lateral surface. The finite-difference method was also implemented as a reference for comparison and validation of the developed finite-volume method. Homogenous isotropic rectangular cross sections employed in structural engineering problems were analyzed by the finite-volume and finite-difference methods and validated against exact elasticity solutions. The convergence and accuracy of the finite-volume method relative to elasticity solutions were also demonstrated for composite cross sections made up of two symmetrically joined rectangular regions filled with different materials. Three typical homogenous cross sections employed in structural engineering were then analyzed in order to assess the accuracy of the membrane analogy widely used in the design. The finite-volume method's strength lies in its superior ability to handle heterogeneous material cross sections, by inherently satisfying traction and displacement continuity conditions at the interfaces separating different materials, whereas the finite-difference method requires more refined grids to yield converged results. This strength was further demonstrated for composite cross sections with isotropic and orthotropic materials in the form of discontinuous and continuous reinforcement of concrete T-beam and box-beam cross sections. This thesis lays the foundation for the implementation of the finite-volume method in a large range of applications involving the design of composite structural elements with complex heterogeneous microstructures.

Keywords: Saint Venant's torsion; finite-volume method; finite-difference method.

Acknowledgments

I am thanking those around me who helped me through the process of pursuing my master's degree. It would have not been possible without their support and advice.

I would like to sincerely thank my co-advisors, Professor Jose Gomez and Professor Marek-Jerzy Pindera, for their continuous guidance and tremendous support during my two years as a Master of Science student at University of Virginia. My special thanks to Professor Pindera for accommodating my wife and me in his family house in Waterloo, Canada to finish this thesis.

My appreciation goes to my wife, Yiqing Xu, who gave me company, inspiration and motivation all the way for the past five years. My family also gave me great financial and spiritual support with warmth from Hangzhou, China.

To current or ex-graduate students, colleagues, friends, including Muhammad M. Sherif, Abdou K. Ndong, Seth Engel, Zhelong He, Ruoxi Xie, Mike Farnsworth, Zechen Hu, Qimin Luo, Zheng Chen, Runze Yan, Ugur Kilic, Ozer Sevim, Alphonse N. Tetteh, Savannah Washlesky, Marie Benavides, Qais Ghafari, Yipei Song, Haoyi Ma, Wanxin Cai, Xinqi Hou, Zhangfan Jiang, Syed A. Kazmi, Haddis Abebe, Daniel Anthony, I greatly appreciate all your help and good thoughts on me during my time as a graduate student. Your presence in my graduate career made for a great learning environment.

Since the techniques in this thesis were all coded in MATLAB, my contribution in this thesis cannot live without my systematic MATLAB skills learned from Dr. Ethan Young.

Last, I would like to thank the members of the examining committee for serving and providing constructive comments.

The author gratefully acknowledges the Department of Engineering Systems and Environment for providing the necessary funding and fellowship.

Contents

Chapter 1

1. Introduction

1.1. Motivation

Long structural elements such as beams may be loaded by a combination of axial and transverse loads. These loads typically produce deformations that may be separated into extension, pure bending, flexure and torsion. Under combined loading, the different deformation modes are typically analyzed separately when linear elastic analysis is applicable, and the individual contributions are summed algebraically.

In mechanics, moments created by forces that produce twisting of structural elements about their longitudinal axes are called torques or twisting moments, as opposed to bending moments that produce bending of the structural element about an axis that lies in the element's cross section. If these forces are couples, they produce self-equilibrating shear stress distributions in the structural element's cross section. Torsion is the twisting of a structural element with constant cross section, typically called a prismatic bar, when it is loaded by a torque that produces rotation of the cross section about the bar's axis as the only deformation mode. When analyzing the torsion of prismatic bars, the quantities of interest are the relationship between torque and angle of twist of the cross section, related through the torsional rigidity, and the internal stresses. The torsional rigidity is a measure of the cross-section's resistance to torsion that involves material and geometric properties discussed in Chapter 2.

Torsion of prismatic bars plays an important role in structural engineering problems. If the resistance to torsion is insufficient, torsion may cause excessive deformation resulting in failure of structural elements. For instance, in aircraft wing design, torsional rigidity is essential in ensuring limited torsional deformation and hence proper lift function. Some structural components such as shafts in power trains with circular cross sections are designed specifically for torque transmission. In others whose primary load-bearing function does not involve torsion specifically, torsion may not always be avoided and hence the torsional analysis of such members is required for safe design. For instance, torsion of beams subjected to transverse loading arises from the action of shear stress distributions which create an internal shear force whose resultant does not coincide with the shear center. This could happen when the load is applied eccentrically to a beam with T-cross section or a box-cross section, or when the cross section does not possess planes of symmetry with an easily identifiable shear center, such as a beam with channel-cross section.

The shear center is especially important for thin-walled structures since resultant loading through this center only creates pure bending, which prevents structural failure due to the torsion. Katori (2001) computed the shear center of thin-walled open/closed cross sections by the finite-element method. Romano and Barretta (2012) investigated the torsion and shear stress fields of Saint-Venant beams and evaluated its shear as well as the twist center. Barretta (2012) then investigated the relationship between twist and shear centers for orthotropic fiber-reinforced beams with homogenized elastic moduli.

Torsion introduces additional shearing in the structural component's cross section whose impact depends on material make-up. In concrete structures, the effect of shearing cannot be neglected since the strength of concrete in tension is considerably lower than its strength in compression. Shear is a dramatic, rather than ductile, failure mode in concrete beams which causes diagonal cracks that are significantly wider than flexural cracks. Shear failure mechanisms are understood but the quantitative theory is not well developed. In large concrete structure construction, torsion occurs primarily when the load acts at a perpendicular distance from the longitudinal axis of the structural member. The moments occasionally cause excessive shearing stresses due to massive cross sections. As a result, severe cracking can develop well beyond the allowable serviceability limits unless special torsional reinforcement is provided. In actual spandrel beams of a structural system, the extent of damage due to torsion is not severe, it is the redistribution of stresses in the structure that dominates the serviceability. Necessary torsional reinforcement in structural design should be taken seriously to avoid the loss of integrity. In contrast, in thin-walled metal structures widely used in the industry, additional shearing produced by torsion contributes to wall buckling, impacting stability.

1.2. A Historical Perspective and Analysis Approaches

In addition to technologically important applications involving the analysis and design of structural components that may experience twisting, the solution to elastic torsion problems occupies an important place in the theory of elasticity. Specifically, it demonstrates an important solution technique that reduces a seemingly three-dimensional elasticity problem to a two-dimensional one involving just one governing differential equation. This solution approach was first introduced by Saint Venant in 1853, and is now universally called the semi-inverse method. Saint Venant derived explicit functional forms of displacement components in the cross section of a prismatic bar loaded by pure twisting moments from geometric considerations and then, based on the argument of the constancy of the twisting torque along the bar's axis, assumed a functional form of the remaining (out-of-plane) displacement component. The proposed displacement field satisfied exactly two of the three governing equilibrium equations of elasticity. He then used the third equilibrium equation to impose a constraint on the out-of-plane displacement component that produces warping of cross sections perpendicular to the prismatic bar's longitudinal axis. This constraint took the form of Laplace equation that the out-of-plane displacement had to satisfy subject to boundary condition that ensured the bar's lateral surface is traction free. The traction-free boundary condition reduces to the statement that the normal derivative of the out-of-plane displacement is equal to a function in the cross section's in-plane coordinates that are defined by the bar's lateral boundary. Problems defined by the Laplace equation subject to the above boundary condition are known as Neumann-type potential problems and are not readily solvable using standard techniques using the real function approach.

Prandtl subsequently reformulated the torsion problem in 1903 by introducing a stress function which satisfied exactly the third equilibrium equation. Taking advantage of the Saint Venant's displacement-based formulation he then showed that the stress function must satisfy Poisson's equation. The advantage of the stress formulation is the simplification of the boundary condition to Dirichlet type where the sought function itself is taken as an arbitrary constant on the cross section's lateral boundary. This facilitates the analytical solution of torsion problems for cross sections that are circular, elliptical, equilateral triangular and rectangular. For the first three cross sections, simple analytical solutions are generated by deducing the Prandtl's stress function such that it is zero on the cross section's lateral boundary while adjusting a parameter that ensures satisfaction of the governing Poisson's equation. For rectangular cross sections, solution in the form of an infinite Fourier series is obtained that converges relatively fast with the number of harmonic terms.

The Prandtl's stress function reformulation also enables an analogy to be drawn between the torsion problem and a deflection of a pressurized flexible membrane over an opening of the same shape as the bar's cross section. The governing differential equation for the membrane problem is the same as that for the torsion problem, demonstrating the physical significance of the mathematical formulation of the latter and a means of obtaining approximate solutions. Prandtl's reformulation establishes particular relationships between the deflected surface of the pressurized membrane and the distributions of torsional stresses in a bar subjected to twisting moments known as the membrane analogy as will be discussed in Chapter 4.

Membrane analogy serves as an efficient approximation for torsion of thin-walled structures. One classical membrane analogy was presented by Prandtl showing a similarity between the geometry of membrane and torsional stress fields. The other one is a second membrane analogy involving non-pressurized membrane in terms of conjugate warping function developed by Heinrich (1996). Troyani et al. (2007) presented a selectively refining procedure based on the membrane analogy in finite-element torsional problems. Li and Easterbrook (2014) developed an elasticity-based method for torsion of open/closed thin-walled inhomogeneous structures based on membrane analogy and equilibrium and compatibility equations.

Analytical solutions to torsion problems of cross sections other than circular, elliptical, equilateral and rectangular may be obtained by re-casting the torsion problem using the complex potential approach wherein a complex potential that governs the stress field may be obtained by evaluating an integral that involves the mapping transformation of the bar's cross section in one complex plane onto a circle in another complex plane. The problem then reduces to finding the required mapping transformation. This approach has limited utility as it is limited to homogeneous prismatic bars. Moreover, mapping transformations may not be easily determined for complicated cross sections, including those with cut-outs.

Hence, numerical methods have been employed to solve torsion problems of structural members of different cross sections mentioned earlier employed in structural engineering applications. These include the finite-difference, boundary-element and finite-element methods. The finite-difference method is straightforward to use and converges relatively fast, but complications arise for cross sections with complicated lateral boundaries or cross sections made up of different materials separated by interfaces along which traction and displacement components must be continuous. The boundary-element and finite-element methods do not suffer from these shortcomings, but displacement-based variational approaches require substantial mesh refinement at interfaces separating different materials of composite cross sections in order to achieve solution convergence. This is particularly true for reinforced concrete cross sections where stress concentrations may arise at the interface boundaries between discrete reinforcement rods and the surrounding concrete matrix.

1.3. A Concise Literature Review

Due to the pioneering work of Saint Venant and Prandtl, and others who followed the semi-inverse solution strategy, the torsion problem of prismatic homogeneous bars made of isotropic materials is very-well established. It is typically discussed in a separate chapter in standard elasticity and structural mechanics books, including Timoshenko and Goodier (1970), Boresi and Schmidt (1985), Ugural and Fenster (2003) and Sadd (2009). The recent contributions to the literature have focused on prismatic bars made of anisotropic materials and composite cross sections in light of the rapid development of composite materials during the past 30 years. Mushkhelishvilli (1963) was the first to develop an exact elasticity solution for torsion of a prismatic bar with a rectangular cross section composed of two bonded isotropic rectangular parts with different shear moduli. The solution is an extension of the elasticity solution to the problem of a rectangular homogeneous cross section given in terms of an infinite Fourier series representation of the Prandtl's stress function. Savoia and Tullini (1993), followed by Swanson (1998), subsequently extended this solution to rectangular orthotropic multi-layer beams composed of rectangular sub-layers. Most recently, Teimoori et al. (2016) investigated the torsion of a rectangular cross section coated on top and bottom by thin isotropic using finite Fourier cosine transform.

The analytical approach has also been applied to torsion of circular and elliptical cross sections with anisotropic properties and cylindrical reinforcement or voids. For instance, Chen et al. (2002) derived an exact elasticity solution to the problem of a composite cylinder reinforced by a continuous inclusion or fiber, following the CCA model proposed by Hashin and Rosen (1964). Subsequently, Chen (2005) developed a theoretical framework for torsion of anisotropic composite bars and identified anisotropic elliptical bars that did not warp. Tsai and Chen (2012) subsequently generalized the solution to the CCA model containing a single fiber to accommodate a number of coated fibers. Karimi et al. (2017) developed an analytical solution in the finite Fourier sine transform for hollow cylinders with cracks in an orthotropic coating with the aid of a distribution dislocation technique.

In order to obtain solutions to torsion of cross sections with complicated shapes for which analytical solutions may not be easy to generate, finite-difference, boundary-element and finite-element methods had been employed. The finite-difference method had already been employed by Ely and Zienkiewicz (1960) to solve the Poisson's equation for arbitrary and multiply-connected cross sections with isotropic materials characterized by spatially variable or piece-wise uniform shear moduli. Continuity conditions were developed for sharp interfaces separating regions with different moduli, but the actual finite-difference implementation was not given. This is perhaps the first paper that discusses materials with spatially variable moduli, a topic of interest some twenty-five years later when functionally graded materials were first introduced and subsequently intensively investigated. Nonetheless, the finite-difference method is not typically employed to solve torsion problems involving composite or heterogeneous cross sections as suggested by the small number of publications based on this approach.

The boundary-element method appears to be employed with greater frequency than the finite-difference method in the solution of the torsion problem. Sapountzakis (2001) developed a boundary-element method for the nonuniform torsion of composite bars and applied it to the solution of two-boundary value problems. Sapountzakis and Mokos (2003) further extended the boundary-element approach to composite bar consisting of inclusions embedded in a homogeneous matrix. Tsiatas and Katsikadelis (2011) employed a microstructure-dependent couple stress model to solve a torsion problem using the direct boundary-element method.

The finite-element method is by far the most widely employed technique in the solution of torsion problems, and new approaches based on this method continue to be proposed. Xiao et al. (1999) developed a hybrid-stress finite element method based on Hellinger-Reissner principle to deal with torsion problems. Li et al. (2000) applied the finite-element approach based on Galerkin's method with additional continuity conditions to study torsional rigidity of composite bars with arbitrary shape using the warping function formulation, whereas Saygun et al. (2007) employed Prandtl's stress function in their finite-element formulation of the torsion problem. Jog and Mokashi (2014) presented a finite element formulation capable of dealing with multiply-connected compound anisotropic bars. A finite-element method based on linear and quadratic triangular elements was developed by Purnomo et al. (2018), which was capable of accommodating either homogenous or non-homogenous, anisotropic materials and arbitrary shape cross sections, in contrast with the stress function approach applicable to open cross sections composed of isotropic materials. Most recently, Beheshti (2018) proposed a finite-element approach based on strain-gradient elasticity to analyze torsion problems involving prismatic bars of very small dimensions.

Functionally graded materials became popular in recent years because their spatially variable microstructures enable to tailor and optimize structural performance to given applications, including torsion problems. Horgan (2007) proved that some anisotropic graded elliptical cross sections do not warp under pure torsion. Xu et al. (2010) derived an exact solution to torsion of an orthotropic, inhomogeneous or graded rectangular cross section where the shear modulus obeys an exponential law. Darilmaz et al. (2018)

adopted a Hellinger-Reissner based hybrid finite-element method to obtain torsional rigidity and shear stresses of composite or graded cross sections.

1.4. The Finite-Volume Method in Structural Analysis

An attractive alternative to the solution of the Saint Venant's torsion problem is offered by the finite-volume method which has gained popularity in the past thirty years. The finite-volume method is a well-established numerical technique for the solution of boundary-value problems in fluid mechanics, cf. Leveque (2002), Versteeg and Malalasekera (2007). Satisfaction of the governing (transport or equilibrium) field equations within subvolumes of the investigated discretized domain in an integral sense is a key feature of the finite-volume method which distinguishes it from variational techniques such as the finite-element method. In the context of fluid mechanics applications, this is done upon first expressing the field equations in a finite-difference form, and then extrapolating the grid point field variables to the subvolume surfaces surrounding each point to enable the required surface integration, thereby ensuring local field equation satisfaction in the integral sense.

The simplicity and demonstrated stability of the finite-volume method in fluid mechanics applications have motivated the transition of this technique to solid mechanics problems during the past 30 years as an alternative to the finite-element approach. For static elasticity-type problems, this reduces to the satisfaction of the equilibrium equations in the integral sense within subvolumes of the discretized analysis domain,

$$\int_{V_q} \left(\frac{\partial \sigma_{ji}}{\partial x_j} + F_i \right) dV_q = \int_{S_q} \sigma_{ji} n_j dS_q + \int_{V_q} F_i dV_q = 0$$

where n_j are components of the unit normal to the bounding surface S_q of the subvolume V_q, and Gauss's Theorem was employed to convert the volume integral of stress divergence to the surface integral of traction components. Three versions of this technique can be identified in the analysis of solid mechanics problems, as discussed by Cavalcante et al. (2012). These versions are characterized by different subvolume discretizations of the investigated domain and different displacement field representations within subvolumes, which lead to a different manner of approximating field variables along subvolume surfaces.

The first two approaches, known as the cell-centered and cell vertex finite-volume techniques originally developed for homogeneous materials and structures, were motivated by the established finite-volume technique for fluid mechanics problems and elements of the finite-element method. The cell-centered finite-volume method is similar to the original fluid mechanics version and employs subvolumes which are centered around grid points at which field variables are defined. Initially, structured meshes based on rectangular or cylindrical subvolumes had been used for domain discretization, which was subsequently generalized to unstructured meshes with arbitrary subvolume topology based on polyhedral shapes. The cell vertex or vertex-based, the finite-volume approach leverages elements of the finite-element method in domain discretization and displacement field approximation. The domain is first discretized into finite elements, and the common vertices of adjacent elements provide grid points at which field variables are defined using shape functions borrowed from the finite-element approach. Subvolumes centered around grid points are then constructed taking contributions from elements with common vertices and using element and face centers as subvolume corners. Thus the subvolume geometry and displacement field approximation are directly linked to element discretization and employed shape functions. Satisfaction of the local equilibrium equations is carried out over all subvolumes containing every common vertex shared by adjacent elements forming grid points. Arbitrarily shaped polygonal control volumes may thus be constructed based on the chosen element type used to mesh the analysis domain.

The third version of the finite-volume method evolved independently and nearly in parallel to model materials with heterogeneous microstructures, including periodic and functionally graded materials, cf. Suquet (1985), Charalambakis and Murat (2006), Buryachenko (2007), Birman and Byrd (2007), Chatzigeorgiou et al. (2008), and Paulino et al. (2008). The structural finite-volume theory has its origins in the so-called Higher-Order Theory for Functionally Graded Materials (HOTFGM), developed in a sequence of papers in the 1990s and summarized in Aboudi et al. (1999). This theory provided the main framework for the construction of its homogenized counterpart initially named the Higher-Order Theory for Periodic Multiphase Materials by Aboudi et al. (2001).

The structural and homogenized versions of these so-called higher-order theories were subsequently reconstructed in a sequence of papers by Bansal and Pindera (2003, 2005, 2006) and Zhong et al. (2004) by simplifying the discretization of analysis domain which, in turn, facilitated implementation of the efficient local/global stiffness matrix approach, Bufler (1971), Pindera (1991). The re-constructed theories were further extended by Cavalcante et al. (2006, 2007a,b), Gattu et al. (2008) and Khatam and Pindera (2009a,b) by incorporating parametric mapping to enable efficient modeling of complex microstructures using quadrilateral subvolumes. These significant re-constructions revealed the above higher-order approaches to be in fact finite-volume methods, which in turn motivated corresponding name changes in order to correctly reflect the fundamental character of these re-constructed theories.

The re-constructed finite-volume theories are similar to the cell-centered techniques that evolved in parallel for homogeneous materials and structures during the same time frame. However, in contrast with the early cell-centered techniques, the re-constructed theories employ explicit displacement field approximation within individual subvolumes, and follow an elasticity-based approach in satisfying interfacial displacement and traction continuity conditions in a surface-averaged sense. This is consistent with the satisfaction of equilibrium equations in a surface-averaged sense and leads to an explicit construction of local stiffness matrices for individual subvolumes which, in turn, substantially reduces the number of unknown variables, and allows direct comparison with the finite-element method. Assembly of local stiffness matrices into the global stiffness matrix is then performed such that continuity of surface-averaged tractions and displacements is satisfied. The satisfaction of both traction and displacement continuity across subvolume faces produces a robust solution technique that naturally accommodates heterogeneous material microstructures.

A review of the finite-volume method in solid mechanics applications has been recently provided by Cardiff and Demirdzic (2019). While the method has been used extensively in the solution of plane problems in structural mechanics, including contact and crack problems, there appear to be no papers that address the use of the finite-volume method in the solution of Saint Venant's torsion problems. The present thesis fills this void and provides a powerful alternative to the wide-spread use of variational techniques for this class of problems.

1.5. Objectives

The main objective of this thesis is to demonstrate the utility of the finite-volume approach in the solution of Saint Venant's torsion problems of prismatic bars of arbitrary cross section and composition. Hence the finite-volume theory developed by Pindera and co-workers is extended to the solution of torsion problems of structural components of different shapes, and employed to demonstrate its utility in structural engineering applications. The extension is carried out to accommodate prismatic bars with both homogeneous and composite cross sections. Arbitrary cross sections bounded by surfaces that are parallel to the Cartesian coordinate axes are most easily accommodated by the extension since the version of the finite-volume method based on rectangular subvolume discretization of the analyzed domain, first developed by Bansal and Pindera (2003), is employed. Hence cross sections of structural components such as T-beams, box-beams or channel-beams that are either homogeneous or composite may be analyzed, including beams reinforced by continuous inserts.

The displacement-based formulation is employed in constructing the solution methodology by adopting the elasticity-based results in approximating the functional form of the displacement field in individual subvolumes. A finite-difference solution approach is also developed for validating the extended theory in the analysis of homogeneous cross sections for which analytical solutions are not available. The finite-difference solution approach involves both displacement-based and stress-based formulations.

1.6. Thesis Outline

The thesis is organized as follows. The extension of the finite-volume technique to the solution of Saint Venant's torsion problems is described in Chapter 2. The theory is validated in Chapter 3 using known elasticity solutions for homogeneous and composite rectangular cross sections, and compared with the accuracy and performance of the finite-difference solution for homogeneous cross sections. Chapter 4 presents results for typical homogeneous cross sections employed in structural engineering applications, including T-beams, box-beams and channel-beams, and examines the accuracy of the membrane analogy in analyzing these cross sections. Composite cross sections are analyzed in Chapter 5, including cross sections reinforced with thin wraps and graded cross sections. The main contributions and conclusions of this investigation are summarized in Chapter 6.

Chapter 2

2. Saint Venant's Torsion Problem

2.1. Introduction

A new finite-volume based approach to the solution of Saint Venant's torsion problems of homogeneous and composite prismatic bars subjected to pure torsion is developed in this chapter. The approach leverages the elasticity formulation of the torsion problem based on the Saint Venant's semi-inverse method which provides the correct displacement field approximation within the rectangular subvolumes of the beam's discretized cross section. The remaining governing differential equation for the warping function is then locally satisfied in each subvolume in a surface-average sense, enabling the construction of the local stiffness matrix that relates surface-averaged displacements to surface-averaged tractions on the subvolume's boundaries. Orthotropic subvolumes are admitted in the formulation to enable analysis of prismatic bars reinforced with composite materials or bars made up of composite cross sections. Continuity of both displacements and tractions across subvolumes' interfaces is satisfied in a surface-average sense, together with the traction-free lateral boundary conditions, upon the construction of the global stiffness matrix whose solution determines the local stress fields, torque-twist angle relationship and hence the cross section's torsional rigidity.

The remainder of this chapter is structured as follows. Section 2.2 provides an overview of Saint Venant's torsion problem based on the semi-inverse method. The torsion problem is first formulated in terms of displacements and the warping function in order to provide a foundation for parallel formulation and solution strategy based on the finite-volume method. Then the torsion problem is reformulated in terms of the Prandtl's stress function in Section 2.3. The stress formulation facilitates the development of closed-form solutions to several important cross sections of homogeneous and to lesser extent composite bars. One such solution is employed in Chapter 3 in validating the displacement-based finite-volume solution methodology developed subsequently in Section 2.4. For comparison with the finite-volume solution to the torsion problem, finite-difference solutions are also developed in Section 2.5. Both displacement-based and stress function approaches are developed for comparison with finite-volume solutions of homogeneous and composite cross sections. Summary and discussion of the developed solution strategies are provided in Section 2.6.

2.2. Displacement Formulation and Warping Function

Analysis of the deformation of a prismatic bar subjected to pure twisting moments along the z axis in the $x-y$ plane situated at an arbitrary elevation z from the face relative to which the relative rotation angle of the cross section is measured, Fig. (2.1), produces the displacement components u and v in the form

$$u(y,z) = -\theta yz, \qquad v(x,z) = \theta xz \tag{2.1}$$

where θ is the angle of twist of the cross section per unit length along the bar's axis.

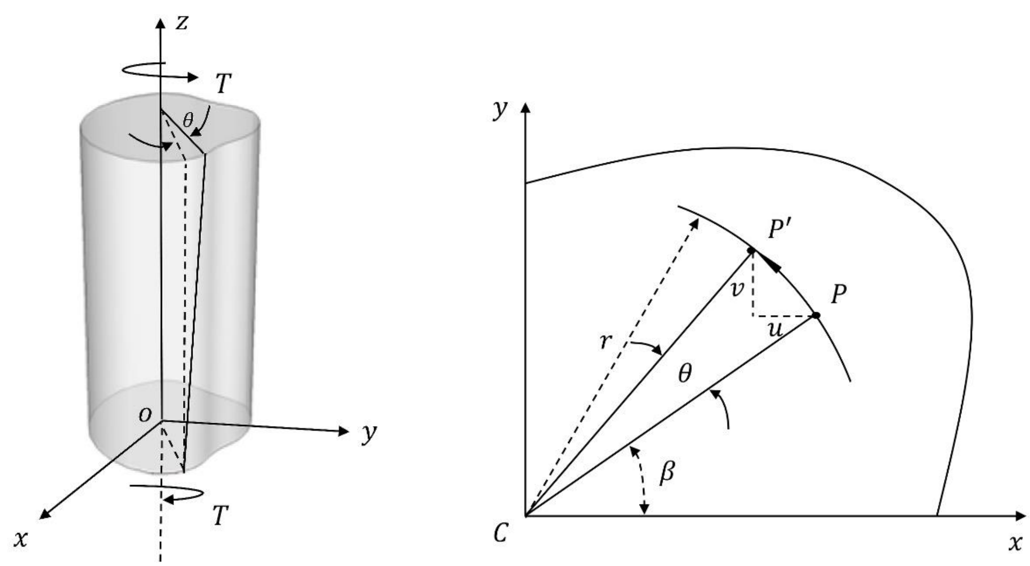

Figure 2.1. Saint Venant's torsion problem showing the deformation of planes passing through the prismatic bar's centroidal axis due to twisting moment applied to the end faces (left), and the displacement of a material point in the plane orthogonal to the bar's axis (right).

Eq. (2.1) is based on the assumption of infinitesimal in-plane deformations employed in the kinematic analysis and the fact that the torsional center of the cross sections at any elevation does not displace in x or y direction. Each cross section rotates as a rigid body about the same axis, since the in-plane projection of the cross section in the deformed configuration has the exact same shape as that of the undeformed cross section implied by the above two equations. The remaining out-of-plane displacement component w, which characterizes the cross-section's warping, is then assumed to depend only on the in-plane coordinates (x, y) because the twisting moment does not vary along the bar's axis. It is expressed in terms of the warping function ψ as follows

$$w = \theta\psi(x, y) \tag{2.2}$$

where θ has been included for consistency with the in-plane displacement field.

The above displacement field produces vanishing normal and transverse shear strains, namely $\varepsilon_{xx} = \varepsilon_{yy} = \varepsilon_{zz} = 0$ and $\gamma_{xy} = 0$. The surviving strains are those shear strains that occur in the planes which contain the z axis, namely $x - z$ and $y - z$ planes.

$$\gamma_{yz} = \frac{\partial w}{\partial y} + x\theta, \qquad \gamma_{xz} = \frac{\partial w}{\partial x} - y\theta \tag{2.3}$$

Consequently, assuming isotropic cross section the normal and transverse shear stresses vanish, $\sigma_{xx} = \sigma_{yy} = \sigma_{zz} = 0$ and $\sigma_{xy} = 0$, and the only stresses that survive are the shear stresses in the above two planes. Using Hooke's law, the corresponding non-vanishing shear stress components are then,

$$\sigma_{yz} = G\theta\left(\frac{\partial\psi}{\partial y} + x\right), \qquad \sigma_{xz} = G\theta\left(\frac{\partial\psi}{\partial x} - y\right) \tag{2.4}$$

This stress field satisfies exactly the first two equilibrium equations

$$\begin{gathered}\frac{\partial\sigma_{xx}}{\partial x} + \frac{\partial\sigma_{xy}}{\partial y} + \frac{\partial\sigma_{xz}}{\partial z} = 0\\ \frac{\partial\sigma_{xy}}{\partial x} + \frac{\partial\sigma_{yy}}{\partial y} + \frac{\partial\sigma_{yz}}{\partial z} = 0\end{gathered} \tag{2.5}$$

$$\frac{\partial \sigma_{xz}}{\partial x} + \frac{\partial \sigma_{yz}}{\partial y} + \frac{\partial \sigma_{zz}}{\partial z} = 0$$

with the third equation reducing to

$$\frac{\partial \sigma_{xz}}{\partial x} + \frac{\partial \sigma_{yz}}{\partial y} = 0 \tag{2.6}$$

which, based on the stresses in Eq. (2.4), produces the condition on $\psi(x, y)$

$$\frac{\partial^2 \psi}{\partial x^2} + \frac{\partial^2 \psi}{\partial y^2} = 0 \tag{2.7}$$

This equation is solved subject to the traction-free boundary condition on the prismatic bar's lateral surface

$$t_z = \sigma_{xz} cos(n, x) + \sigma_{yz} cos(n, y) = 0 \tag{2.8}$$

where n is the normal axis to the cross-section's boundary, and x,y are local Cartesian coordinates parallel to the fixed coordinate system centered at the centroid of the cross section. The components of the unit normal to the lateral boundary can be expressed in terms of the normal derivatives of the local boundary Cartesian coordinates,

$$n_x = \cos(n, x) = \frac{dx}{dn}$$

$$n_y = \cos(n, y) = \frac{dy}{dn}$$

Using the above relations in Eq. (2.8) the traction-free boundary condition is then expressed in terms of the normal derivative of $\psi(x, y)$ on the lateral boundary,

$$\frac{d\psi}{dn} = y\frac{dx}{dn} - x\frac{dy}{dn} \tag{2.9}$$

Once the solution for $\psi(x, y)$ is obtained for a given cross section, the angle of twist per unit length θ may be related to the resulting torque produced by the shear stresses σ_{xz} and σ_{yz},

$$T = \iint \left(\sigma_{yz} x - \sigma_{xz} y\right) dA \tag{2.10}$$

2.3. Stress Formulation and Prandtl's Stress Function

The torsion problem may be reformulated in terms of stresses by noting that the surviving third equilibrium equation, see Eq. (2.6), is exactly satisfied by the potential function $\phi(x, y)$ called Prandtl's stress function defined by,

$$\sigma_{xz} = \frac{\partial \phi}{\partial y}, \qquad \sigma_{yz} = -\frac{\partial \phi}{\partial x} \tag{2.11}$$

Using these definitions in the expressions for the two stress components expressed in terms of $\psi(x, y)$, Eq. (2.4), differentiating appropriately and adding the two equations we obtain the governing differential equation for $\phi(x, y)$

$$\frac{\partial^2 \phi}{\partial x^2} + \frac{\partial^2 \phi}{\partial y^2} = -2G\theta \tag{2.12}$$

with the corresponding boundary condition on ϕ

$$\phi(x, y) = constant \text{ on } x, y \in S \tag{2.13}$$

The boundary condition is thus simplified at the expense of a slight complication in the governing differential equation. However, because the shear stress resultant is tangent to the family of lines $\phi(x, y) = constant$, the traction-free boundary condition may be used to construct closed-form potential functions $\phi(x, y)$ using simple polynomials for circular, elliptical and equilateral triangle cross sections through appropriate choice of the constant that defines the boundary. For solid rectangular cross sections, $\phi(x, y)$ is constructed using an infinite Fourier series representation.

The construction of $\phi(x, y)$ leads to the torque-angle of twist relationship directly in terms of the potential function itself,

$$T = 2 \iint \phi(x, y) dA \tag{2.14}$$

2.4. Finite Volume Formulation and Solution

The displacement-based formulation is employed to construct the finite-volume method (FVM) for the torsion problem of cross sections of arbitrary shape and composition. Towards this end, the same global coordinate system (x, y, z) is used as that employed in the elasticity solution, which is centered at the cross section's centroid with the coordinate z along the prismatic bar's axis, and the coordinates x and y in the bar's cross section. It is necessary to use the same global coordinate system in order to correctly capture the stress field that arises from the application of the pure twisting moment. This contrasts with the previous constructions of the finite-volume theory employed in the analyses of functionally graded and periodic materials. The cross section is then discretized into (α, β) subvolumes, Fig. (2.2), with $\alpha = 1, \ldots N_\alpha$, $\beta = 1, \ldots N_\beta$ along the x and y directions, such that the local subvolume dimensions (h_α, l_β) sum up to the overall cross section's dimensions H and L, where

$$H = \sum_{\alpha=1}^{N_\alpha} h_\alpha, \qquad L = \sum_{\beta=1}^{N_\beta} l_\beta \tag{2.15}$$

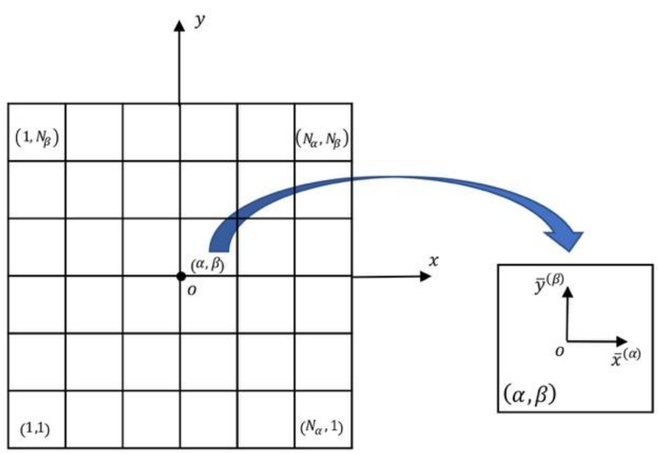

Figure 2.2. A view of 6×6 subvolumes with indices for four corner subvolumes.

In order to approximate the displacement field in each subvolume, local coordinate systems $(\bar{x}^{(\alpha)}, \bar{y}^{(\beta)})$ are set up at the subvolumes' centers in the bar's cross section, where the coordinates $(\bar{x}^{(\alpha)}, \bar{y}^{(\beta)})$ of an arbitrary point within the subvolume (α, β) relative to the global coordinate system are given by $x^{(\alpha)} = x_o^{(\alpha)} + \bar{x}^{(\alpha)}$ and $y^{(\beta)} = y_o^{(\beta)} + \bar{y}^{(\beta)}$, and the subvolume centers are

$$x_o^{(\alpha)} = \left(\alpha - \frac{1}{2} - \frac{N_\alpha}{2}\right) h_\alpha, \qquad y_o^{(\beta)} = (\beta - \frac{1}{2} - \frac{N_\beta}{2}) l_\beta \tag{2.16}$$

The exact expressions for the displacement components in the bar's cross section along the x and y directions given by (2.1) are then expressed in the (α, β) subvolume in terms of the local coordinates,

$$u^{(\alpha,\beta)} = -\theta(y_o^{(\beta)} + \bar{y}^{(\beta)})z, \qquad v^{(\alpha,\beta)} = \theta(x_o^{(\alpha)} + \bar{x}^{(\alpha)})z \tag{2.17}$$

whereas the out-of-plane component is approximated in each subvolume using a second-order expansion in the local coordinates by

$$\begin{aligned} w^{(\alpha,\beta)} &= W_{(00)}^{(\alpha,\beta)} + \bar{x}^{(\alpha)} W_{(10)}^{(\alpha,\beta)} + \bar{y}^{(\beta)} W_{(01)}^{(\alpha,\beta)} \\ &\quad + \frac{1}{2}\left(3\left(\bar{x}^{(\alpha)}\right)^2 - \frac{h_\alpha^2}{4}\right) W_{(20)}^{(\alpha,\beta)} + \frac{1}{2}\left(3\left(\bar{y}^{(\beta)}\right)^2 - \frac{l_\beta^2}{4}\right) W_{(02)}^{(\alpha,\beta)} \end{aligned} \tag{2.18}$$

Using the strain-displacement relations, the above displacement field representation produces two non-zero out-of-plane shear strains expressed in terms of the unknown coefficients $W_{(mn)}^{(\alpha,\beta)}$ and the applied loading θ

$$\begin{aligned} \epsilon_{xz}^{(\alpha,\beta)} &= \frac{1}{2}\left(\frac{\partial w^{(\alpha,\beta)}}{\partial \bar{x}^{(\alpha)}} + \frac{\partial u^{(\alpha,\beta)}}{\partial z}\right) \\ &= \frac{1}{2}\left[W_{(10)}^{(\alpha,\beta)} + 3\bar{x}^{(\alpha)} W_{(20)}^{(\alpha,\beta)} - \theta\left(y_o^{(\beta)} + \bar{y}^{(\beta)}\right)\right] \\ \epsilon_{yz}^{(\alpha,\beta)} &= \frac{1}{2}\left(\frac{\partial w^{(\alpha,\beta)}}{\partial \bar{y}^{(\beta)}} + \frac{\partial v^{(\alpha,\beta)}}{\partial z}\right) \\ &= \frac{1}{2}\left[W_{(01)}^{(\alpha,\beta)} + 3\bar{y}^{(\beta)} W_{(02)}^{(\alpha,\beta)} + \theta\left(x_o^{(\alpha)} + \bar{x}^{(\alpha)}\right)\right] \end{aligned} \tag{2.19}$$

For wide-ranging applicability, cross sections comprised of linear elastic orthotropic materials are admitted in the formulation. For this class of materials, the relationship between stresses and strains in each subvolume is given by the generalized based on Hooke's Law referred to the principal material coordinate system,

$$\begin{bmatrix}\sigma_{zz}\\ \sigma_{xx}\\ \sigma_{yy}\\ \sigma_{xy}\\ \sigma_{yz}\\ \sigma_{xz}\end{bmatrix}^{(\alpha,\beta)} = \begin{bmatrix}C_{11} & C_{12} & C_{13} & 0 & 0 & 0\\ C_{12} & C_{22} & C_{23} & 0 & 0 & 0\\ C_{13} & C_{23} & C_{33} & 0 & 0 & 0\\ 0 & 0 & 0 & C_{44} & 0 & 0\\ 0 & 0 & 0 & 0 & C_{55} & 0\\ 0 & 0 & 0 & 0 & 0 & C_{66}\end{bmatrix}^{(\alpha,\beta)} \begin{bmatrix}\epsilon_{zz}\\ \epsilon_{xx}\\ \epsilon_{yy}\\ 2\epsilon_{xy}\\ 2\epsilon_{yz}\\ 2\epsilon_{xz}\end{bmatrix}^{(\alpha,\beta)} \tag{2.20}$$

Thus in the case of torsional loading, the material response of each subvolume is characterized by the shear moduli $C_{55}^{(\alpha,\beta)}$ and $C_{66}^{(\alpha,\beta)}$ in the $y-z$ and $x-z$ plane, respectively, that may vary from subvolume to subvolume. Hence the two non-zero shear stress components in these planes in each subvolume are expressed in terms of the unknown coefficients $W_{(mn)}^{(\alpha,\beta)}$ as follows,

$$\begin{aligned}\sigma_{xz}^{(\alpha,\beta)} &= C_{66}^{(\alpha,\beta)}\left[W_{(01)}^{(\alpha,\beta)} + 3\bar{y}^{(\beta)}W_{(02)}^{(\alpha,\beta)} + \theta\left(x_o^{(\alpha)} + \bar{x}^{(\alpha)}\right)\right]\\ \sigma_{yz}^{(\alpha,\beta)} &= C_{55}^{(\alpha,\beta)}\left[W_{(10)}^{(\alpha,\beta)} + 3\bar{x}^{(\alpha)}W_{(20)}^{(\alpha,\beta)} - \theta\left(y_o^{(\beta)} + \bar{y}^{(\beta)}\right)\right]\end{aligned} \tag{2.21}$$

2.4.1. Local Stiffness Matrix

The unknown coefficients $W_{(mn)}^{(\alpha,\beta)}$ in the out-of-plane displacement representation in Eq. (2.18) may be determined by satisfying displacement and traction continuity conditions between adjacent subvolumes, the external traction-free boundary conditions on the lateral surface of the bar's cross section, and the remaining equilibrium equation that ensures the equilibrium of each subvolume. These equations are satisfied in a surface-average and/or volume-average sense. Hence given $N_\alpha \times N_\beta$ subvolumes, each containing 5 unknown coefficients in the out-of-plane displacement representation, $5N_\alpha \times N_\beta$ equations are needed. Along each row, there are two traction and displacement continuity conditions that are imposed on common vertical interfaces separating adjacent subvolumes for a total of $N_\beta \times 2 \times (N_\alpha - 1)$ equations. Similarly, proceedings along each column we have $N_\alpha \times 2 \times (N_\beta - 1)$ equations. Finally, there are $(2 \times N_\alpha + 2 \times N_\beta)$ boundary subvolumes with as many external surfaces. Finally, one equilibrium equation needs to be satisfied in each subvolume for the total of $N_\alpha \times N_\beta$ additional equations. Summing up these equations, we obtain the required number of $5N_\alpha \times N_\beta$ equations.

The number of unknowns, and hence equations, may be reduced by almost 50% for cross sections discretized into a large number of subvolumes by reformulating the problem in terms of surface-averaged displacements on the four faces of each subvolume. This reformulation is convenient because of the surface-averaging approach employed in satisfying both the interfacial continuity conditions and the equilibrium of the (α,β) subvolume. Towards this end, we construct a local stiffness matrix for each subvolume by relating the surface-averaged tractions to the corresponding surface-averaged displacements. We start by defining the surface-averaged displacements as follows,

$$\hat{w}^{\pm1(\alpha,\beta)} = \frac{1}{l_\beta}\int_{-\frac{l_\beta}{2}}^{\frac{l_\beta}{2}} w^{\pm1(\alpha,\beta)}\,(\pm\frac{h_\alpha}{2},\bar{y}^{(\beta)})d\bar{y}^{(\beta)} \tag{2.22}$$

$$\hat{w}^{\pm2(\alpha,\beta)} = \frac{1}{h_\alpha}\int_{-\frac{h_\alpha}{2}}^{\frac{h_\alpha}{2}} w^{\pm2(\alpha,\beta)}\,(\bar{x}^{(\alpha)},\pm\frac{l_\beta}{2})d\bar{x}^{(\alpha)} \tag{2.23}$$

Using Eq. (2.18), the surface-averaged interfacial displacements are obtained in terms of the unknown variables $W_{(mn)}^{(\alpha,\beta)}$

$$\hat{w}^{\pm1(\alpha,\beta)} = W_{(00)}^{(\alpha,\beta)} \pm \frac{h_\alpha}{2} W_{(10)}^{(\alpha,\beta)} + \frac{h_\alpha^2}{4} W_{(20)}^{(\alpha,\beta)} \tag{2.24}$$

$$\hat{w}^{\pm2(\alpha,\beta)} = W_{(00)}^{(\alpha,\beta)} \pm \frac{l_\beta}{2} W_{(01)}^{(\alpha,\beta)} + \frac{l_\beta^2}{4} W_{(02)}^{(\alpha,\beta)} \tag{2.25}$$

Hence, the first and second-order coefficients $W_{(mn)}^{(\alpha,\beta)}$ can be expressed in terms of the surface-averaged displacements and the zero-order coefficient.

$$\begin{aligned} W_{(10)}^{(\alpha,\beta)} &= \frac{1}{h_\alpha^{(\alpha,\beta)}}\left(\hat{w}^{+1(\alpha,\beta)} - \hat{w}^{-1(\alpha,\beta)}\right) \\ W_{(01)}^{(\alpha,\beta)} &= \frac{1}{l_\beta^{(\alpha,\beta)}}\left(\hat{w}^{+2(\alpha,\beta)} - \hat{w}^{-2(\alpha,\beta)}\right) \end{aligned} \tag{2.26}$$

$$W_{(20)}^{(\alpha,\beta)} = \frac{2}{\left(h_\alpha^{(\alpha,\beta)}\right)^2}\left(\widehat{w}^{+1^{(\alpha,\beta)}} + \widehat{w}^{-1^{(\alpha,\beta)}}\right) - \frac{4W_{(00)}^{(\alpha,\beta)}}{\left(h_\alpha^{(\alpha,\beta)}\right)^2}$$

$$W_{(02)}^{(\alpha,\beta)} = \frac{2}{\left(l_\beta^{(\alpha,\beta)}\right)^2}\left(\widehat{w}^{+2^{(\alpha,\beta)}} + \widehat{w}^{-2^{(\alpha,\beta)}}\right) - \frac{4W_{(00)}^{(\alpha,\beta)}}{\left(l_\beta^{(\alpha,\beta)}\right)^2}$$

Similarly, surface-averaged interfacial tractions are defined as follows,

$$\hat{t}_z^{\pm1^{(\alpha,\beta)}} = \frac{1}{l_\beta}\int_{-\frac{l_\beta}{2}}^{\frac{l_\beta}{2}} t_z^{\pm1^{(\alpha,\beta)}}\left(\pm\frac{h_\alpha}{2}, \bar{y}^{(\beta)}\right) d\bar{y}^{(\beta)} \tag{2.27}$$

$$\hat{t}_z^{\pm2^{(\alpha,\beta)}} = \frac{1}{h_\alpha}\int_{-\frac{h_\alpha}{2}}^{\frac{h_\alpha}{2}} t_z^{\pm2^{(\alpha,\beta)}}\left(\bar{x}^{(\alpha)}, \pm\frac{l_\beta}{2}\right) d\bar{x}^{(\alpha)} \tag{2.28}$$

where the traction vector associated with a surface characterized by the unit normal vector $\boldsymbol{n}$ is $t_i^{n^{(\alpha,\beta)}} = \sigma_{ji}^{(\alpha,\beta)} n_j^{(\alpha,\beta)}$. The superscripts ±1 and ±2 in the above definitions are associated with the positive and negative faces with the unit normal vector along the $\bar{x}^{(\alpha)}$ and $\bar{y}^{(\beta)}$ axes, respectively. Hence the traction vector on any of the four subvolume faces becomes, in terms of the two out-of-plane stress shear components,

$$t_z^{n^{(\alpha,\beta)}} = \sigma_{zz}^{(\alpha,\beta)} n_z^{(\alpha,\beta)} + \sigma_{xz}^{(\alpha,\beta)} n_x^{(\alpha,\beta)} + \sigma_{yz}^{(\alpha,\beta)} n_y^{(\alpha,\beta)} \tag{2.29}$$

which may be expressed in terms of the corresponding shear strains

$$t_z^{n^{(\alpha,\beta)}} = 2C_{66}^{(\alpha,\beta)} \epsilon_{xz}^{(\alpha,\beta)} n_x^{(\alpha,\beta)} + 2C_{55}^{(\alpha,\beta)} \epsilon_{yz}^{(\alpha,\beta)} n_y^{(\alpha,\beta)} \tag{2.30}$$

Using the strain-displacement relation, Eq. (2.19), and performing surface averaging on each of the four subvolume faces, the corresponding surface-averaged tractions are obtained in terms of the unknown first and second-order coefficients $W_{(mn)}^{(\alpha,\beta)}$ as follows,

$$\hat{t}_z^{\pm 1(\alpha,\beta)} = C_{66}^{(\alpha,\beta)}\left[\pm W_{(10)}^{(\alpha,\beta)} + (\frac{3h_\alpha}{2})W_{(20)}^{(\alpha,\beta)} \mp \theta y_o^{(\beta)}\right]$$

$$\hat{t}_z^{\pm 2(\alpha,\beta)} = C_{55}^{(\alpha,\beta)}\left[\pm W_{(01)}^{(\alpha,\beta)} + \left(\frac{3l_\beta}{2}\right)W_{(02)}^{(\alpha,\beta)} \pm \theta x_o^{(\alpha)}\right] \tag{2.31}$$

These traction equations are then expressed in terms of the surface-averaged interfacial displacements and the remaining unknown coefficient $W_{(00)}^{(\alpha,\beta)}$ through the use of Eq. (2.26). Therefore, we have,

$$\hat{t}_z^{+1(\alpha,\beta)} = C_{66}^{(\alpha,\beta)}\left[(4\hat{w}^{+1(\alpha,\beta)} + 2\hat{w}^{-1(\alpha,\beta)} - 6W_{(00)}^{(\alpha,\beta)})/h_\alpha - \theta y_o^{(\beta)}\right]$$

$$\hat{t}_z^{-1(\alpha,\beta)} = C_{66}^{(\alpha,\beta)}\left[(2\hat{w}^{+1(\alpha,\beta)} + 4\hat{w}^{-1(\alpha,\beta)} - 6W_{(00)}^{(\alpha,\beta)})/h_\alpha + \theta y_o^{(\beta)}\right]$$

$$\hat{t}_z^{+2(\alpha,\beta)} = C_{55}^{(\alpha,\beta)}\left[(4\hat{w}^{+2(\alpha,\beta)} + 2\hat{w}^{-2(\alpha,\beta)} - 6W_{(00)}^{(\alpha,\beta)})/l_\beta + \theta x_o^{(\beta)}\right] \tag{2.32}$$

$$\bar{t}_z^{-2(\alpha,\beta)} = C_{55}^{(\alpha,\beta)}\left[(2\hat{w}^{+2(\alpha,\beta)} + 4\hat{w}^{-2(\alpha,\beta)} - 6W_{(00)}^{(\alpha,\beta)})/l_\beta - \theta x_o^{(\beta)}\right]$$

The last step in the construction of the local stiffness matrix is to express the remaining unknown coefficient $W_{(00)}^{(\alpha,\beta)}$ in terms of the four interfacial surface-averaged displacements associated with the (α,β) subvolume. The surface tractions associated with each face of the (α,β) subvolume are related to each other through the equilibrium equation satisfied in a volume-average sense. Using the Gauss Theorem, the equilibrium equation may be expressed in terms of surface averaging of the traction components,

$$\int\left(\frac{\partial\sigma_{xz}}{\partial x} + \frac{\partial\sigma_{yz}}{\partial y}\right)^{(\alpha,\beta)} dv^{(\alpha,\beta)} = \int\left(\sigma_{xz}n_x + \sigma_{yz}n_y\right)^{(\alpha,\beta)} ds^{(\alpha,\beta)} = 0 \tag{2.33}$$

or, in terms of the traction component $t_z^{(\alpha,\beta)}$,

$$\int t_z^{(\alpha,\beta)}\, ds^{(\alpha,\beta)} = 0$$

Integrating over the (α,β) subvolume faces, the above equilibrium equation becomes,

$$l_\beta\left(\hat{t}_z^{+1^{(\alpha,\beta)}}+\hat{t}_z^{-1^{(\alpha,\beta)}}\right)+h_\alpha\left(\hat{t}_z^{+2^{(\alpha,\beta)}}+\hat{t}_z^{-2^{(\alpha,\beta)}}\right)=0 \tag{2.34}$$

Using the expressions for the surface-averaged tractions in terms of the surface-averaged interfacial displacements and the remaining unknown coefficient, Eq. (2.32), the above equilibrium equation yields the zero-order coefficient solely in terms of the surface-averaged displacements,

$$\begin{aligned} W_{(00)}^{(\alpha,\beta)} &= \frac{C_{66}^{(\alpha,\beta)} l_\beta^2}{2C_{66}^{(\alpha,\beta)} l_\beta^2 + 2C_{55}^{(\alpha,\beta)} h_\alpha^2}\left(\widehat{w}^{+1^{(\alpha,\beta)}}+\widehat{w}^{-1^{(\alpha,\beta)}}\right) \\ &\quad + \frac{C_{55}^{(\alpha,\beta)} h_\alpha^2}{2C_{66}^{(\alpha,\beta)} l_\beta^2 + 2C_{55}^{(\alpha,\beta)} h_\alpha^2}\left(\widehat{w}^{+2^{(\alpha,\beta)}}+\widehat{w}^{-2^{(\alpha,\beta)}}\right) \end{aligned} \tag{2.35}$$

Hence the four surface-averaged tractions in Eq. (2.32) are expressed solely in terms of the corresponding surface-averaged displacements, which may be related through the local stiffness matrix,

$$\begin{bmatrix} \hat{t}_z^{+1} \\ \hat{t}_z^{-1} \\ \hat{t}_z^{+2} \\ \hat{t}_z^{-2} \end{bmatrix}^{(\alpha,\beta)} = \begin{bmatrix} L_{11} & L_{12} & L_{13} & L_{14} \\ L_{21} & L_{22} & L_{23} & L_{24} \\ L_{31} & L_{32} & L_{33} & L_{34} \\ L_{41} & L_{42} & L_{43} & L_{44} \end{bmatrix}^{(\alpha,\beta)} \begin{bmatrix} \widehat{w}^{+1} \\ \widehat{w}^{-1} \\ \widehat{w}^{+2} \\ \widehat{w}^{-2} \end{bmatrix}^{(\alpha,\beta)} + \begin{bmatrix} -C_{66}^{(\alpha,\beta)} y_o^{(\beta)} \\ C_{66}^{(\alpha,\beta)} y_o^{(\beta)} \\ C_{55}^{(\alpha,\beta)} x_o^{(\alpha)} \\ -C_{55}^{(\alpha,\beta)} x_o^{(\alpha)} \end{bmatrix} \theta \tag{2.36}$$

where the elements $L_{ij}^{(\alpha,\beta)}$ are given explicitly in terms of subvolume moduli and geometry in Appendix A in closed form.

2.4.2. Global Stiffness Matrix

The solution for the unknown surface-averaged displacements is obtained by constructing a system of equations such that the interfacial displacement and traction continuity conditions are satisfied together with the traction-free boundary conditions. Towards this end, proceeding along each row across adjacent (α,β) and $(\alpha+1,\beta)$ subvolumes, and along each column across adjacent (α,β) and $(\alpha,\beta+1)$ subvolumes, the vertical and horizontal surface-averaged interfacial displacements, respectively, are set to common values at the common interfaces.

$$\widehat{w}^{+1(\alpha,\beta)} = \widehat{w}^{-1(\alpha+1,\beta)} = \widehat{w}^{1(\alpha+1,\beta)} \tag{2.37}$$

$$\widehat{w}^{+2(\alpha,\beta)} = \widehat{w}^{-2(\alpha,\beta+1)} = \widehat{w}^{2(\alpha,\beta+1)} \tag{2.38}$$

These common surface-averaged interfacial displacements are then employed in the interfacial traction equilibrium conditions

$$\hat{t}_z^{+1(\alpha,\beta)} + \hat{t}_z^{-1(\alpha,\beta)} = 0 \tag{2.39}$$

$$\hat{t}_z^{+2(\alpha,\beta)} + \hat{t}_z^{-2(\alpha,\beta)} = 0 \tag{2.40}$$

expressed in terms of the common interfacial displacements,

$$\begin{aligned} L_{12}^{(\alpha,\beta)}\widehat{w}^{1(\alpha,\beta)} + \left(L_{11}^{(\alpha,\beta)} + L_{22}^{(\alpha+1,\beta)}\right)\widehat{w}^{1(\alpha+1,\beta)} + L_{21}^{(\alpha+1,\beta)}\widehat{w}^{1(\alpha+2,\beta)} \\ + L_{14}^{(\alpha,\beta)}\widehat{w}^{2(\alpha,\beta)} + L_{13}^{(\alpha,\beta)}\widehat{w}^{2(\alpha,\beta+1)} + L_{24}^{(\alpha+1,\beta)}\widehat{w}^{2(\alpha+1,\beta)} \\ + L_{23}^{(\alpha+1,\beta)}\widehat{w}^{2(\alpha+1,\beta+1)} = \left(C_{66}^{(\alpha,\beta)} - C_{66}^{(\alpha+1,\beta)}\right)\,\theta y_o^{(\beta)} \end{aligned} \tag{2.41}$$

$$\begin{aligned} L_{32}^{(\alpha,\beta)}\widehat{w}^{1(\alpha,\beta)} + L_{31}^{(\alpha,\beta)}\widehat{w}^{1(\alpha+1,\beta)} + L_{42}^{(\alpha,\beta+1)}\widehat{w}^{1(\alpha,\beta+1)} \\ + L_{41}^{(\alpha,\beta+1)}\widehat{w}^{1(\alpha+1,\beta+1)} + L_{34}^{(\alpha,\beta)}\widehat{w}^{2(\alpha,\beta)} \\ + \left(L_{33}^{(\alpha,\beta)} + L_{44}^{(\alpha,\beta+1)}\right)\widehat{w}^{2(\alpha,\beta+1)} + L_{43}^{(\alpha,\beta+1)}\widehat{w}^{2(\alpha,\beta+2)} \\ = \left(-C_{55}^{(\alpha,\beta)} + C_{55}^{(\alpha,\beta+2)}\right)\theta x_o^{(\alpha)} \end{aligned} \tag{2.42}$$

The above equations apply within the beam's cross section. On the bar's lateral boundary, the traction-free condition, Eq. (2.9), must be satisfied along the vertical and horizontal cross-section boundaries. The components of the unit vector normal to the right and left vertical boundaries of the bar's cross section in Eq. (2.9) are [$\pm$1,0,0], and the normal derivative of ψ, $d\psi/dn$ is replaced by $d\psi/dx$. The corresponding components along the top and bottom horizontal boundaries are [0, $\pm$1,0] and the normal derivative of ψ, $d\psi/dn$, is replaced by $d\psi/dy$. Applying the traction-free boundary condition in a surface-averaged sense along the exterior surfaces of boundary subvolumes, the following conditions are obtained which are expressed in terms of the exterior and interior surface-averaged displacements associated with boundary subvolumes. Along the left and right vertical boundaries with the unit normals $[-1,0,0]$ and $[1,0,0]$, respectively, the traction-free conditions simplify to,

$$\hat{w}^{+1^{(1,\beta)}} - \hat{w}^{-1^{(1,\beta)}} = \theta y_o^{(\beta)} h_\alpha \tag{2.43}$$

$$\hat{w}^{+1^{(N_\alpha,\beta)}} - \hat{w}^{-1^{(N_\alpha,\beta)}} = \theta y_o^{(\beta)} h_\alpha \tag{2.44}$$

where β = 1, … , N_β.

Similarly, the bottom and top horizontal boundaries with the unit normals $[0,-1,0]$ and $[0,1,0]$, respectively, the traction-free conditions are,

$$\hat{w}^{+2^{(\alpha,1)}} - \hat{w}^{-2^{(\alpha,1)}} = -\theta x_o^{(\alpha)} l_\beta \tag{2.45}$$

$$\hat{w}^{+2^{(\alpha,N_\beta)}} - \hat{w}^{-2^{(\alpha,N_\beta)}} = -\theta x_o^{(\alpha)} l_\beta \tag{2.46}$$

where α = 1, … , N_α.

The global system of equations for the unknown surface-averaged interfacial and boundary displacements may be expressed in terms of the global stiffness matrix as follows,

$$\begin{bmatrix} G_{11} & G_{12} \\ G_{21} & G_{22} \end{bmatrix} \begin{bmatrix} \hat{w}^1 \\ \hat{w}^2 \end{bmatrix} = \begin{bmatrix} \Delta C_{66} \\ \Delta C_{55} \end{bmatrix} \theta \tag{2.47}$$

where the structure of the first submatrix G_{11} is shown below, with similar results for the remaining submatrices.

$$G_{11} = \begin{bmatrix} L_{12}^{(1,1)} & L_{11}^{(1,1)} + L_{22}^{(2,1)} & L_{21}^{(2,1)} & & 0 & \cdot & \cdot & \cdot \\ \cdot & \cdot & \cdot & & \cdot & \cdot & \cdot & \cdot \\ \cdot & 0 & L_{12}^{(\alpha,\beta)} & & L_{11}^{(\alpha,\beta)} + L_{22}^{(\alpha+1,\beta)} & L_{21}^{(\alpha+1,\beta)} & 0 & \cdot \\ \cdot & \cdot & \cdot & \cdot & \cdot & \cdot & \cdot & \\ \cdot & \cdot & \cdot & 0 & L_{12}^{(N_\alpha-1,N_\beta)} & L_{11}^{(N_\alpha-1,N_\beta)} + L_{22}^{(N_\alpha,N_\beta)} & L_{21}^{(N_\alpha,N_\beta)} & \end{bmatrix} \tag{2.48}$$

The above system of equations is singular, with the rank of $N_\alpha \times N_\beta - 1$, thereby requiring an additional constraint equation that eliminates rigid body motion along the prismatic bar's axis. To summarize, each subvolume has four unknown surface-averaged displacements, and due to displacement continuity, traction continuity, and boundary conditions, each subvolume is assigned with four equations. With $4N_\alpha N_\beta$ sets of four equations, it is possible to solve for the solution upon elimination of the rigid body motion along the out-of-plane axis.

2.4.3. Constraints

One additional condition is necessary to eliminate the effect of rigid body motion and hence the singularity of the global stiffness matrix. The centroid is the rotation center in each cross section without any in-plane displacement. One approach is to constrain the out-of-displacement $w(x,y)$ by requiring that $w(0,0) = 0$ at the cross-section centroid. This constraint cannot be employed, however, for hollow cross sections with the centroid located outside the cross section itself. A more general and rigorous fixation condition specifically for the torsion problem requires the integral along the contour of the cross section to be zero,

$$\oint w(x,y)ds = \sum_{s} \hat{w}^{(\alpha,\beta)} = 0 \tag{2.49}$$

The solution of the above augmented global system of equations yields the unknown interfacial surface-averaged displacements which yield the corresponding surface-averaged tractions as well as the pointwise displacements, strains and stresses in each subvolume.

2.5. Finite Difference Formulation and Solution

The same rectangular shape cross section with the dimension H along the x direction and the dimension L along the y direction employed in the FVM analysis is considered in this section using the finite-difference method (FDM). The FDM analysis is limited to homogeneous cross sections made of linearly elastic isotropic materials. In contrast with the FVM analysis, the FDM-based solution to the Saint Venant's torsion problem is obtained independently for both the warping and Prandtl's stress functions using the displacement and stress formulations, respectively.

2.5.1. Discretization

The FDM analysis is based on approximating the partial derivatives appearing in the governing differential equation at different points within the analyzed domain by finite differences involving unknown values of the function itself evaluated at the given and adjacent points. Therefore, the analyzed domain is discretized into a grid of points or nodes such that the entire domain is spanned. Typically for convergence reasons, the nodes are equally spaced in the interior of the analyzed domain. In order to compare the FVM and FDM solutions on the same footing, the FDM grid is constructed based on the subvolume discretization of the analyzed cross section into equally dimensioned subvolumes along the x and y axes. Then the nodes are inserted in the center of each (α, β) subvolume, producing uniform node spacing between interior nodes which is the same as the subvolume dimensions. Additional nodes are inserted in the middle of the exterior faces of all the boundary subvolumes in order to satisfy the governing equation along the boundary and be able to apply the boundary conditions on the rectangular cross section's lateral surfaces. Therefore the node spacing between the boundary nodes and the adjacent interior nodes is half of the distance between interior nodes. This discretization scheme produces a grid containing $(N_\alpha + 2) \times (N_\beta + 2)$ nodes. The indices of these nodes follow the subvolume convention and hence are numbered 1 to $(N_\alpha + 2)$ from the left to the right, and 1 to $(N_\beta + 2)$ from the bottom to the top. Fig. (2.3) illustrates the above-described domain discretization.

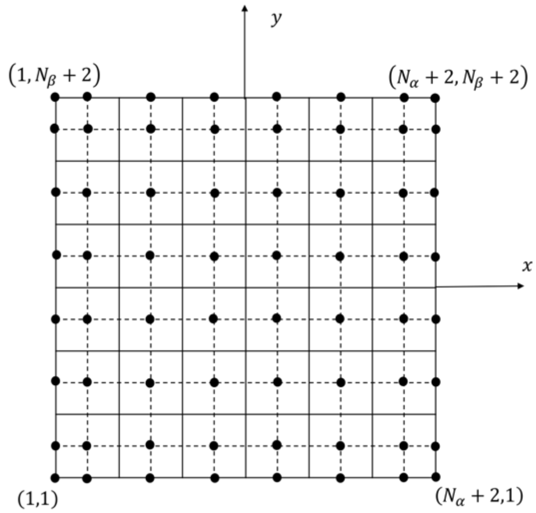

Figure 2.3. Depiction of an 8×8 node FDM grid on a square domain.

2.5.2. Displacement Formulation

The Laplace equation that the warping function $\psi(x, y)$ must satisfy, Eq. (2.7) repeated below for convenience,

$$\frac{\partial^2\psi}{\partial x^2} + \frac{\partial^2\psi}{\partial y^2} = 0 \tag{2.50}$$

is discretized by approximating the partial derivatives of the warping functions by their values at the given and adjacent nodes. Using the Taylor series expansions along the x axis at the $(\alpha - 1, \beta)$ and $(\alpha + 1, \beta)$ nodes, the second partial derivative of $\psi(x, y)$ with respect to x at the (α, β) node is obtained in terms of the nodal values of the warping function at the three horizontal node in the finite difference form,

$$\frac{\partial^2\psi}{\partial x^2} = \frac{\psi^{(\alpha+1,\beta)} - 2\psi^{(\alpha,\beta)} + \psi^{(\alpha-1,\beta)}}{d^2} \tag{2.51}$$

Similarly, the first partial derivative with respect to x employed in the calculation of the shear stress component is

$$\frac{\partial\psi}{\partial x} = \frac{\psi^{(\alpha+1,\beta)} - \psi^{(\alpha,\beta)}}{d} \tag{2.52}$$

Performing the same Taylor series expansions along the y axis, the following results are obtained for the second and first partial derivatives of $\psi(x, y)$ with respect to y

$$\frac{\partial^2 \psi}{\partial y^2} = \frac{\psi^{(\alpha,\beta+1)} - 2\psi^{(\alpha,\beta)} + \psi^{(\alpha,\beta-1)}}{d^2} \tag{2.53}$$

$$\frac{\partial \psi}{\partial y} = \frac{\psi^{(\alpha,\beta+1)} - \psi^{(\alpha,\beta)}}{d} \tag{2.54}$$

Combining Eq. (2.51) and Eq. (2.53), the finite difference approximation of the Laplace equation for the warping function involving five inner nodes becomes,

$$\psi^{(\alpha+1,\beta)} + \psi^{(\alpha-1,\beta)} + \psi^{(\alpha,\beta+1)} + \psi^{(\alpha,\beta-1)} - 4\psi^{(\alpha,\beta)} = 0 \tag{2.55}$$

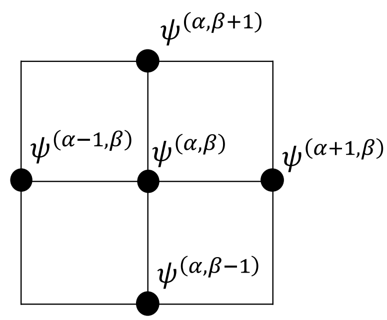

Figure 2.4. Depiction of an FDM inner node and its adjacent nodes.

Special treatment is needed for the boundary nodes owing to the lack of four adjacent nodes required for the satisfaction of both the equilibrium and traction-free conditions on the lateral surface. One way to accomplish this is to use forward or backward differencing at each boundary node to satisfy the above two conditions. Another way is to use the central difference scheme since it produces a second-order error, while forward/backward difference yields a first-order error. To accomplish this, imaginary nodes outside of the cross-section's domain are introduced because it is impossible to apply the central difference scheme for the boundary nodes directly. Using the imaginary boundary nodes, the Laplace's equation for boundary nodes may still be formulated thanks to imaginary nodes.

The imaginary nodes are identified by the superscripts 0 and $(N_\alpha + 3)$ associated with the x axis, and 0 and $(N_\beta + 3)$ associated with the y axis. Using this convention, the boundary nodes have to satisfy the following traction-free conditions along each of the four cross section sides,

Bottom boundary nodes	$\psi^{(\alpha,2)} - \psi^{(\alpha,0)} = -x^{(\alpha,1)}d$	(2.56)
Top boundary nodes	$\psi^{(\alpha,N_\beta+3)} - \psi^{(\alpha,N_\beta+1)} = -x^{(\alpha,N_\beta+2)}d$	(2.57)
Left boundary nodes	$\psi^{(2,\beta)} - \psi^{(0,\beta)} = y^{(1,\beta)}d$	(2.58)
Right boundary nodes	$\psi^{(N_\alpha+3,\beta)} - \psi^{(N_\alpha+1,\beta)} = y^{(N_\alpha+2,\beta)}d$	(2.59)

where d is the distance between the boundary nodes and the adjacent interior nodes. The edges of the cross section require the use of an imaginary node only in the direction normal to the face, while the corner nodes require the use of two imaginary nodes, in the x and y-directions. The unknown values of the warping function associated with the imaginary nodes appearing in the finite-differenced equilibrium equations for the boundary nodes, Eq. (2.53), are eliminated using the above traction-free conditions. Hence all the finite-differenced equilibrium equations at every node, including the boundary nodes, are expressed in terms of the unknown values of the warping function associated with interior and boundary nodes. These equations form a $(N_\alpha + 2) \times (N_\beta + 2)$ system of equations for as many unknown nodal values of the warping function. The rigid body motion along the z axis is eliminated by applying the contour integral in Eq. (2.51).

Once the solution of the global system of equations for the unknown nodal values of $\psi(x, y)$ is obtained, it is possible to take advantage of the stress and out-of-plane displacement relationship, Eq. (2.4) to generate the shear stress fields. Shear stress components for every interior node can be expressed in the central difference form,

$$\begin{aligned} \sigma_{xz}^{(\alpha,\beta)} &= G\theta(\frac{\psi^{(\alpha+1,\beta)} - \psi^{(\alpha-1,\gamma)}}{d} - y^{(\alpha,\beta)}) \\ \sigma_{yz}^{(\alpha,\beta)} &= G\theta(\frac{\psi^{(\alpha,\beta+1)} - \psi^{(\alpha,\beta-1)}}{d} + x^{(\alpha,\beta)}) \end{aligned} \tag{2.60}$$

Applying forward or backward difference method to the left boundary nodes gives

$$\sigma_{yz}^{(1,\beta)} = G\theta(\frac{\psi^{(2,\beta)}-\psi^{(1,\beta)}}{d} - y^{(1,\beta)}), \quad \sigma_{xz}^{(1,\beta)} = 0 \tag{2.61}$$

whereas the right boundary nodes yield,

$$\sigma_{yz}^{(N_\alpha+2,\beta)} = G\theta(\frac{\psi^{(N_\alpha+2,\beta)}-\psi^{(N_\alpha+1,\beta)}}{d} - y^{(N_\alpha,\beta)}), \quad \sigma_{xz}^{(N_\alpha+2,\beta)} = 0 \tag{2.62}$$

Similarly, applying forward or backward difference method to the bottom boundary nodes gives

$$\sigma_{xz}^{(\alpha,2)} = G\theta(\frac{\psi^{(\alpha,2)}-\psi^{(\alpha,1)}}{d} + x^{(\alpha,1)}), \quad \sigma_{yz}^{(\alpha,1)} = 0 \tag{2.63}$$

and the top boundary nodes yield,

$$\sigma_{xz}^{(\alpha,N_\beta+2)} = G\theta(\frac{\psi^{(\alpha,N_\beta+2)}-\psi^{(\alpha,N_{\beta+2})}}{d} + x^{(\alpha,N_\beta)}), \quad \sigma_{yz}^{(\alpha,N_\beta+2)} = 0 \tag{2.64}$$

2.5.3. Stress Formulation

Alternatively, it is also possible to obtain the solution to the Prandtl's stress function from the governing differential equation for $\phi(x, y)$, rewritten here for convenience,

$$\frac{\partial^2\phi}{\partial x^2} + \frac{\partial^2\phi}{\partial y^2} = -2G\theta \tag{2.65}$$

Applying the same procedure in finite-differencing the above equations as that employed in finite-differencing the Laplace's equation for the warping function, we obtain for the interior nodes the following result,

$$\phi^{(\alpha+1,\beta)} + \phi^{(\alpha-1,\beta)} + \phi^{(\alpha,\beta+1)} + \phi^{(\alpha,\beta-1)} - 4\phi^{(\alpha,\beta)} = -2G\theta d^2 \tag{2.66}$$

The advantage of the stress formulation is that the traction-free boundary condition at each node involves only the values of the Prandtl's stress function itself,

$$\phi^{(\alpha,\beta)} = 0 \tag{2.67}$$

Moreover, the finite-differenced Poisson's equation at the boundary nodes does not need to be explicitly employed and hence there is no need to introduce imaginary nodes as in the case of the corresponding Laplace equation. This is because the $N_\alpha \times N_\beta$ unknown values of the Prandtl's stress function at the interior nodes may be determined by applying the finite-differenced Poisson's equation at each node whilst eliminating the values at each boundary node associated with the set of nodes directly adjacent to the boundary using the traction-free condition. This produces the required $N_\alpha \times N_\beta$ equations for the same number of unknown nodal Prandtl's stress function values.

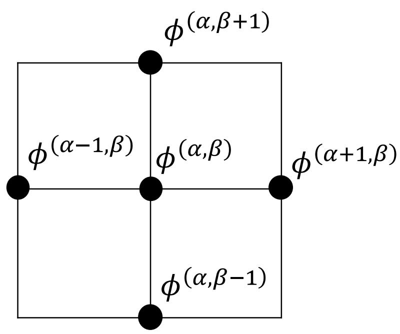

Figure 2.5. Depiction of an FDM inner node and its adjacent nodes.

Applying the above equations at each node produces the global system of equations for the unknown nodal values of the Prandtl's stress function whose solutions enables calculation of the corresponding stresses using the finite-differenced form of Eq. (2.11). Shear stress values for the inner nodes were determined using the central difference scheme as follows,

$$\sigma_{xz}^{(\alpha,\beta)} = \frac{\phi^{(\alpha,\beta+1)} - \phi^{(\alpha,\beta-1)}}{d} \tag{2.68}$$

and

$$\sigma_{yz}^{(\alpha,\beta)} = -\frac{\phi^{(\alpha+1,\beta)} - \phi^{(\alpha-1,\beta)}}{d} \tag{2.69}$$

whereas the corresponding stresses at the boundary nodes were calculated using the forward or backward finite-difference scheme. As readily seen in the above equations, at the left and right boundary nodes,

$$\sigma_{xz}^{(\alpha,\beta)} = 0 \tag{2.70}$$

and similarly at the top or bottom boundary nodes

$$\sigma_{yz}^{(\alpha,\beta)} = 0 \tag{2.71}$$

because in both cases the nodal values of the Prandtl's stress function were explicitly set to zero in order to satisfy the traction-free boundary conditions.

The stresses are related to the partial derivatives of the warping function through Eq. (2.4), which can be written in terms of the shear stress components as follows,

$$\frac{\partial \psi}{\partial x} = \frac{\sigma_{xz}}{G\theta} + y, \qquad \frac{\partial \psi}{\partial y} = \frac{\sigma_{yz}}{G\theta} - x \tag{2.72}$$

In the finite-difference sense, using the central difference scheme Eq. (2.70) becomes

$$\begin{gathered} \frac{\psi^{(\alpha+1,\beta)} - \psi^{(\alpha-1,\beta)}}{d} = \frac{\sigma_{xz}^{(\alpha,\beta)}}{G\theta} + y^{(\alpha,\beta)} \\ \frac{\psi^{(\alpha,\beta+1)} - \psi^{(\alpha,\beta-1)}}{d} = \frac{\sigma_{yz}^{(\alpha,\beta)}}{G\theta} - x^{(\alpha,\beta)} \end{gathered} \tag{2.73}$$

Eq. (2.71) can be used for at the inner nodes to determine the interior nodal out-of-plane displacements. Otherwise, applying the forward or backward difference scheme to the left and right boundary nodes, respectively gives,

$$\begin{gathered} \frac{\psi^{(2,\beta)} - \psi^{(1,\beta)}}{d} - y^{(1,\beta)} = 0 \\ \frac{\psi^{(N_\alpha+2,\beta)} - \psi^{(N_\alpha+1,\beta)}}{d} - y^{(N_\alpha+2,\beta)} = 0 \end{gathered} \tag{2.74}$$

Similarly, applying the forward or backward difference scheme to the bottom and top boundary nodes, respectively, gives

$$\frac{\psi^{(\alpha,2)} - \psi^{(\alpha,1)}}{d} + x^{(\alpha,1)} = 0$$
$$\frac{\psi^{(\alpha,N_\beta+2)} - \psi^{(\alpha,N_\beta+1)}}{d} + x^{(\alpha,N_\beta+2)} = 0 \qquad (2.75)$$

The constraint is zero total out-of-plane displacement along the contour of the cross section. Each contour segment is assumed to have the average out-of-plane displacement as the nearby point-wise out-of-plane displacement.

Eqs. (2.71)-(2.73) make up a system of linear equations. Solving this system of equations generates the values for the out-of-plane displacement at each node.

2.6. Summary and Discussion

The two methods developed in this chapter in order to solve the Saint Venant's torsion problem of rectangular cross section members, namely the finite-volume and finite-difference methods, have been implemented in MATLAB computer codes. The formulations developed using rectangular subvolume/grid domain discretizations are sufficiently general to be employed for cross sections such as T-shaped, channel-shaped and box-shaped prismatic bars. The results that these methods are able to generate include the displacement field, shear stress fields, and torsional rigidity.

Both methods will be validated in Chapter 3 against the elasticity solution for rectangular cross section bars of any aspect ratio. The finite-difference method is well-suited for the solution of Saint Venant's torsion problems involving homogenous linear elastic isotropic material cross sections, while the finite-volume method is also capable of solving torsion problems involving heterogeneous, linear elastic orthotropic material cross sections. In the finite-volume approach, subvolumes that make up any shape cross section are rectangular with their own material property. Each subvolume is in stress equilibrium and satisfies traction and displacement continuity with its adjacent neighbors in a surface-averaged sense. This property is one of the remarkable advantages of the finite-volume method where extremely fine meshing is not required for the interfaces separating composite materials as required by the finite-difference and finite-element methods.

Extended programs have also been developed for more general shapes of open/closed cross sections through appropriate coding. These will be employed in Chapters 4 and 5 in the context of membrane analogy assessment and analysis of prismatic with composite cross sections.

Chapter 3

3. Finite Volume Technique Validation

3.1. Introduction

Prior to applying the finite volume technique derived in Chapter 2 to Saint Venant's torsion problems involving cross sections of arbitrary shape and composite construction, we must validate the new method through comparison with cross sections whose elasticity solutions are already available. One benchmark for the validation process is the solid rectangular cross section composed of a homogenous isotropic material for which exact analytical solution in the form of an infinite Fourier series is available. Rectangular cross sections with different aspect ratios are employed in the validation. Out-of-plane displacements and shear stress resultants at specific locations within the cross-sectional area are calculated using the elasticity solution and compared with the finite-volume and finite-difference results as a function of the domain discretization refinement.

At each mesh discretization employed in the finite-volume analysis, a finite-difference grid is set up with one node centered in each subvolume. This enables comparison of the finite-volume and finite-difference results at the same points in the cross section. In both methods, the displacement formulation had been employed to generate the out-of-plane displacement field from which the shear stress fields are obtained using Hooke's law. Least square difference values at all grid points are also calculated to quantify the overall difference between the two numerical methods and the elasticity solution. The convergence of torsional rigidity calculated from the stress field is also examined to provide additional validation support. The rate of convergence with mesh refinement also sheds light on the effectiveness of the two numerical methods. The other benchmark is a composite bar consisting of two different rectangular regions for which exact elasticity solution in Fourier series form is also available. Comparison of the finite volume solution with the exact analytical solution as well as with the finite difference solution yields critical analysis of the accuracy of the finite-volume theory.

3.2. Rectangular Homogenous Cross Section

We validate the developed finite-volume solution first by comparison with the exact analytical solution for the $2a \times 2b$ rectangular solid cross section, and compare its convergence performance relative to the finite-difference solution to the same problem. Mesh discretization with the same equally-dimensioned subvolumes/grid spacing had been employed for consistency.

3.2.1. Elasticity Solution

The analytical solution for the Prandtl's stress function $\phi(x,y)$ is obtained in closed form in terms of an infinite Fourier series taken over the odd harmonics of $\sin(n\pi/2a)$,

$$\phi(x,y) = \frac{32G\theta a^2}{\pi^3} \sum_{n=1,3,5,\ldots}^{\infty} \frac{1}{n^3}(-1)^{\frac{n-1}{2}} \left(1 - \frac{\cosh\frac{n\pi y}{2a}}{\cosh\frac{n\pi b}{2a}}\right) \sin\frac{n\pi x}{2a} \tag{3.1}$$

from which we obtain the shear stresses σ_{xz} and σ_{yz}

$$\sigma_{xz}(x,y) = \frac{\partial\phi}{\partial y} = -\frac{16G\theta \mathrm{a}}{\pi^2} \sum_{n=1,3,5,\ldots}^{\infty} \frac{1}{n^2}(-1)^{\frac{n-1}{2}} \left(\frac{\sinh\frac{n\pi y}{2a}}{\cosh\frac{n\pi b}{2a}}\right) \cos\frac{n\pi x}{2a} \tag{3.2}$$

$$\begin{aligned}\sigma_{yz}(x,y) &= -\frac{\partial\phi}{\partial x} \\ &= \frac{16G\theta a}{\pi^2} \sum_{n=1,3,5,\ldots}^{\infty} \frac{1}{n^2}(-1)^{\frac{n-1}{2}} \left(1 - \frac{\cosh\frac{n\pi y}{2a}}{\cosh\frac{n\pi b}{2a}}\right) \sin\frac{n\pi x}{2a}\end{aligned} \tag{3.3}$$

and thus calculate the shear stress resultant field according to $\tau(x,y) = \sqrt{\sigma_{xz}^2 + \sigma_{yz}^2}$. The out-of-plane displacement w is obtained by integrating Eq. (3.2) and Eq. (3.3), multiplied by the angle of twist per unit length. This yields,

$$w = \theta xy - \frac{32\theta a^2}{\pi^3} \sum_{n=1,3,5,\ldots}^{\infty} \frac{1}{n^3}(-1)^{\frac{n-1}{2}} \left(\frac{\sinh\frac{n\pi y}{2a}}{\cosh\frac{n\pi b}{2a}}\right) \sin\frac{n\pi x}{2a} \tag{3.4}$$

Finally, the angle of twist-torque relationship is obtained by integrating $\phi(x,y)$ over the cross section, yielding

$$T = 2\int_A \phi(x,y)\,dxdy$$
$$= \frac{1}{3}G\theta(2a)^3(2b)\left(1 - \frac{192}{\pi^5}\frac{a}{b}\sum_{n=1,3,5,\dots}^{\infty}\frac{1}{n^5}\tanh\frac{n\pi b}{2a}\right) \quad (3.5)$$

The above analytical solution converges fast with the number of harmonics for a wide range of aspect ratios a/b. Twenty-five harmonics are sufficient to obtain converged solutions in the aspect ratio range [1, 20] which have been employed in assessing the predictive capability of the finite-volume solution of the Saint Venant's torsion problem.

Fig. (3.1) presents the analytical full-field distributions of the out-of-plane displacement $w(x,y)$ and shear stress resultant $\tau = \sqrt{\sigma_{xz}^2 + \sigma_{yz}^2}$ employed in the assessment of the finite-volume method for a square and rectangular cross section with aspect ratios of 1, 5, 10. The distributions have been normalized by the corresponding maximum values so that the results are valid for any applied angle of twist per unit length for angles small enough to be consistent with the infinitesimal deformation assumption. For the square cross section, the maximum and minimum out-of-plane displacements occur along the edges at some distance away from the corners. The shear stress resultants also occur along the edges halfway between the plate's corners. As required, the shear stress resultant vanishes at the four corners in order to satisfy the traction-free boundary condition. The twenty-five harmonics used in the infinite Fourier series representation of the Prandtl's stress function are sufficient to very accurately capture this condition.

As the plate's aspect ratio increases, the maximum and minimum out-of-plane displacements along the edges shift towards the plate's corners, whereas the shear stress resultant becomes more uniform along the edges. Concomitantly, the Prandtl's stress function calculated using Eq. (3.1) becomes increasingly independent of the long direction, and may at sufficiently large aspect ratios be approximated by a parabolic function, and illustrated in Fig. (3.2) for the aspect ratios *a/b* = 1,5, 10 and 20. This is the basis for the membrane analogy-based approximation for thin-walled cross sections discussed in Chapter 4.

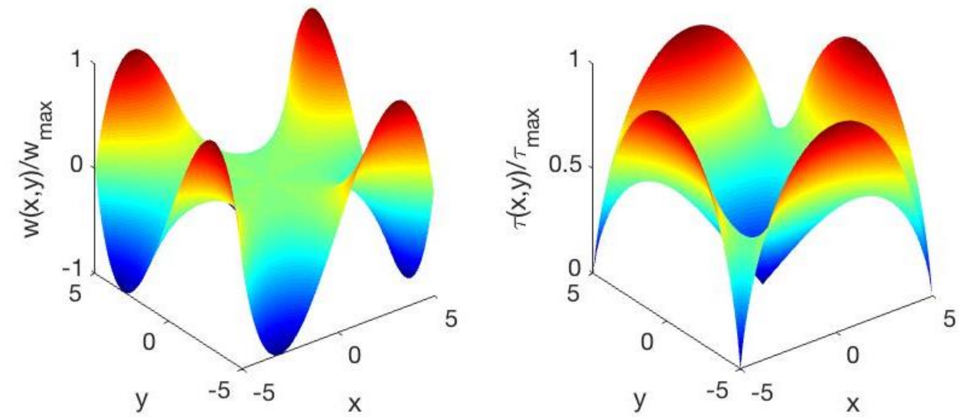

Square cross section

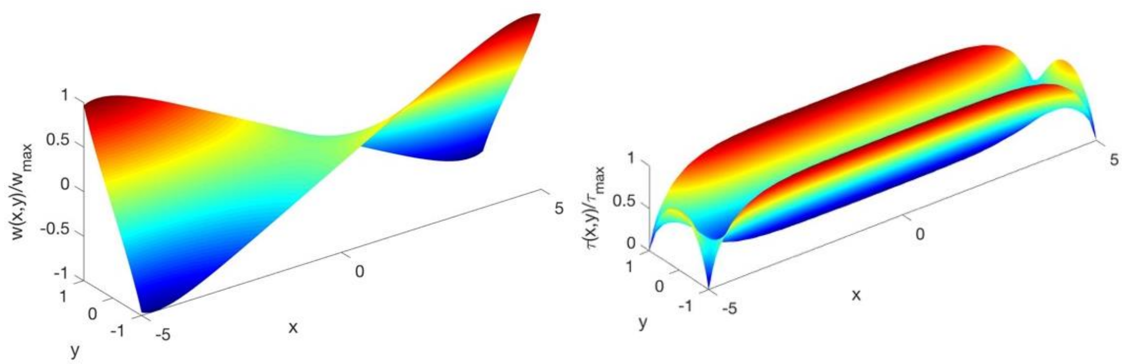

Rectangular cross section with the aspect ratio *a/b* = 5

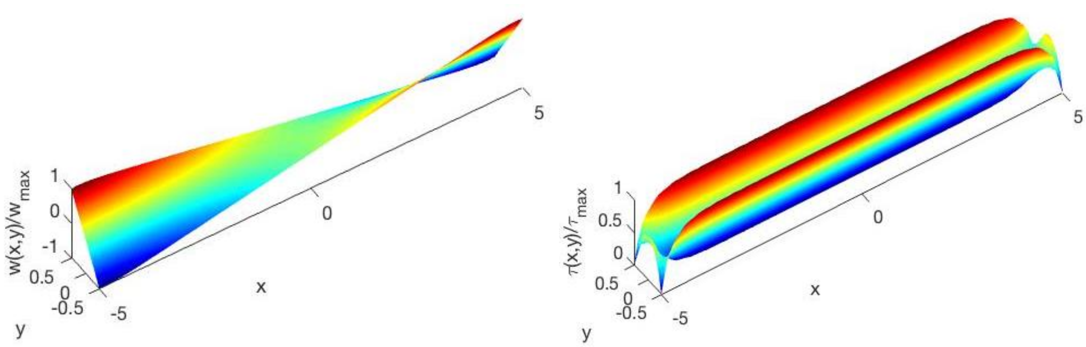

Rectangular cross section with the aspect ratio *a/b* = 10

Figure 3.1. Normalized out-of-plane displacement (left column) and shear stress resultant distributions for rectangular cross sections with different aspect ratios.

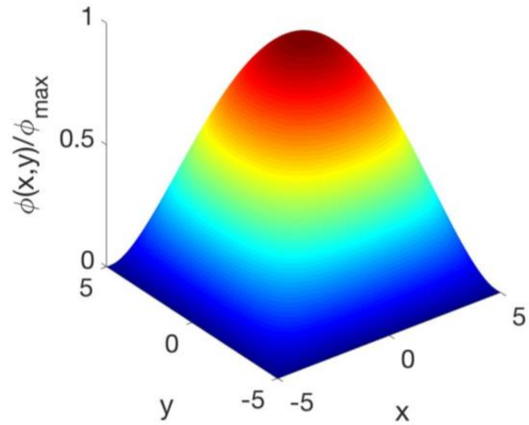

a/b = 1

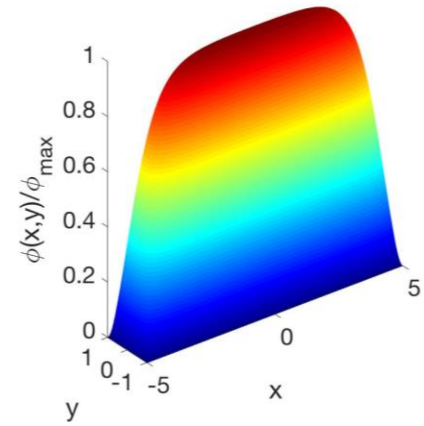

a/b = 5

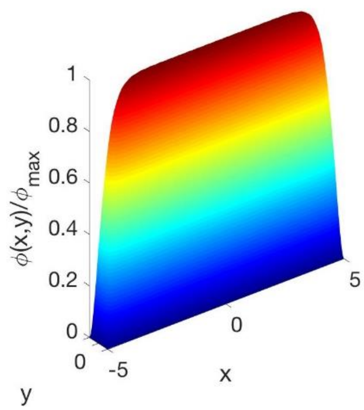

a/b = 10

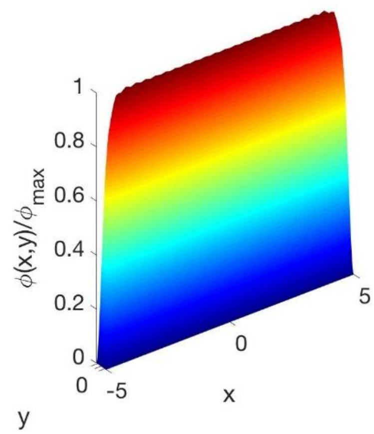

a/b = 20

Figure 3.2. Normalized Prandtl's stress function distributions for rectangular cross sections with different aspect ratios.

3.2.2. Comparison

We first compare the convergence of the finite-volume solution with mesh refinement to the elasticity solution for the rectangular cross-section torsion problem. Towards this end, the cross-section domain is initially divided into $N_\alpha \times N_\beta$ equally-dimensioned $(h_\alpha = l_\beta)$ subvolumes, then successively split into more equally-dimensioned subvolumes in order to obtain finer meshes. Holding the cross section's horizontal dimension fixed, rectangular cross sections with aspect ratios of 1, 5, 10 and 20 were generated and initially subdivided into 10×10, 20×4, 30×3 and 40×2, respectively, uniformly sized subvolumes at the coarsest level of discretization. Note that the aspect ratio of each rectangular cross section is obtained from the ratio of the number of subvolumes along the horizontal and vertical dimensions, N_α / N_β, since the subvolume dimensions are equal. Dividing the original equally-dimensioned subvolumes by an odd arithmetic sequence ensures that the centers of the original subvolumes remain centers of the smaller subvolumes in each finer discretization. This ensures that the stress field is compared at the same points with mesh refinement. Comparison of the convergence with mesh/grid refinement of the full-field finite-volume and finite-difference $w(x,y)$, $\tau(x,y)$ distributions to the elasticity solution was made in the least-squared sense, where the differences were calculated in the center of each subvolume and summed according to,

$$\Delta w = \frac{1}{n^2} \sqrt{\sum_{i=1}^{N_\alpha} \sum_{j=1}^{N_\beta} [w^{approx}(x_i, y_i) - w^{elast}(x_i, y_i)]^2} \tag{3.6}$$

and subsequently normalized by the maximum out-of-plane displacement or shear stress resultant value obtained from the elasticity solution at the same locations. The same process is applied for the finite-difference solutions at exactly the same locations in the initial grid. This is the reason why the finite-difference nodes in the partial differential equation discretization were placed in the center of each subvolume.

The results of the least square differences of the out-of-plane displacements at the initial nodes are presented in Fig. (3.3). As observed, the finite-volume technique does not converge as fast as the finite-difference method for all the aspect ratios. It should be noted that the convergence of the finite-difference method on homogeneous domains with isotropic properties has been extensively studied and is well-established. It is relatively fast because the governing partial differential equation is solved directly and a discretized form in a pointwise manner at increasing closer points rather through a particular approximation of the displacement field in discretized subvolumes. In contrast, the finite-volume method has been developed explicitly for heterogeneous materials characterized by multiple homogeneities embedded in a matrix material. Hence its strength lies in producing stable solutions to problems involving materials with microstructures that require satisfaction of both displacement and traction continuity across common interfaces, an application for which the finite-difference method is not naturally suited. Nonetheless, comparison with the finite-difference results provides a demanding test of the finite-volume method's convergence behavior.

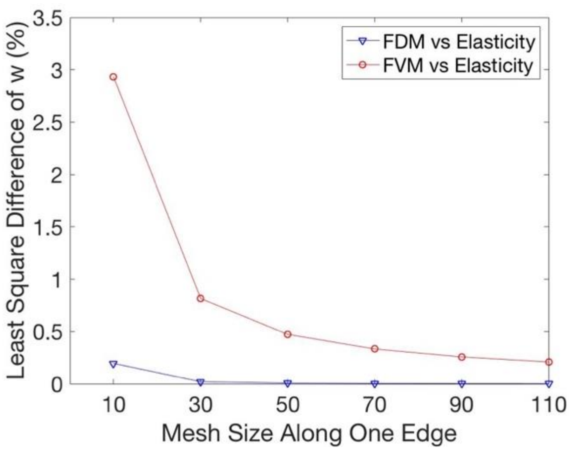

a/b = 1

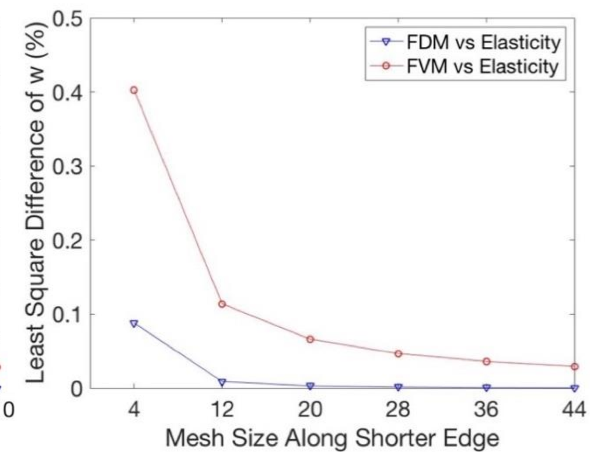

a/b = 5

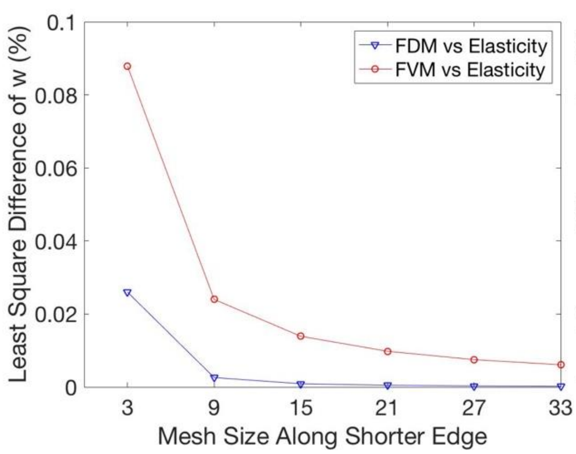

a/b = 10

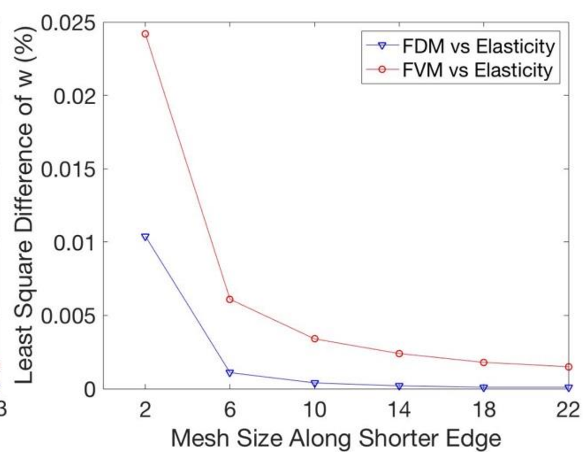

a/b = 20

Figure 3.3. Convergence of the finite-difference and finite-volume out-of-plane displacement field calculated at selected subvolume centers with mesh refinement to the elasticity solution for the torsion problem of rectangular cross sections with different aspect ratios.

Specifically, for the square place, the normalized least square error in the out-of-plane displacement field based on 100 initial nodal values is less than 1% for the relatively coarse plate discretization into 30×30 subvolumes. This error decreases to below 0.5% for the

100×100 subvolume domain discretization. Progressively smaller errors are observed in the case of the remaining aspect ratios. For instance, in the case of the aspect ratio of five, the coarse mesh of 40×12 subvolumes yield an error just above 0.1% which is reduced to less than 0.05% for the finest mesh of 220×44 subvolumes. The reason for the decreasing errors with increasing plate aspect ratio is because the mesh density also increases since the plate area decreases because of the manner in which the different aspect ratios were generated. Nonetheless, the continuous refinement of the subvolume discretization produces monotonically decreasing errors predicted by the finite-volume method which is desirable behavior. These errors are very small at sufficiently small subvolume refinement. When the mesh density remains constant, the error for the different cross section aspect ratios remains in the same order of magnitude range with increasing mesh refinement.

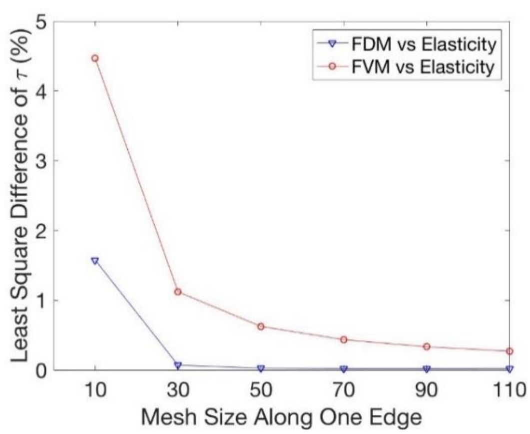

a/b = 1

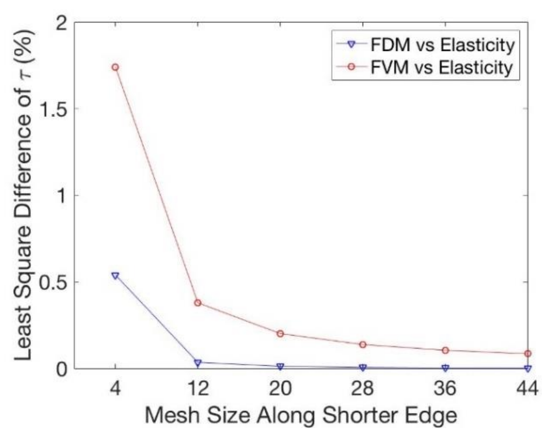

a/b = 5

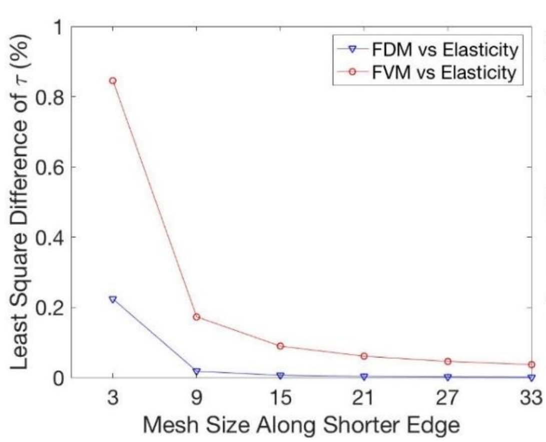

a/b = 10

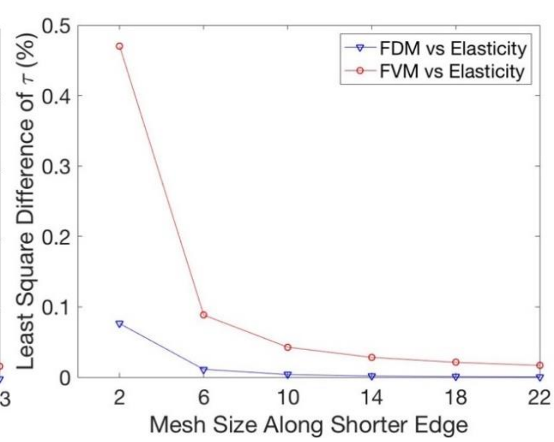

a/b = 20

Figure 3.4. The convergence of the finite-difference and finite-volume shear stress resultant field calculated at selected subvolume centers with mesh refinement to the elasticity solution for the torsion problem of rectangular cross sections with different aspect ratios.

The corresponding results for the convergence of the shear stress resultant with mesh refinement are shown in Fig. (3.4). The convergence behavior is similar to that observed for the out-of-plane displacement except that the error does not decrease as rapidly with increasing aspect ratio. Nonetheless, errors less than 1% are achievable with relatively coarse mesh discretizations for the square cross section which halfway further with increasing aspect ratio.

The results presented in Figs. (3.3)-(3.4) provide a global picture of the finite-volume method's convergence behavior with mesh refinement. To get an idea of how well the method converges to the elasticity solution throughout the entire cross section's domain in a pointwise manner, the error distributions have been calculated for mesh sizes for which the global differences between the elasticity and finite-volume solutions are acceptably small. Using Figs. (3.3)-(3.4) as a basis for this mesh selection, the mesh sizes for the cross sections with the aspect ratios $a/b = 1{,}5, 10, 20$ were 110×110, 220×40, 330×30, 440×20, respectively. The spatial error distributions of the out-of-plane displacement and shear stress resultant for the first three aspect ratios are presented in Fig. (3.5). These distributions have been calculated in the center of each subvolume for the respective meshes and compared with the corresponding values at the same points obtained from the elasticity solution. As observed, the maximum pointwise differences occur in the regions of high gradients of the respective displacement and stress fields. For the out-of-plane displacement, this occurs along the cross-section's edges in the vicinity of the corners. For the shear stress resultant, the maximum differences occur directly at the four corners where the shear stress resultant has to vanish. The finite-volume method approximates the stress field linearly using local coordinates. Hence in order to capture the large stress gradients at the corners, large mesh density is required in these regions. Elsewhere throughout the cross-section's domain where the displacement and stress fields vary less rapidly, the error distributions are very small as suggested by the global calculations. This includes large aspect ratio cross sections for which the Prandtl's stress function varies approximately parabolically as seen in Fig. (3.2), with concomitant shear stress resultant variation in Fig. (3.1). Full-field differences between the elasticity and finite-difference solutions, which are much smaller than those presented in Fig. (3.5) are illustrated for completeness in Appendix B.

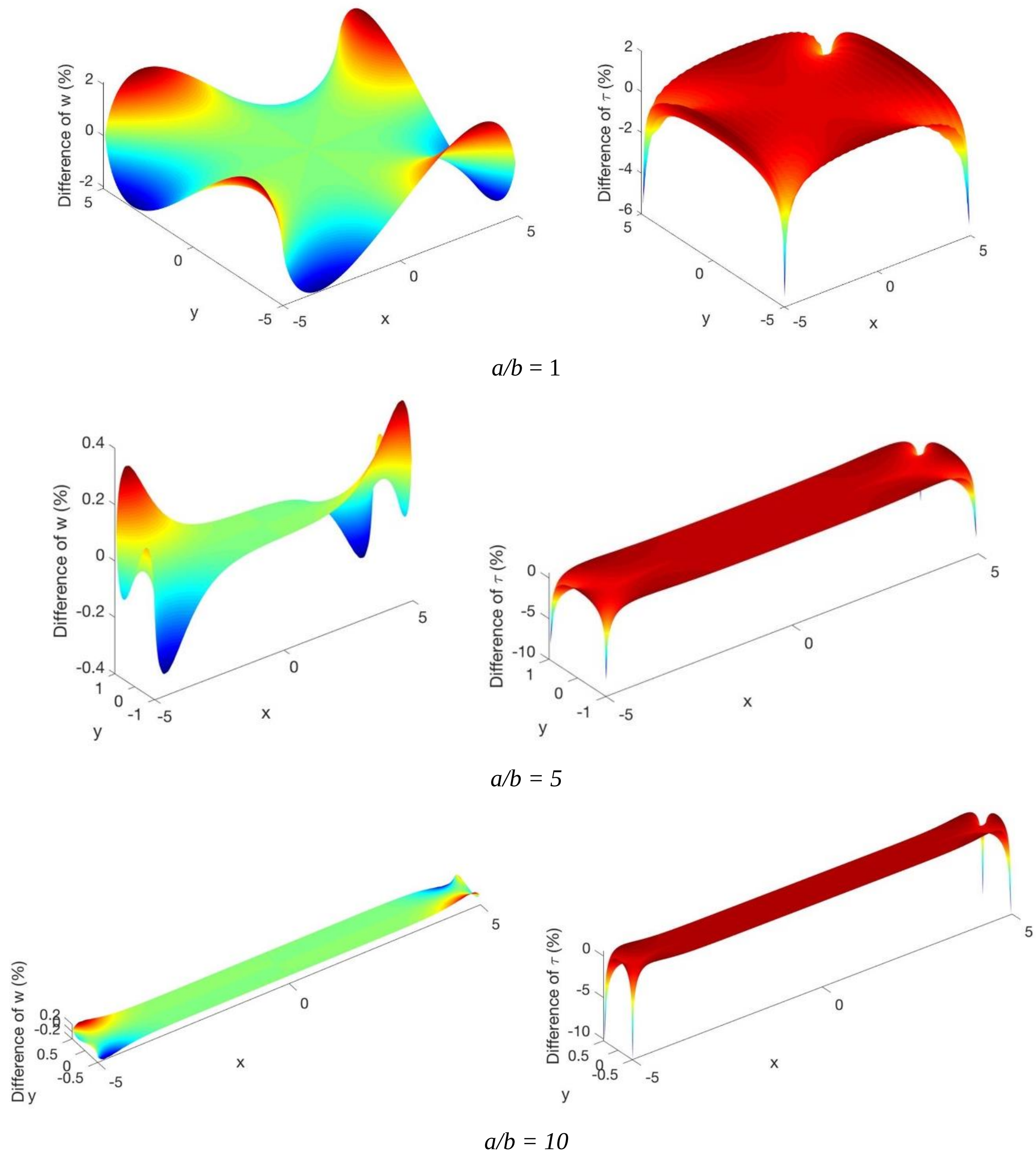

Figure 3.5. Full-field difference of displacement and shear stress (FVM vs Elasticity).

Finally, we present a comparison of the convergence behavior of the finite-volume and finite-difference methods with mesh refinement to the elasticity results for the torsional rigidity of rectangular bars with different aspect ratios. The torsional rigidity may be calculated using either Eq. (2.10) using the shear stress field or Eq. (2.14) using the Prandtl's stress function. For the elasticity solution, the torsional rigidity has been calculated using the known Prandtl's stress function for which Eq. (2.14) is obtained in closed form as given by Eq. (3.5). Since the finite-volume and finite-difference solutions are displacement-based, the torsional rigidity for these methods has been calculated using Eq. (2.10). The calculations were performed by evaluating the moments produced by each shear stress component at same locations within each subvolume.

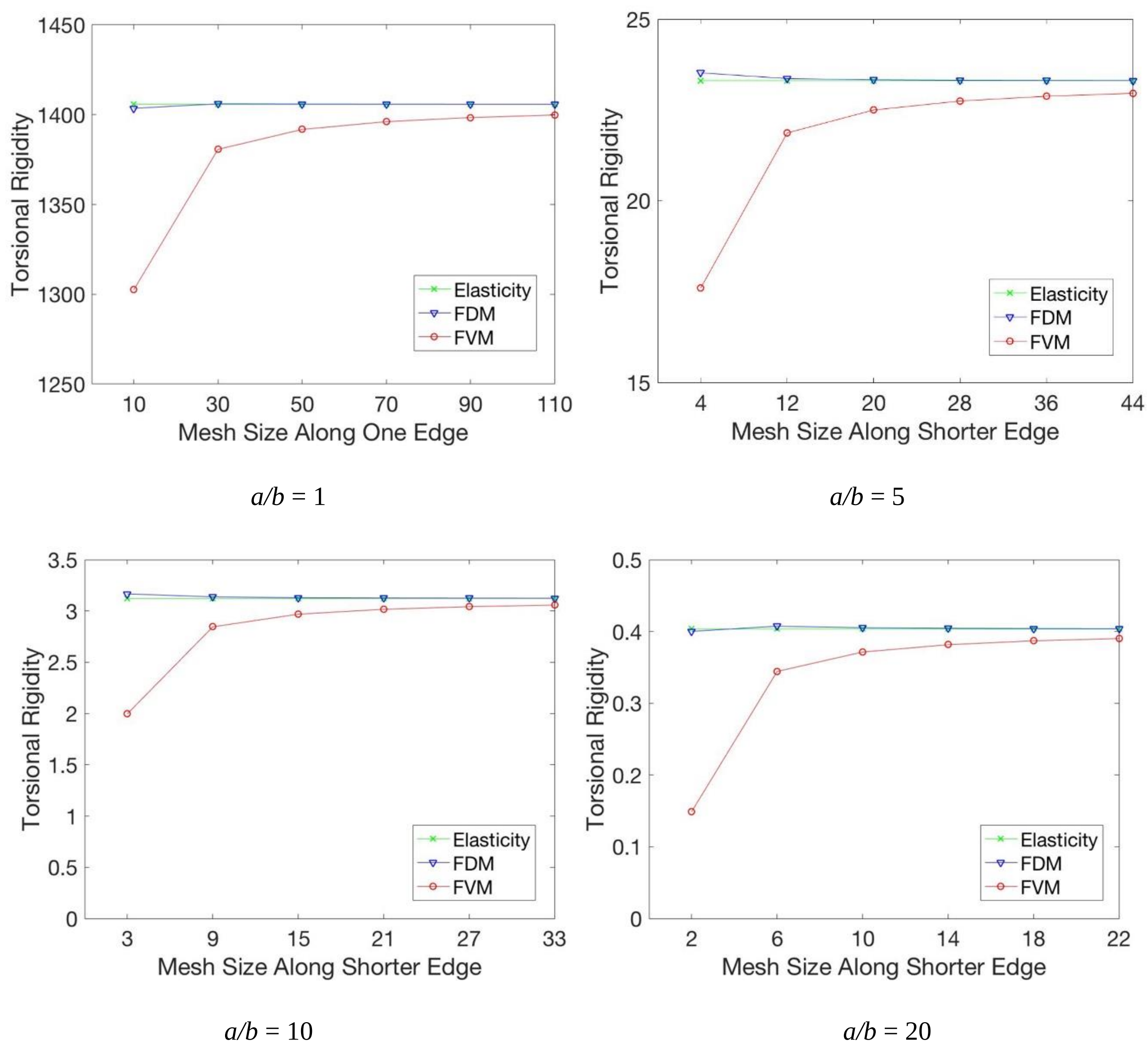

Figure 3.6. Convergence of the torsional rigidity with mesh refinement for rectangular cross sections with different aspect ratios.

Fig. (3.6) illustrates the convergence behavior of torsional rigidity with mesh refinement for the four cross section aspect ratios. As observed, the finite-volume theory performs very well when the cross-section domain is discretized sufficiently well.

3.2.3. Force Equilibrium Verification

As an additional check, we examine the requirement that the shear stress distributions $\sigma_{xz}(x,y)$ and $\sigma_{yz}(x,y)$ are self-equilibrating and thus produce zero force resultants in the x and y directions,

$$F_x = \int \sigma_{xz}(x,y)dxdy = 0,$$
$$F_y = \int \sigma_{yz}(x,y)dxdy = 0 \tag{3.7}$$

Tables (3.1)-(3.4) present the two forces calculated using the finite-volume method for the four aspect ratios of the rectangular cross sections as a function of the mesh refinement. As observed, the two forces F_x and F_y at different subvolume discretization calculated from the shear stress fields are essentially zero, illustrating excellent satisfaction of the above equilibrium conditions which does not depend on the mesh refinement. This is a remarkable strength of the finite-volume theory which makes it especially suitable for torsion problems involving composite cross sections with heterogeneous microstructures.

Table 3.1. Resultant forces F_x and F_y for the rectangular cross section with the aspect ratio of 1.

Mesh	10x10	30x30	50x50	70x70	90x90	110x110
F_x	1.1413×10^{-13}	1.0748×10^{-11}	8.0611×10^{-12}	5.2626×10^{-11}	1.2675×10^{-10}	4.2352×10^{-10}
F_y	-5.1625×10^{-14}	1.0745×10^{-11}	8.6374×10^{-11}	1.1413×10^{-10}	-6.5468×10^{-10}	8.0932×10^{-10}

Table 3.2. Resultant forces F_x and F_y for the rectangular cross section with the aspect ratio of 5.

Mesh	4x20	12x60	20x100	28x140	36x180	44x220
F_x	-7.0655×10^{-13}	-4.7046×10^{-12}	8.3648×10^{-11}	-4.2473×10^{-9}	-2.3096×10^{-9}	4.5626×10^{-9}
F_y	-1.2793×10^{-13}	1.5232×10^{-11}	-2.5175×10^{-11}	2.2869×10^{-10}	-2.3839×10^{-10}	9.6941×10^{-10}

Table 3.3. Resultant forces F_x and F_y for the rectangular cross section with the aspect ratio of 10.

Mesh	3x30	9x90	15x150	21x210	27x270	33x330
F_x	7.6933×10^{-13}	1.8015×10^{-10}	1.7214×10^{-10}	-1.9204×10^{-9}	1.2976×10^{-8}	1.4292×10^{-8}
F_y	-1.8402×10^{-14}	3.7996×10^{-12}	-1.4711×10^{-11}	-7.0878×10^{-11}	1.1855×10^{-10}	-1.6834×10^{-9}

Table 3.4. Resultant forces F_x and F_y for the rectangular cross section with the aspect ratio of 20.

Mesh	2x40	6x120	10x200	14x280	18x360	22x440
F_x	7.0610×10^{-14}	-3.1175×10^{-10}	2.2632×10^{-9}	9.3190×10^{-9}	-3.6739×10^{-10}	6.0207×10^{-8}
F_y	-3.1808×10^{-14}	6.5122×10^{-12}	-3.1045×10^{-11}	-9.1891×10^{-11}	-4.1239×10^{-10}	9.0672×10^{-10}

3.3. Rectangular Composite Cross Section

As previously mentioned, the strength of the finite-volume method lies in its ability to analyze composite and heterogeneous cross sections. Therefore, in this section, the predictive capability of the developed finite-volume method is first verified by comparison with the exact elasticity solution to the torsion problem of a cross section composed of two rectangular isotropic materials. This verification focuses on the convergence behavior of the torsional rigidity with mesh refinement to the elasticity solution as in the preceding section, and also includes the effect of the subvolume aspect ratio which was not considered previously. Upon establishing the necessary mesh discretization for sufficiently accurate results, the predictions of the finite-volume method are compared with the reported finite-element results for composite cross sections with different elastic shear modulus contrast and geometry.

3.3.1. Elasticity Solution

The torsion of a composite rectangular cross section, consisting of two rectangular regions with different material properties was solved analytically by Muskhelishvili (1963), Fig. (3.7). The following formula for the torsional rigidity GI was reported for cross sections whose overall aspect ratio a/b is equal or less than 5,

$$D = T/\theta = \frac{8}{3}(G_1 + G_2)ab^3 - 3.361b^4\frac{G_1^2 + G_2^2}{G_1 + G_2} \quad (3.8)$$

where G_1 and G_2 are the shear moduli of the different rectangular regions. This formula was obtained from the Fourier series solution by approximating the sums accordingly for the above aspect ratio range.

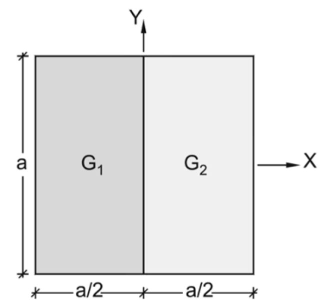

Figure 3.7. Composite cross section comprised of two homogeneous isotropic materials with different shear moduli.

3.3.2. Convergence Study

As in the preceding section, the torsional rigidity was calculated using the shear stress field obtained from the finite-volume solution in Eq. (2.10), given that the Prandtl's stress function is not available. The moments about the z axis produced by the two shear stresses in each subvolume were determined and summed up. Two approaches of taking into account the shear stress contributions to the moment were employed. In the first approach, shear stresses located at the center of each subvolume, which are the average shear stresses within the subvolume, are employed in calculating their moments about the z axis and summed up. Alternatively, in the second approach, each subvolume is further subdivided into a 5×5 grid and the shear stresses at the grid intersections are employed in calculating their moments about the z axis. The alternative approach is more computationally demanding and hence the extent of increase in the accuracy of moment calculations is of interest.

For the convergence study, a rectangular composite cross section with the overall aspect ratio a/b = 5 (with a = 5, b = 1) and isotropic shear moduli $G_1 = 5862.07$ MPa and $G_2 = 279.33$ MPa was analyzed. Using these numbers in Eq. (3.8), the torsional rigidity from the elasticity solution is calculated as 63036.3 MPa·m^4. Fig. (3.8) illustrates convergence behavior with mesh refinement of the finite-volume results for the torsional rigidity normalized by the elasticity solution. Five different subvolume aspect ratios were employed in the calculations, ranging from 0.2 to 5 producing rectangular discretizations. The results indicate that the differences in the manner of moment calculation within each subvolume based on the average shear stress value or multiple values at nine locations vanish with increasing mesh refinement. It is only for coarse mesh discretizations that relatively small differences in the calculated torque are observed. Moreover, the convergence to the elasticity solution depends on the subvolume aspect ratio. The quickest convergence occurs when the subvolumes are square. When the subvolumes are elongated (either horizontally or vertically) with aspect ratios of 5 or 0.2, the convergence is slow and there is an error of approximately 5% between the finite-volume and elasticity result at the most refined domain discretization into 9,000 subvolumes. This error reduces to less than 1% and 2% when the subvolume aspect ratio is 2 and 0.5, respectively. The square subvolumes generate the torsional rigidity of 62,495.0 MPa·m^4 at 9,000 subvolumes which produces an error of 0.86% relative to the elasticity result. It should be noted, however, that for the square subvolume the torsional rigidity reaches most of its asymptotic value at 4,000 subvolumes, with little additional increase occurring between 4,000 and 9,000 subvolumes.

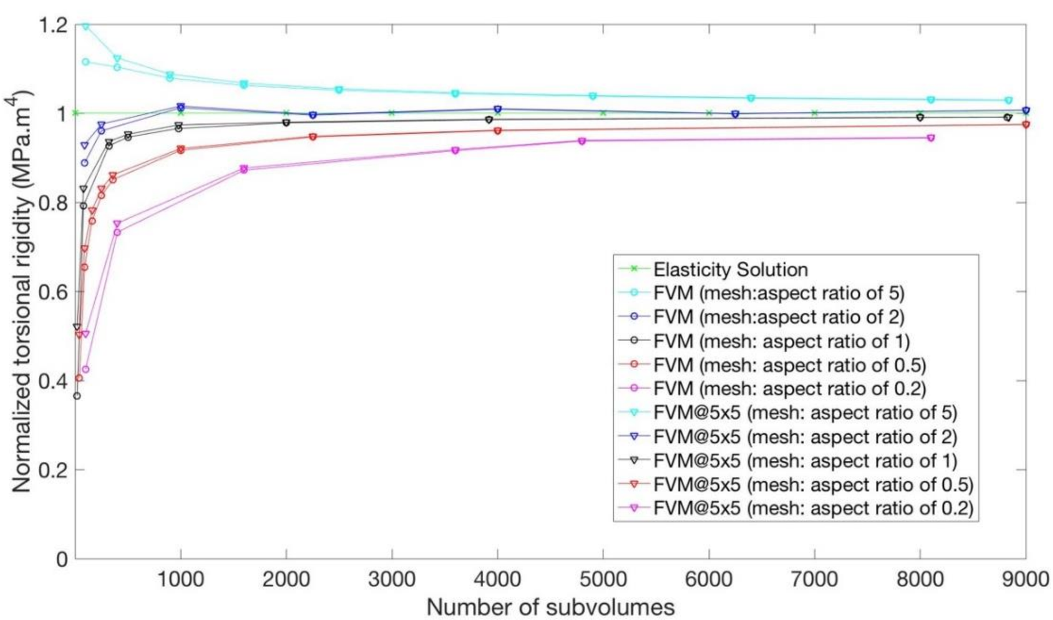

Figure 3.8. Torsional rigidity of two symmetrically placed composite cross section normalized by the elasticity solution.

For comparison, using the same shear moduli and cross section geometry Li et al. (2000) report the torsional rigidity of 60955.6 MPa·m^4 with an error of 3.3% relative to the elasticity solution. Similarly, Saygun et al. (2007) employed 200×20 linear rectangular finite elements and calculated this value as 62894.1 MPa·m^4 with a smaller error of 0.23%.

3.3.3. Comparison with Numerical Results from the Literature

A more extensive comparison with numerical results based on the finite-element method reported in the literature is provided in Table (3.5) and Table (3.6). These were generated by Darılmaz et al. (2018), Rongqiao et al. (2010), Sapountzakis (2001), Jog and Mokashi (2014), among others, for a wide range of shear modulus contrast of the composite cross section's components shown in Fig. (3.7). Torsional rigidity factors are listed in Table (3.5) and maximum shear stress factors are listed in Table (3.6). As observed, the finite-volume method's results compare very favorably with the finite-element results reported by different researchers in wide parameter space. Differences in most cases are less than 1%.

Table 3.5. Torsional rigidity factor for a composite square section ($\beta = D/(ab^3G_1)$)

G_1/G_2	β Present	β [1]	β [2]	β [3]	β [4]
1	0.1388	0.1405	0.1406	0.1405	0.1407
2	0.1949	0.1968	0.1970	0.1969	0.1972
5	0.3101	0.3104	0.3105	0.3105	–
10	0.4698	0.4658	0.4661	0.4661	–

Table 3.6. Maximum shear stress factor for a composite square section $\bar{\tau}_{max} = \tau_{max}/(aG_1\theta)$

G_1/G_2	$\bar{\tau}_{max}$ Present	$\bar{\tau}_{max}$ [1]	$\bar{\tau}_{max}$ [2]	$\bar{\tau}_{max}$ [3]
1	0.6583	0.6608	0.6755	0.6751
2	1.1780	1.1945	1.2108	1.2101
5	2.6082	2.6206	2.6764	2.6752
10	4.9053	4.9570	5.0321	5.0321

[1] Darılmaz et al. (2018); [2] Rongqiao et al. (2010); [3] Sapountzakis (2001); [4] Jog & Mokashi (2014).

3.4. Summary and Discussion

For rectangular cross sections made of homogenous and isotropic materials for which exact elasticity solutions are available in an infinite Fourier series form, the convergence of the finite-volume predictions with mesh refinement to the elasticity results for a wide range of cross section aspect ratios is slower relative to the finite-difference convergence. Yet the fact remains that the differences between the finite-volume and exact elasticity results are still within an acceptable range even with relatively coarse meshes. A differentiating feature of the finite-volume method is the satisfaction of equilibrium equations at any level of mesh discretization in a surface-averaged sense. One consequence of this is the generation of self-equilibrating shear stress fields for the investigated torsion problems at all levels of domain discretization, illustrated by the vanishing of the horizontal and vertical shear forces produced by the shear stresses acting on the cross section. The finite-volume method's strength lies in its superior ability to handle heterogeneous microstructures where the satisfaction of interfacial displacement and traction continuity across subdomains with large modulus contrast requires large finite-difference grids, in contrast with the finite-volume method.

The convergence and accuracy of the finite-volume method to the elasticity solution was also confirmed in the study of a composite cross section made up of two symmetrically placed rectangular sections filled with different materials. Comparison with the finite-element results from the literature also showed that the finite-volume results were very close.

The two types of cross sections investigated by the finite-volume method relative to both the finite-difference and finite-element methods confirm the applicability of the extended finite-volume method to torsional structural engineering problems. This provides confidence in the application of this technique to more complicated cross sections involving thin-walled and composite structures investigated in Chapters 4 and 5, respectively.

Chapter 4

4. Critical Assessment of the Membrane Analogy

4.1. Introduction

Prandtl was the first to notice a relationship between torsion and membrane problems, which became the foundation for experimental solutions of torsion problems involving arbitrarily shaped cross sections. This relationship became known as the membrane analogy. Specifically, the differential equation for the stress function in Saint-Venant's torsion problem is of the same form as that describing the deflection of a pressurized membrane, so the shape of that pressurized membrane also describes the Prandtl's stress function surface. The membrane analogy also serves as the basis for approximate analytical solutions to Saint Venant's torsion problems involving narrow or thin-walled closed or open cross sections.

In this chapter, the theoretical basis for the membrane analogy is reviewed and three common types of cross sections in structural engineering are selected for the assessment of the membrane analogy's accuracy in the calculation of torsional rigidity. The solutions to torsion of these cross sections are first conducted by means of the membrane analogy based on the assumption that the wall thickness of the individual components is small enough for the thin rectangular approximation to be valid. The three types of cross sections with different wall thicknesses are then analyzed both by the finite-difference and finite-volume methods. Comparison between results generated by the different methods is conducted with the aim of establishing the range of validity of the membrane analogy.

4.2. The Membrane Analogy

An edge-supported homogenous membrane placed over a plate with a hole illustrates the membrane analogy for the torsion of a solid cross section. The membrane covers exactly the hole cut in the plate, whose shape is the same as that of the cross section of the prismatic bar subjected to torsion in this analogy. The governing differential equation for membrane deflection z is derived from the vertical equilibrium considerations where the weight of the membrane is neglected,

$$\frac{\partial^2 z}{\partial x^2}+\frac{\partial^2 z}{\partial y^2}=-\frac{p}{S} \tag{4.1}$$

In the above equation, p denotes the pressure the membrane subjected to and S is the tensile force per unit membrane length Eq. (4.1) is identified as the Poisson's equation with the Laplacian of the membrane deflection always a constant value. Comparing it with the governing differential equation of Prandtl's stress function Eq. (2.12), it is observed that quantities in these two equations are analogous. Specifically, the Prandtl's stress function ϕ is analogous to the membrane deflection z. The shear module G of isotropic material and the reciprocal of tensile force per unit length S are another analogy pair. In addition, twice the angle of twist per unit length θ is analogous to the pressure p to which the membrane is subjected.

4.2.1. Membrane Analogy for Thin-Walled Open Cross Sections

Applying the membrane analogy to a narrow rectangular cross section shown in Fig. (4.1), it is assumed that the shape of the membrane deflection z is cylindrical along the entire span of the cross section. In other words, the end effects are neglected and no dependence on the x coordinate is assumed.

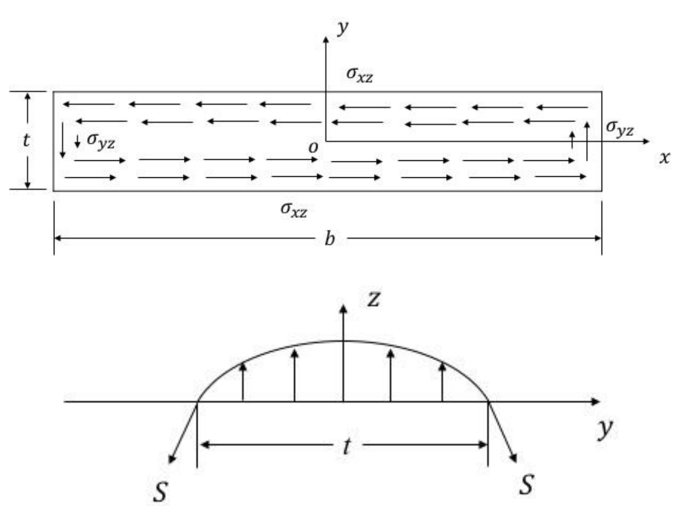

Figure 4.1. Membrane Analogy for a torsional member of narrow rectangular cross section.

Subject to the approximation that $z(y)$ only, and hence $\partial z/\partial x = 0$, Eq. (4.1) may be readily integrated twice to determine the membrane deflection which assumes a parabolic shape. Considering the boundary condition $dz/dy = 0$ at $y = 0$, and $z = 0$ at $y = \pm\, t/2$, the integration of Eq. (4.1) yields the following deflection equation for the narrow rectangular cross section,

$$z = \frac{1}{2}\frac{p}{S}\left[\left(\frac{t}{2}\right)^2 - y^2\right] \tag{4.2}$$

Eq. (4.2) is employed to calculate the volume bounded by the parabolic cylindrical membrane and its projection onto $x - y$ plane

$$V = pbt^3/12S \tag{4.3}$$

Replacing 2θ with p and $1/S$ with G, the resultant torque can be expressed as

$$T = 2V = \frac{1}{3}bt^3G\theta \tag{4.4}$$

where b is the longer edge of the narrow rectangular cross section and t is the shorter edge. Rearranging the above equation, the torsional rigidity for a thin rectangular cross section is

$$C = \frac{T}{\theta} = \frac{1}{3}bt^3G \tag{4.5}$$

Furthermore, the dominant shear stress along the long edge of the rectangular cross section is obtained by differentiating the membrane deflection by y,

$$\tau_{zx} = -\frac{\partial z}{\partial y} = 2G\theta y \tag{4.6}$$

Using Eq. (4.4) to express $G\theta$ in terms of the torque and rectangular cross section’s geometry, the maximum shear, which occurs at $y = \pm t/2$, is obtained as,

$$\tau_{max} = G\theta t = \frac{3T}{bt^2} \tag{4.7}$$

Eq. (4.7) is also applicable to thin-walled open cross sections wherein long rectangular members can be identified. For such cross sections, the torsional rigidity can be approximated as the sum of the individual torsional rigidities of the individual members,

$$J_e = \sum \frac{1}{3} b t^3 \tag{4.8}$$

The validity of this method depends on the similarity between the parabolic membrane shape and that of the geometry of each component section. Note that the exceptions of this application are those points near the corners of the cross section, since the effect of stress concentration is neglected in the membrane analogy.

4.2.2. Membrane Analogy for Thin-Walled Closed Cross Sections

The membrane analogy may also be applied to thin-walled multiply-connected (or closed) cross sections based on additional assumptions. Inside hollow areas, the stress must be zero because no material is there. This zero-stress requirement may be consequently satisfied by a constant ϕ over the hollow area. Therefore, each inner boundary is a line of constant ϕ characterized by a different value for multiply-connected regions. The absolute value of ϕ is meaningless, and ϕ at one boundary can be equated to zero and the others then are adjusted accordingly. By convention, this zero ϕ boundary is usually assigned as the outermost boundary of the cross section.

The membrane representing the thin-wall cross section area is attached to the outer boundary of the fixed cross section and the inner weightless plates which have the exact same shapes as each of the voided areas. The membrane is then pressurized, bridging the inner and outer contours over a short distance t. One assumption for thin-walled closed cross sections is the constant shear stress τ over the given thickness t, since the shear stress represents the slope of h, the resisting force per unit length along the mean perimeter, yielding

$$\tau = \frac{h}{t} \tag{4.9}$$

The difference of the membrane deflection on the outer and inner contour z is the counterpart of h in the membrane analogy. The thickness of the thin-walled cross section may vary circumferentially, however, Eq. (4.9) still holds true for every infinitesimal circumferential section. The mean perimeter enclosing an area A is used to determine the volume bounded by the membrane. Thus, the analogy gives the torque expression

$$T = 2Ah \tag{4.10}$$

If the thickness of the thin wall is a constant, combining Eq. (4.8) and Eq. (4.9), the uniform shear stress is

$$\tau = \frac{T}{2At} \tag{4.11}$$

Vertical equilibrium yields

$$pA = \oint \left(\frac{h}{t}S\right) ds \Longrightarrow \frac{p}{S} = \frac{h}{A}\oint \frac{ds}{t} \tag{4.12}$$

where s is the length of the mean perimeter of the thin-walled cross section.

In the thin-walled structure, $\tan\left(\frac{h}{t}\right) \approx \frac{h}{t}$, because the difference in the membrane deflection along the outer and inner contour is relatively smaller than the thickness of the thin wall t. Substituting the other analogous pairs, p with θ, and $1/S$ with G,

$$2G\theta = \frac{1}{A}\oint \tau \, ds \tag{4.13}$$

Rearranging the Eq. (4.13), the angle of twist per unit length is expressed in terms of the uniform shear stress. Eq. (4.11) and Eq. (4.13) are known as Bredt's formulae.

4.2.3. Structural Problems Solved by Membrane Analogy

With the help of the membrane analogy, the torsional rigidity of thin-walled open cross sections consisting of several narrow rectangular members can be easily calculated by using Eq. (4.8), where the shear stress resultant is theoretically at its maximum in the middle of the longer edge of each rectangular section. Eq. (4.7) can be used to calculate the maximum shear stress resultant either given the angle of twist or the applied torque.

As for closed rectangular cross sections, a table in *Advanced Strength and Applied Elasticity (Ugural and Fenster)* presents membrane analogy based calculations for the shear stress and angle of twist values for hollow rectangular cross sections subject to torsion for reference.

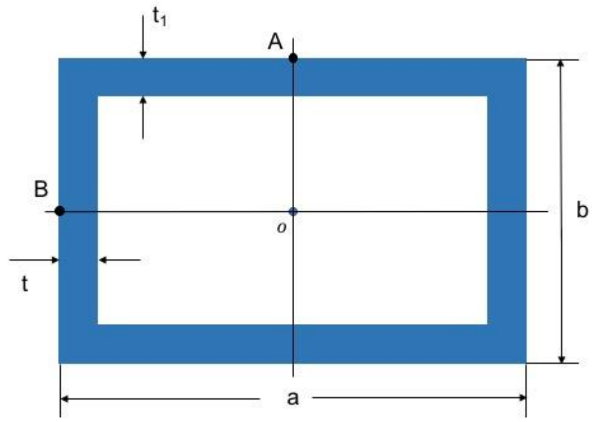

Figure 4.2. Depiction of a general hollow rectangular cross section.

Using the membrane analogy, the torque and angle of twist per unit length θ relationship is obtained in the form,

$$T = \frac{2tt_1a^2b^2G\theta}{at + bt_1} \tag{4.14}$$

Membrane analogy also indicates that the maximum shear stress resultant of this sort of hollow rectangular cross sections is always in the middle of its outermost edges without shear stress variation along the thickness. Taking advantage of the relationship between the angle of twist per unit length and torque, Eq. (4.14), the maximum shear stress occurs on the horizontal or vertical outermost edge. The corresponding expressions are,

$$\tau_A = \frac{tabG\theta}{at+bt_1} \qquad \tau_B = \frac{t_1abG\theta}{at+bt_1} \tag{4.15}$$

4.3. Critical Assessment

T-beams, channel-beams, and box-beams are three commonly used types of beams in structural engineering. These beams sometimes are subjected to twist in practice, which may be modeled as a pure torsion problem. The analysis of a T-beam, channel-beam and box-beam subjected to Saint Venant's torsion is first conducted numerically using the developed FVM and FDM approaches. In order to evaluate the effect of the wall thickness of the structure on torsional rigidity and maximum shear stress, each type of cross section with three different thicknesses are analyzed. The membrane analogy may be used to approximate torsional rigidity and maximum shear stress resultant for each T-beam, channel-beam and box-beam, if the thickness of the structure is small enough compared to their full dimension as the assumption basis. In this section, the FVM and FDM analyses are employed to determine the limits of applicability of the membrane analogy regarding both the torsional rigidity estimate as well as the maximum shear stress resultant magnitudes and locations. This involves an examination of the full-field shear stress distributions.

All cross sections analyzed in this section are homogenous and isotropic. Moreover, the same shear modulus is employed in the analyses of each cross section. Since the shear stress resultant is directly dependent on the shear modulus, it is convenient to introduce the non-dimensional shear stress resultant $\tau(x, y)$ as the ratio of shear stress resultant $\tau_{resultant}(x, y)$ and the shear modulus G. Furthermore, the angle of twist per unit length also appears as a linear coefficient in the expressions for torsional rigidity and shear stress resultant, so the results are also normalized by the angle of twist. Hence the normalized results have to be multiplied by the applied angle of twist to obtain actual values.

4.3.1. T-Beam Cross Section

The cross section of a T-beam is made up of two perpendicular rectangular members. The $x - y$ coordinate system coincides with the centroid of each cross section and hence needs to be re-calculated when the flange and web wall thickness is changed, which is done uniformly. However, the centroid locations change very little with decreasing wall thickness. Both the flange and web portions of the T-beam are discretized into uniform square subvolumes, with 40 subvolumes spanning the thickness of each member initially set at 2, and then decreased to 1.5, 1.0 and 0.5. The discretizations for each wall thickness were carried out such that the subvolume/grid density was preserved for each cross section. Fig. (4.3) illustrates the two T-beam cross sections with the thickest and thinnest member walls.

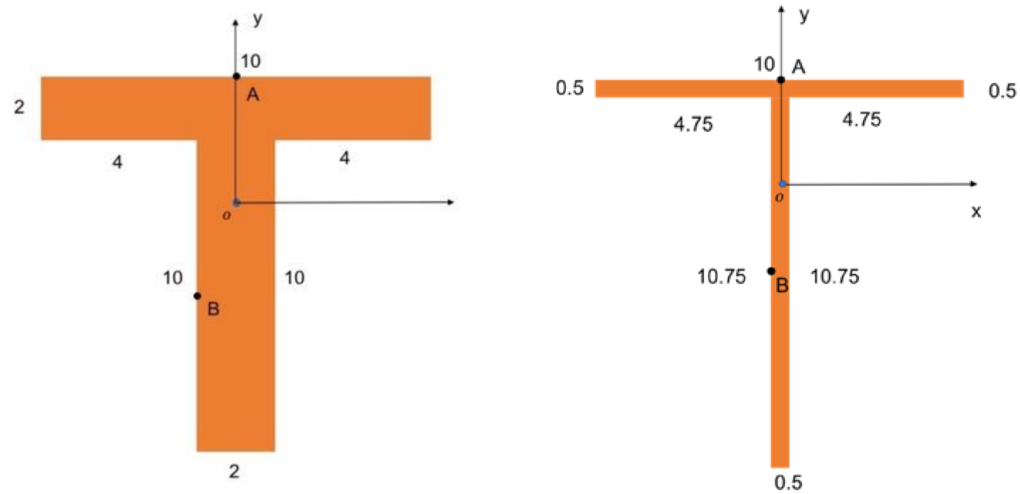

Figure 4.3. Schematics of T-beam cross sections with wall thickness of 2 (left) and 0.5 (right).

The finite-difference and finite-volume methods were employed to generate the shear stress fields from which the shear stress resultant distributions were calculated. These distributions were also employed to calculate the torsional rigidity using Eq. (2.10). The distributions include shear stresses calculated along the cross-section's boundary. Fig. (4.4) and Fig. (4.5) compare the shear stress resultant distributions generated using the FDM and FVM approaches for the thickest and thinnest wall thicknesses, respectively. As observed, both numerical methods predict very similar distributions characterized by stress concentrations at the re-entrant corners of the T-section formed by the intersection of the flange and the web. At the remaining corners, the shear stress resultants vanish as required by the traction-free boundary conditions. With the exception of the corner regions, the shear stress resultant distributions are nearly uniform along the boundaries of the flange for both configurations, as approximated by the membrane analogy. The region over which the uniform shear stress resultant occurs is greater for the thinnest wall cross section, confirming the membrane analogy approximation for open cross sections with long rectangular members. Greater differences in the shear stress distributions between the two T-beam cross sections are observed along the flange boundary, where substantial departures from uniform distribution occur for the largest wall thickness of 2.0. Specifically, the maximum shear stress resultant along the upper flange boundary occurs in the middle and decreases slowly to a nearly uniform value with increasing distance towards the flange ends. As the flange thickness decreases to 0.5 this maximum value remains in the middle of the flange, but its influence is limited to this region with the rest of the upper flange boundary experiencing uniform shear stress distribution.

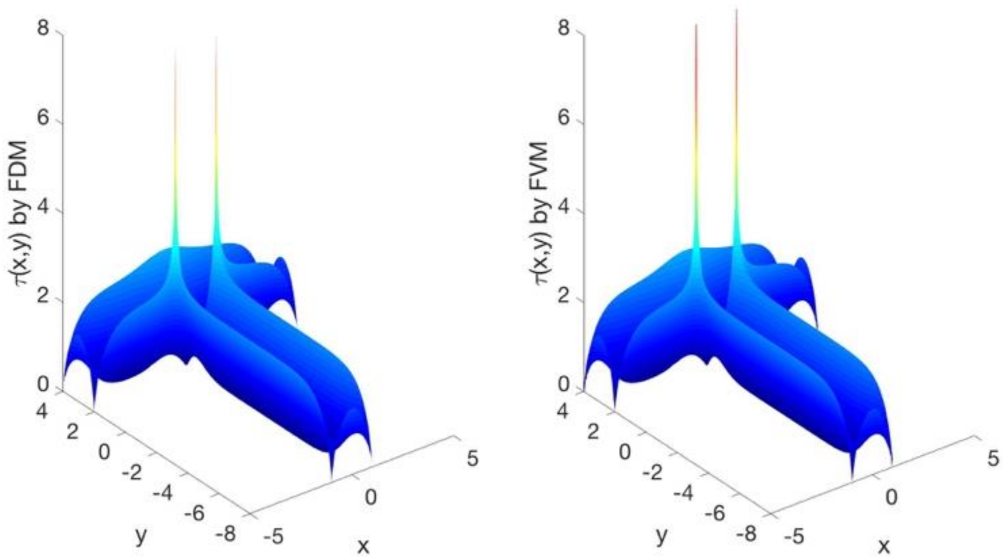

Figure 4.4. Distributions of shear stress resultant generated by the FDM & FVM approaches for a T-beam with wall thickness of 2.0.

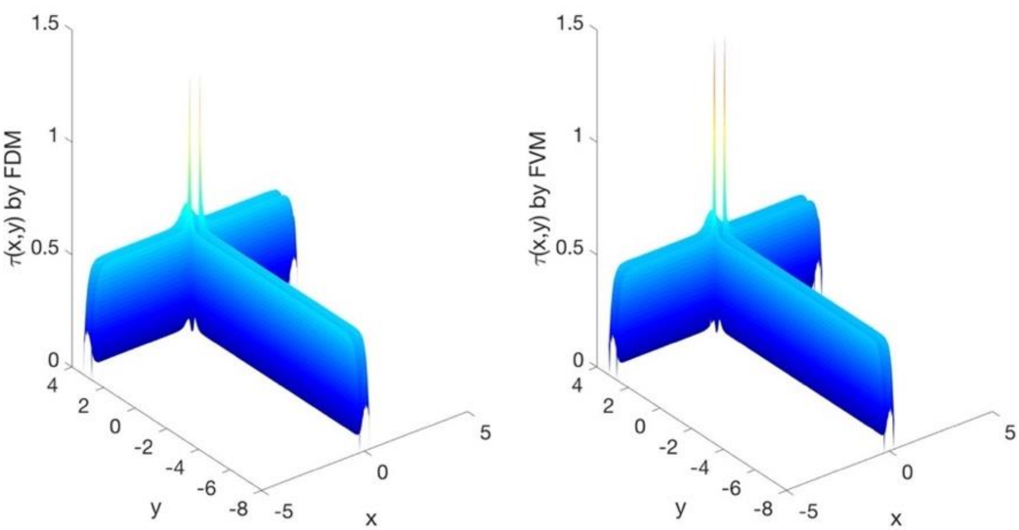

Figure 4.5. Distributions of shear stress resultant generated by the FDM & FVM approaches for a T-beam with wall thickness of 0.5.

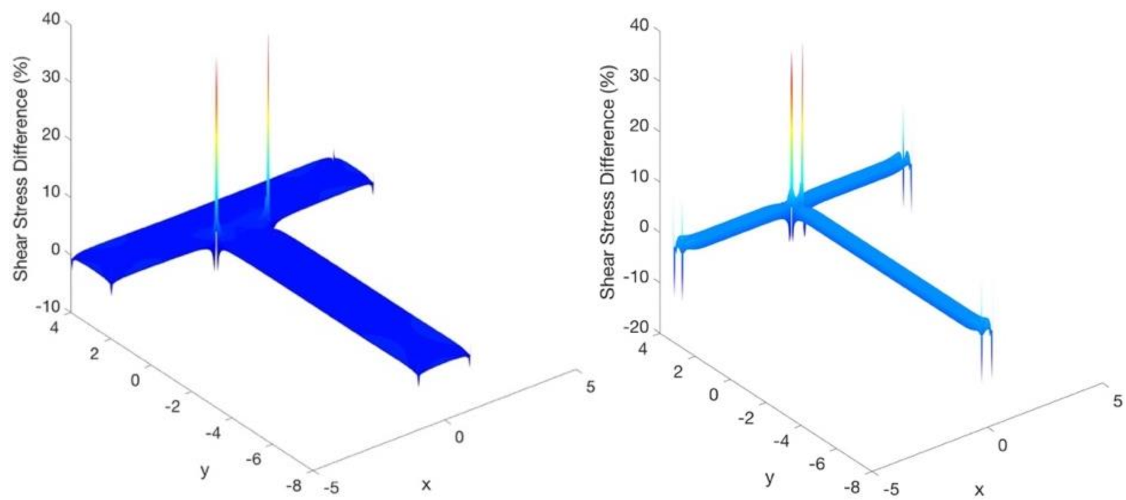

Figure 4.6. Differences in the shear stress resultant distributions between FDM & FVM results for T-beam cross sections with wall thickness of 2.0 (left) and 0.5 (right).

The shear stress resultant distributions predicted by the two numerical methods differ only in the immediate vicinity of the corners, both external and re-entrant. In particular, the FVM calculations produce greater stress concentrations at the re-entrant corners and much smaller (nearly zero) shear stress resultants at the external corners relative to the FDM approach for the two T-beam cross sections with the largest and smallest flange/web thickness. These differences in the full-field distributions are illustrated in Fig. (4.6). They were generated by calculating point-wise differences between the two methods and then normalizing by the maximum shear stress resultant obtained by the FVM approach according to,

$$d(x,y) = \left(\tau_{FVM}(x,y) - \tau_{FDM}(x,y)\right)/max\left(\tau_{FVM}(x,y)\right) \times 100\% \qquad (4.16)$$

As observed in the figure, the substantial differences in the shear stress resultants predicted by the two methods are positive at the re-entrant corners and their vicinity, and positive or negative at the external corners. These difference distributions support the preceding statement that the FVM approach generates higher stress concentrations at the re-entrant corners. The occurrence of the large stress concentrations at the re-entrant corners seen in the above figures is discussed in the sequel.

The membrane analogy assumes that the shear stress distribution is uniform along the perimeter of a long rectangular member except near the ends or connections with other sections, as indeed observed in Fig. (4.5) for the smallest flange/web wall thickness. However, even in this case, the stress concentrations at the re-entrant corners do not vanish, requiring further analysis based on elasticity considerations. In the case of a circular shaft with a square cutout at the outer radius with two 90-degree (re-entrant) corners, the shear stress field is singular as reported by Sinclair (2004). The shear stress field has a singularity of the order of -1/3 characterized by the variation $Tr^{-1/3}$ where the distance r is measured from the corner using a local coordinate system and T is the applied torque. Therefore, the local or dominant shear stress dependence on the distance r from the re-entrant corner exhibits a linear dependence when graphed as $ln(\sigma)$ versus $ln(r)$ with the slope of -1/3. It is reasonable to assume that the same functional dependence occurs in the immediate vicinity of the re-entrant corners for the T-beam.

For the T-shape cross section, there are two singular points at the re-entrant corners formed by the flange and web intersections. Only one of them is analyzed because the other one is symmetric about the centerline of the web. Fig. (4.7) and Fig. (4.8) illustrate the local shear stress resultant dependence on the distance from the re-entrant corner along the flange and web boundaries of the two cross sections predicted by the two numerical approaches. Along the bottom surface of the flange, the shear stress resultant τ is in fact σ_{xz} whereas along the left surface of the web it is σ_{yz}. The results have been graphed for both τ vs r and $ln(\tau)$ vs $ln(r)$ to investigate whether the near-corner behavior is indeed singular, characterized by the -1/3 order singularity. Included in the graphs of $ln(\tau)$ vs $ln(r)$ in both figures are straight lines with the slope of -1/3 for comparison with the predicted results. As observed, the calculated shear stress resultants exhibit behavior at the re-entrant corners that is singular for both cross sections regardless of the wall thickness. This behavior is outside of the membrane analogy assumptions and may affect the torsional rigidity and maximum non-singular shear stress calculations for sufficiently thick flange and web walls.

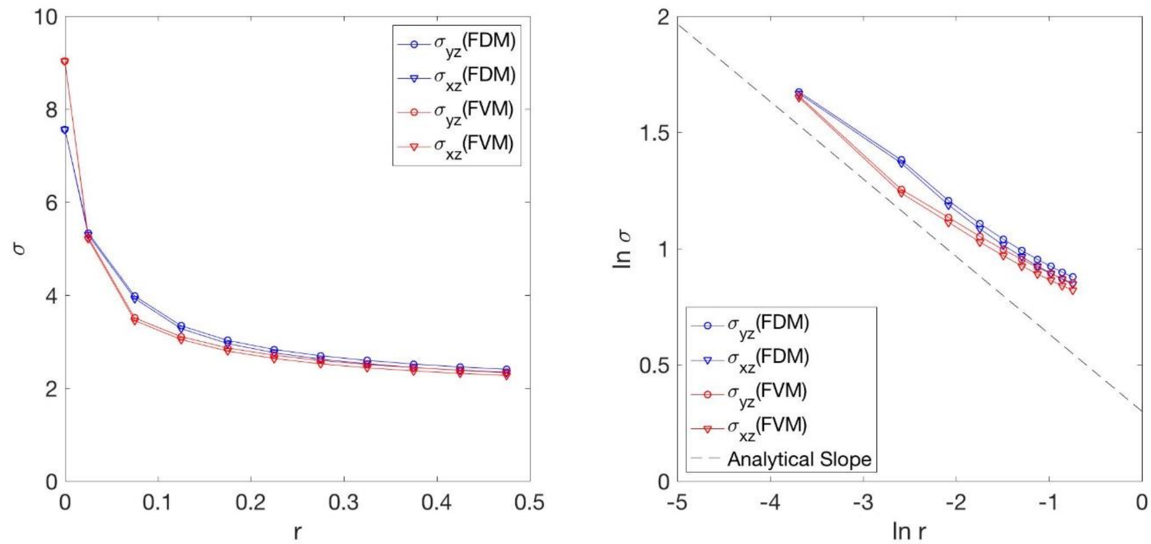

Figure 4.7. Shear stress resultants versus distance from the re-entrant corner (left) and the corresponding logarithmic counterparts (right) for a T cross section with wall thickness of 2.0.

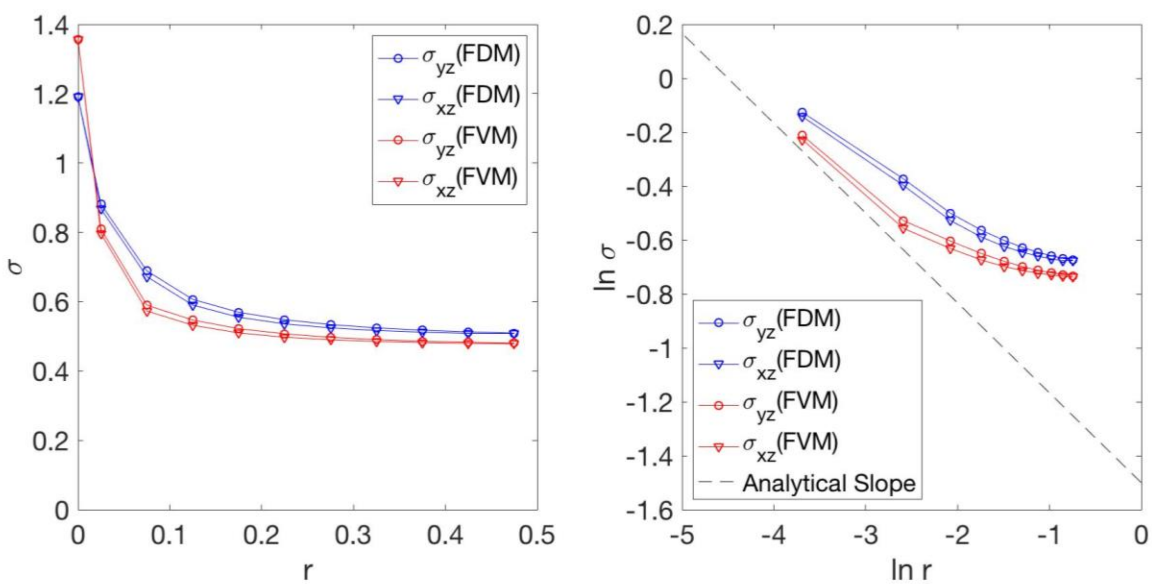

Figure 4.8. Shear stress resultants versus distance from the re-entrant corner (left) and the corresponding logarithmic counterparts (right) for a T cross section with wall thickness of 0.5.

The results for the remaining two cross sections with the flange and web wall thickness of 1.5 and 1.0 follow the trends consistent with those presented in the foregoing. Specifically, the shear stress resultant distributions become more uniform along the long dimensions of the flange and web members of the T-beam with increasing wall thickness, with the order of shear stress singularity at the re-entrant corners remaining the same.

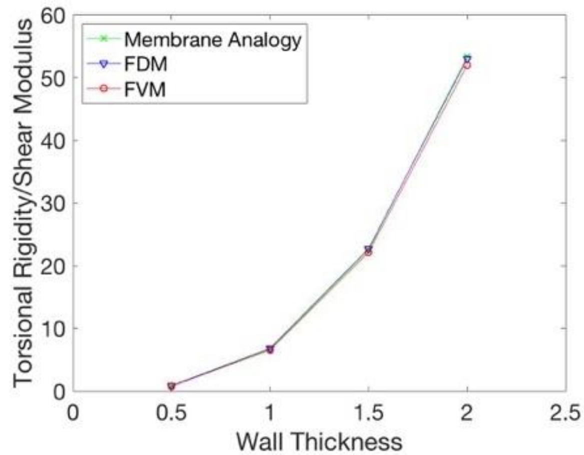

Figure 4.9. Torsional rigidity for the T cross section as a function of the flange/web wall thickness.

The torsional rigidity of the T-beam cross section as a function of the flange/web wall thickness calculated using the two numerical methods is compared with the corresponding membrane analogy results in Fig. (4.9). Interestingly, there is very little difference between the results based on the detailed numerical calculations which exhibit large stress gradients and magnitudes and the approximate membrane analogy based on shear stress fields that do not vary along the flange and web lengths. Hence the membrane analogy appears to hold for aspect ratios (length over thickness) as large as five in the case of T-beam cross sections. The same conclusions do not apply in its entirety for the calculation of non-singular maximum shear stress resultants as illustrated and discussed in the sequel.

Fig. (4.10) presents a comparison of the non-singular maximum shear stress magnitudes that occur in the flange and web at points A and B, respectively, halfway along the members' lengths, see Fig. (4.3), as a function of the wall thickness. In contrast with the torsional rigidity comparison, the membrane analogy underestimates the shear stress resultant at point A of the flange to an extent that depends on the flange/web thickness. For the wall thickness of 2.0, the difference is approximately 17%. This error decreases with decreasing wall thickness as expected, and becomes small, but not zero, when the wall thickness is 0.5. Apparently, the proximity of the flange/web junction to point A affects the local shear stress resultant. On the other hand, the membrane analogy predicts accurately the non-singular maximum shear stress resultant at the point B of the web for the four analyzed wall thicknesses because it is sufficiently removed from the junction and hence not affected by it to the same extent as the point A.

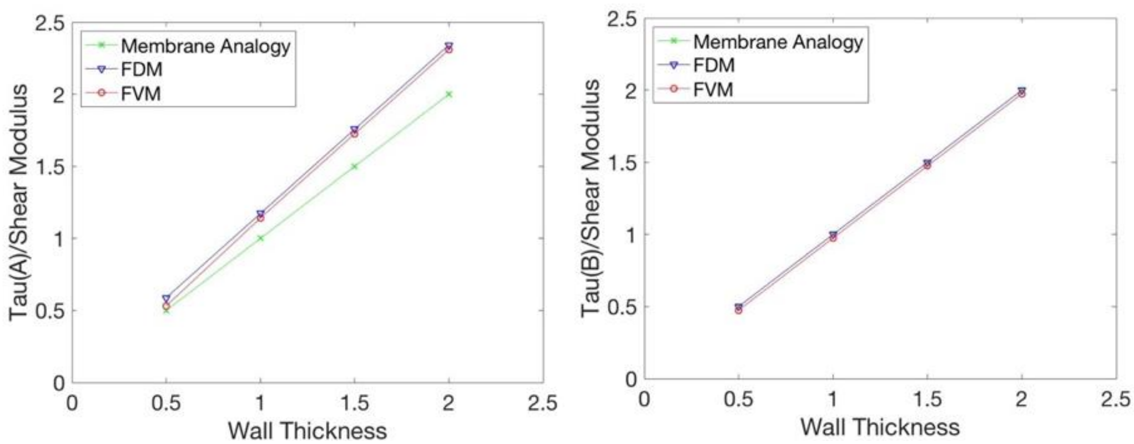

Figure 4.10. Maximum shear stress at the points A (left) and B (right) of the T-beam cross section as a function of the wall thickness.

4.3.2. Channel-Beam Cross Section

Channel-beam cross sections are made up of three rectangular sections connected at right angles. Fig. (4.11) illustrates two channel-beam cross sections with the largest and smallest wall thickness of 2.0 and 0.5, respectively, analyzed using the FDM and FVM approaches for comparison with the membrane analogy predictions. The centroid of the cross section with the largest wall thickness lies at the intersection of the right boundary of the web and the cross section's horizontal plane of symmetry, whereas the thinnest cross section's centroid lies outside. The centroids also coincide with the center of twist and hence the origin of the $x - y$ coordinate systems as verified by summing up the forces along the x and y directions produced by the corresponding shear stresses. As in the case of the T-beam cross section, the analyzed channel-beam cross sections have been discretized using square subvolumes, with 40 subvolumes spanning the cross section with the largest flange and web wall thickness. The remaining cross sections were discretized such that the same subvolume density was retained in each case.

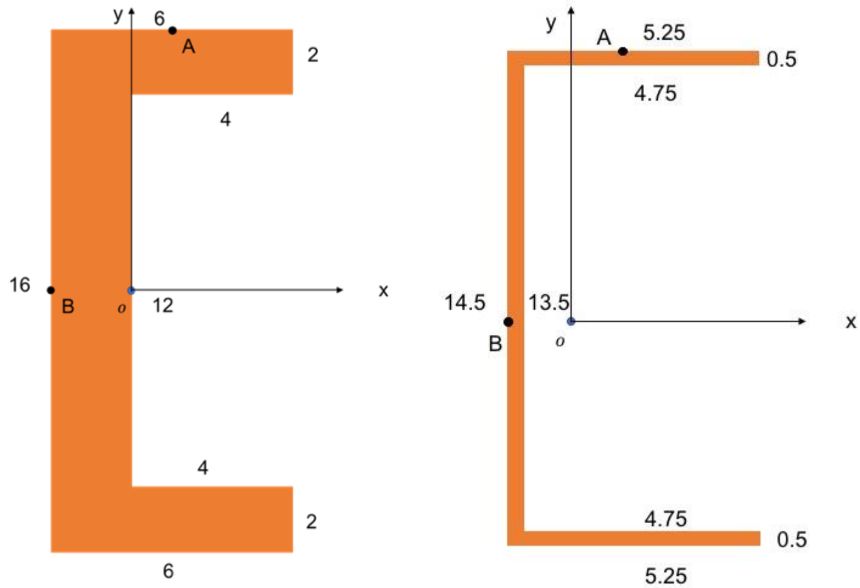

Figure 4.11. Schematics of channel-beam cross sections with wall thickness of 2 (left) and 0.5 (right).

Fig. (4.12) and Fig. (4.13) present full-field distributions of the shear stress resultant in the thickest and thinnest channel-beam cross sections calculated using the finite-difference and finite-volume methods. Similar to the T-beam cross sections, large stress concentrations are evident at the re-entrant corners which indicate shear stress singularities that are not taken into account by the membrane analogy. At the remaining corners, the shear stress resultant vanishes as expected. The finite-difference method underestimates the magnitude of the shear stress resultant at the re-entrant corners relative to the finite-volume method, as also observed in the T-beam results. Hence the differences in the point-wise shear stress distributions defined in Eq. (4.14) and illustrated in Fig. (4.14) are positive at these points and negative at the external corner, indicating that the traction-free boundary condition in these locations is better satisfied by the finite-volume method.

The shear stress resultant distributions for cross sections with intermediate flange and web wall thickness of 1.5 and 1.0 exhibit similar trends and hence they are not shown. The same mesh density was also employed in analyzing their response. Torsional rigidity and maximum shear stress resultant of these cross sections will be employed in the sequel for comparison with the membrane analogy predictions.

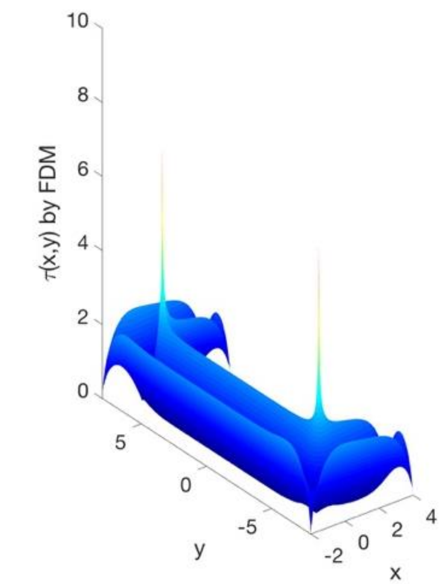

Figure 4.12. Distributions of shear stress resultant generated by the FDM & FVM approaches for a channel-beam with wall thickness of 2.0.

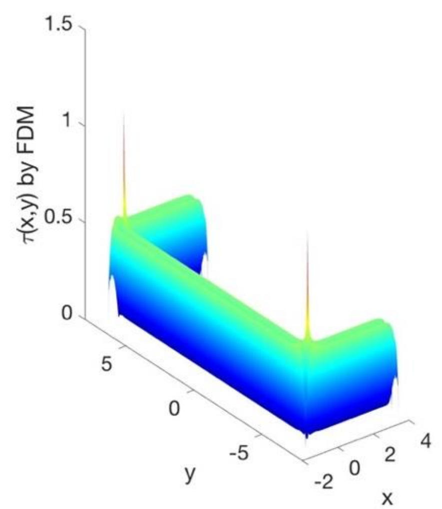

Figure 4.13. Distributions of shear stress resultant generated by the FDM & FVM approaches for a channel-beam with wall thickness of 0.5.

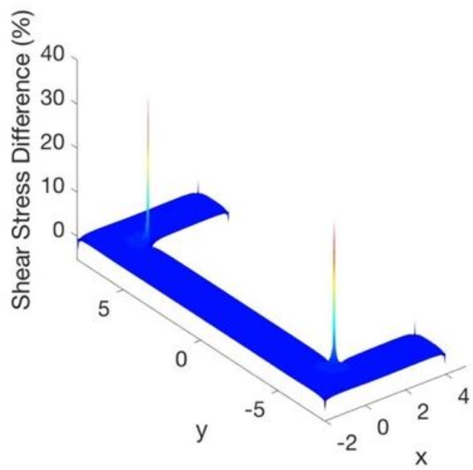

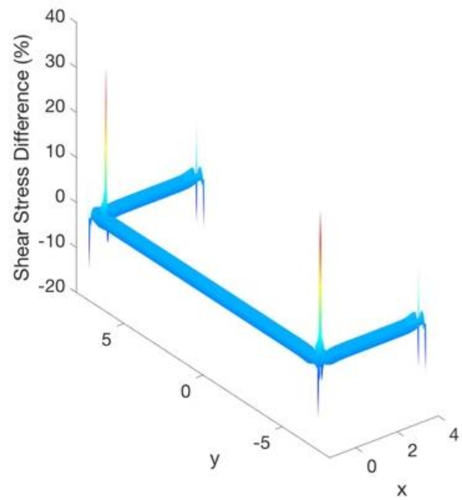

Figure 4.14. Differences in the shear stress resultant distributions between FDM & FVM results for channel-beam cross sections with wall thickness of 2.0 (left) and 0.5 (right).

The full-field shear stress resultant distributions for the thickest cross section, Fig. (4.12), are more uniform along the long dimensions of the individual members of the channel-beam, in contrast with the distributions observed in Fig. (4.4) for the corresponding T-beam cross section. Apparently, the singular-like shear stress behavior in the re-entrant corner regions does not have as much effect on the stress distributions along the top and bottom flanges as in the case of the T-beam. As the wall thickness decreases to 0.5, Fig. (4.13), the distributions become nearly uniform, with the deviations occurring in the immediate vicinity of the re-entrant and external corners. These results suggest that the torsional rigidity and non-singular maximum shear stress differences between the numerical and membrane analogy results will be very small in the range of the analyzed flange and web wall thicknesses.

The torsional rigidity and maximum shear stress resultants at points A and B calculated using the two numerical methods as a function of the member wall thickness are compared with the corresponding membrane analogy results in Fig. (4.15) and Fig. (4.16). As suggested by the preceding stress distributions, there is indeed very little difference between the three sets of results, indicating that the membrane analogy is applicable for channel-beams even when the member wall thickness is as large as 2.0 for the investigated channel-beam configuration. In contrast with the T-beam cross section, the shear stress resultant in the middle of the top/bottom flange (point A) is as accurately predicted as that in the middle of web edge (point B) due to little variation along the members' lengths.

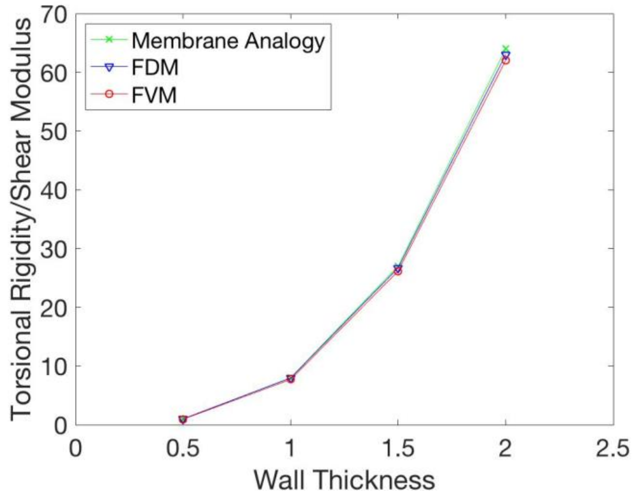

Figure 4.15. Torsional rigidity for the channel cross section with different thickness.

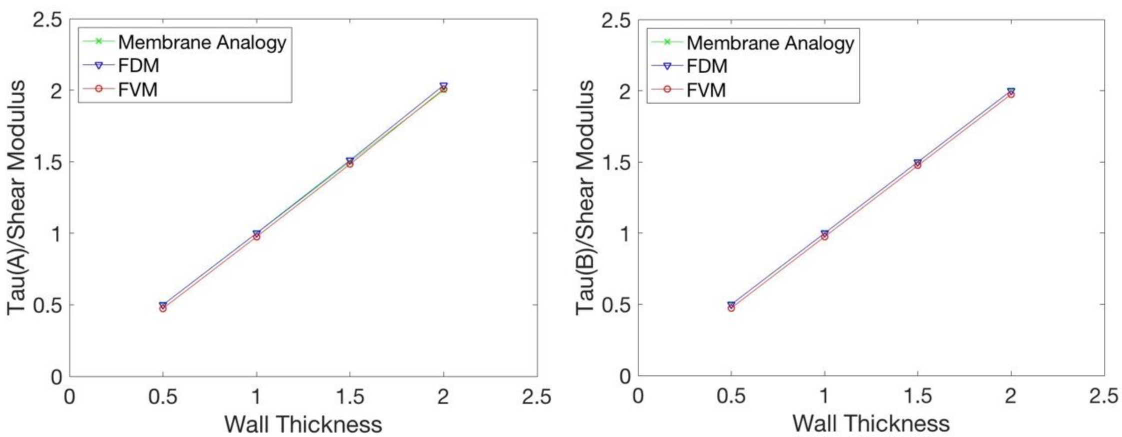

Figure 4.16. Maximum shear stress (left & right) for the channel beam cross sections with different wall thickness.

4.3.3. Box-Beam Cross Section

The last cross section analyzed for comparison with the membrane analogy is a box-beam made up of four rectangular members (two flanges and two webs) to produce a square hollow cross section. Fig. (4.17) illustrates two such configurations with the largest and smallest wall thickness of 2.0 and 0.5, respectively. The two remaining configurations analyzed had wall thicknesses of 1.5 and 1.0. Because of symmetry, the origin of the $x - y$

coordinate system coincides with the cross-section's centroid. The wall thickness of the four configurations was adjusted such that the distance from the origin of the coordinate system to the middle of each member remained the same. Hence the dimensions *a* and *b* that appear in the relations torque vs angle of twist and shear stress resultants at points A and B vs angle of twist, Eqs. (4.14)-(4.15), respectively, for the four configurations analyzed do not change. As for the T-beam and channel-beam configurations, uniform square subvolumes were employed in the cross sections' discretizations, with 40 subvolumes along the largest wall thickness of 2.0, with the smaller wall thickness discretized so as to maintain the same subvolume density.

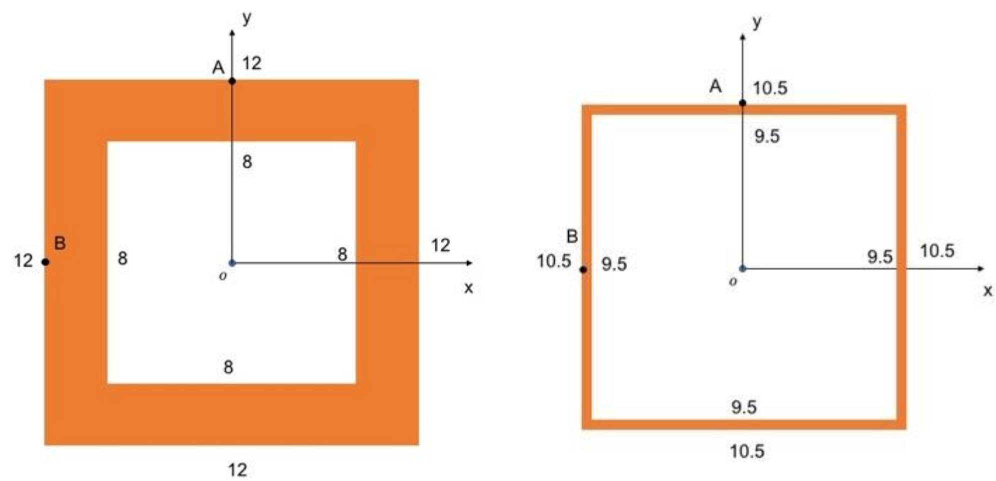

Figure 4.17. Schematics of box-beam cross sections with wall thickness of 2 (left) and 0.5 (right).

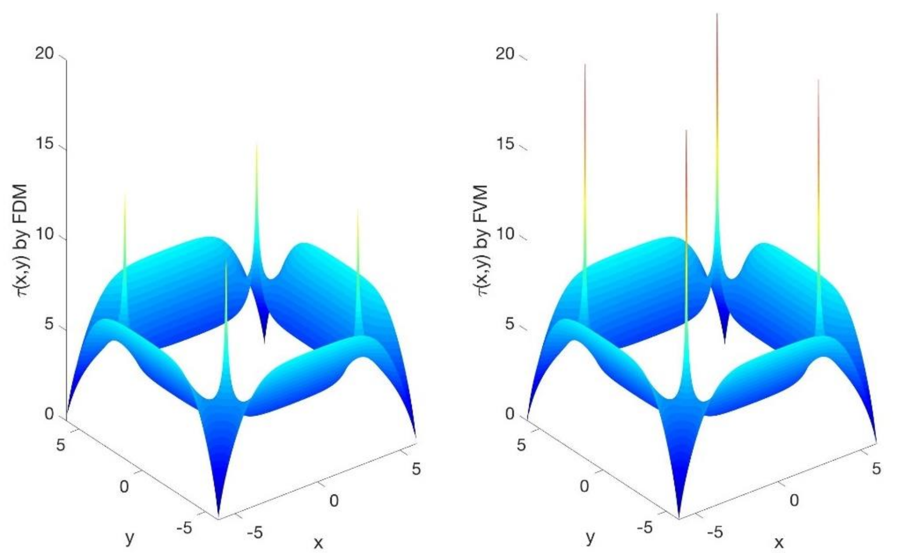

Figure 4.18. Distributions of shear stress resultant generated by the FDM & FVM approaches for a box-beam with wall thickness of 2.0.

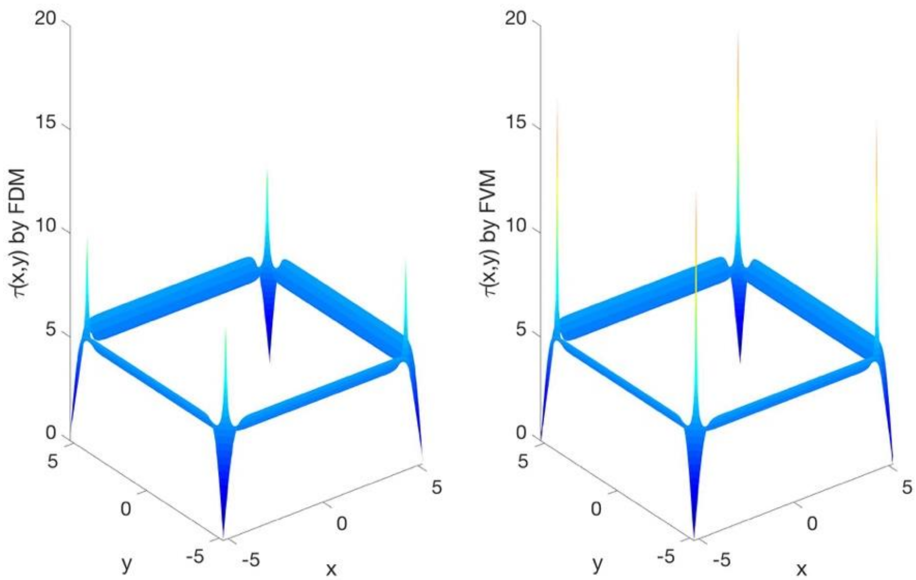

Figure 4.19. Distributions of shear stress resultant generated by the FDM & FVM approaches for a box-beam with wall thickness of 0.5.

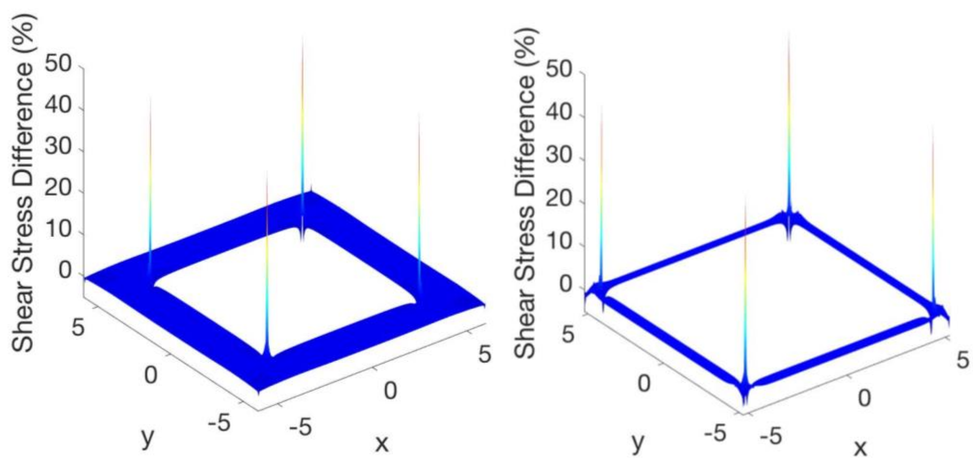

Figure 4.20. Differences in the shear stress resultant distributions between FDM & FVM results for box-beam cross sections with wall thickness of 2.0 (left) and 0.5 (right).

Fig. (4.18) and Fig. (4.19) present full-field distributions of the shear stress resultant in the thickest and thinnest channel-beam cross sections calculated using the finite-difference and finite-volume methods. Cross sections with wall thickness of 1.5 and 1.0 produced similar results. For both configurations, the stress concentrations at the re-entrant corners predicted by the finite-volume method are substantially larger than those predicted by the finite-difference method. These differences do not appear to depend on the member wall thickness as seen in Fig. (4.20) which illustrates the differences in the shear stress resultant distributions between the two techniques.

The presence of four external and re-entrant corners has a larger effect on the uniformity of shear stress resultant distributions along the individual members of the thickest wall box-beam than of the thinnest. The effect is limited to the corner regions whereas elsewhere the shear stress distribution along the lateral boundary is uniform. Nonetheless, because the corner influence extends further into the box-beam's members of the thickest wall configuration, its effect on the torsional rigidity relative to the membrane analogy prediction will be noticeable. This is indeed the case as observed in Fig. (4.21) which illustrates the relationship between torque and wall thickness predicted by the two numerical methods and the membrane analogy. The difference between the numerical methods and membrane analogy approximation does not vanish until the wall thickness decreases to 0.5, in contrast with the corresponding results for the T-beam and channel-beam cross sections. It is also worthwhile to point out that while the torsional rigidity vs wall thickness dependence is nonlinear for the T-beam and channel-beam cross sections, the membrane analogy predicts a linear relationship with the wall thickness, Eq. (4.14) when the dimensions *a* and *b* are kept the same for each configuration. This is indeed the case as observed in Fig. (4.21). The finite-difference and finite-volume calculations also predict a nearly linear relationship, albeit with a somewhat different slope producing deviations from the membrane analogy predictions until the wall thickness becomes 0.5.

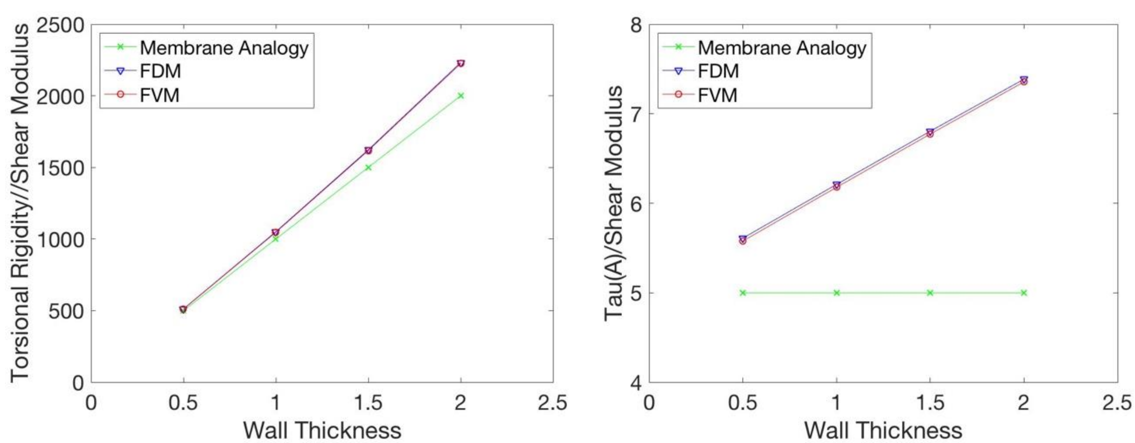

Figure 4.21. Torsional rigidity (left) and maximum shear stress (right) for the box-beam cross sections with different wall thickness.

Fig. (4.21) also includes a comparison of the non-singular maximum shear stress resultants at points A and B situated in the middle of the flange and web members of the box-beam predicted by the two numerical methods and the membrane analogy. Because of symmetry, points A and B produce the same shear stress resultant magnitudes. Moreover, because the box-beam is square and the dimensions a and b remain fixed as the wall thickness decreases, the membrane analogy predicts no variation of the shear stress resultants at those points with wall thickness, Eq. (4.15). In contrast, both numerical techniques indicate a linear decrease with decreasing wall thickness of the shear stress resultants at the two locations, with substantial deviations from the membrane analogy predictions at larger wall thicknesses. Even for the thinnest wall box-beam configuration, the difference is substantial, illustrating the membrane analogy limited applicability for this particular cross section.

4.4. Summary and Discussion

For each set of the analyzed T-beam, channel-beam and box-beam cross sections, the finite-difference and finite-volume methods produce comparable results for the shear stress resultant distributions and the ensuing torsional rigidity. In addition, both methods are capable of capturing the singular stress field character at re-entrant corners of the analyzed cross sections with sufficiently refined discretization or meshing. However, the finite-volume method yields 35% to 45% larger shear stress values at those singular points relative to the finite-difference calculations. The singular character of the shear stress field at the re-entrant corners was determined by graphing the shear stress values along the lateral boundaries of the flange and web members with decreasing distance from the corner, and subsequently demonstrated to possess an -1/3 order singularity consistent with the reported elasticity results. The higher shear stress resultants directly at the corner calculated by the finite-volume method are likely due to the better approximation of the traction-free boundary condition relative to the finite-difference method which requires the use of fictitious nodes outside of the cross section in approximating partial derivatives of the warping function along the boundary. While outstanding differences exist at the re-entrant corners of the analyzed cross sections, the shear stress fields obtained from the finite-difference and finite-volume calculations are essentially the same outside of these regions.

Although the membrane analogy cannot capture the singular-like stress fields at re-entrant corners of the investigated configurations, it is still a good tool in estimating the torsional rigidity and non-singular maximum shear stress resultants. For the T-beam and channel-beam cross sections, no significant differences were observed for the torsional rigidity calculations using the two numerical and membrane analogy approaches for the entire range of wall thicknesses considered. The torsional rigidity for the box-beam cross section was underestimated by the membrane analogy for larger wall thicknesses, but the differences became increasingly smaller as the walls became progressively thinner.

The non-singular maximum shear stress resultants calculated using the membrane analogy are also generally accurate. For the T-beam cross sections, no differences were observed at the midpoint of the web member in the range of wall thicknesses considered, whereas the differences decreased with decreasing wall thickness at the mid-point of the flange member. For the channel-beam configurations, the membrane analogy predictions practically coincided with the numerical results at the corresponding midpoints in the entire range of wall thicknesses. The box-beam configuration was the only exception where substantial differences in the shear stress resultant at the flange/web midpoints were observed even for the thinnest wall configuration. This indicates that each analyzed cross section shape exhibits its only behavior and needs to be analyzed independently.

Although the membrane analogy does not account for singular stress fields which may influence the results of torsional rigidity calculations to some extent, and to a greater extent failure initiation, it is still a useful alternative for estimating torsional rigidity and non-singular maximum shear stress resultants of thin-walled structures with a reasonably tolerable error. Hence the membrane analogy has its own place in solving torsion problems involving differently shaped cross sections, and is particularly attractive in design because of easy and simple calculations which yield good estimates of torsional rigidity and non-singular maximum shear stress resultants in the absence of exact elasticity solutions.

Chapter 5

5. Composite Cross Sections

5.1. Introduction

Cross sections comprised of homogeneous isotropic materials, including those with thin walls, have been analyzed in the previous chapter. The finite-volume formulation presented in Chapter 2 is also capable of dealing with the torsion of orthotropic material cross sections, whereas the finite-difference solution approach is more suitable for isotropic materials. In fact, the finite-volume technique had been originally developed for the analysis of heterogeneous materials wherein the displacement and traction continuity conditions are explicitly satisfied in a surface-averaged sense between adjacent subvolumes, including any two adjacent subvolumes with different material properties. In contrast, the finite-difference and finite-element techniques require some special treatments at the interfaces separating domains comprised of different materials, which are not as easy to apply as in the finite-volume formulation.

Members made up of composite materials have wide-ranging applications in the structural industry. For instance, reinforced concrete beams or columns are typical composite sections where structural steel arrangement is embedded in a concrete matrix. Recently, light mixed materials with high strength or steel panels have been combined with traditional concrete beams as bridge girders. These reinforced concrete members, which serve as main structural components, are usually subjected to tension, compression, bending and shearing. However, torsion may also act in combination with any of these loadings. Sometimes torsion plays a secondary role if, for example, the external loading does not pass through the shear center of a beam. Because torsion is not regarded as such an important part of structural design like bending, its impact in design is typically absorbed in the overall safety factor. However, structural engineers often design structural members to resist torsion when the resultant torques produce the dominant loading effect, such as eccentrically loaded spandrel beams and helical stairway slabs. Thus, it is essential to analyze the torsional behavior, such as shear stress distribution and torsional rigidity, of these members with transverse torsional reinforcement.

In this chapter, the finite-volume method is employed to analyze the effect of strengthening concrete members with different cross sections to resist torsion using different types of reinforcement, focusing on the stress fields and torsional rigidity. Note that, following the validation results presented in Chapter 3, uniform square mesh continues to be employed to ensure reliable results and fast convergence rates.

5.2. Open Cross Sections with Isotropic Reinforcement

For homogenous isotropic cross sections, the center of twist is sometimes defined as the point at rest in every cross section of a bar in which one end is fixed and the other twisted by a couple. The out-of-plane displacement components depend on the center of twist, about which the cross section rotates during twisting. However, note that while the center of twist is referred to in the derivations of the basic relationships, it is not dealt with explicitly in the solution of shear stress or torsional rigidity (*Page 244, Ugural and Fenster, 2003*). Since the Prandtl's stress function is not altered by a shift of the origin from the center of twist to any point within the cross section, it has been proved that every equation in the stress formulation described in Chapter 2 from Eq. (2.11) to Eq. (2.14) still holds true. This demonstrates that the shear stress and resultant torque remain the same for arbitrary locations of the center of twist in cross sections whose deformation is consistent with the displacement field assumptions of the Saint Venant's torsion problem.

This statement may be further extended to heterogeneous cross sections comprised of several isotropic material regions, in different colors shown in Fig. (5.1), adopting the requirement presented by Ely and Zienkiewicz (1960). Their statement indicates that the shear stresses normal to the interface are the same in each region, which can be satisfied by making the Prandtl's stress functions share a common value along the interface separating two materials. In this way, the Prandtl's stress function stays continuous within the cross-sectional area, though its normal derivative is discontinuous across the interfaces.

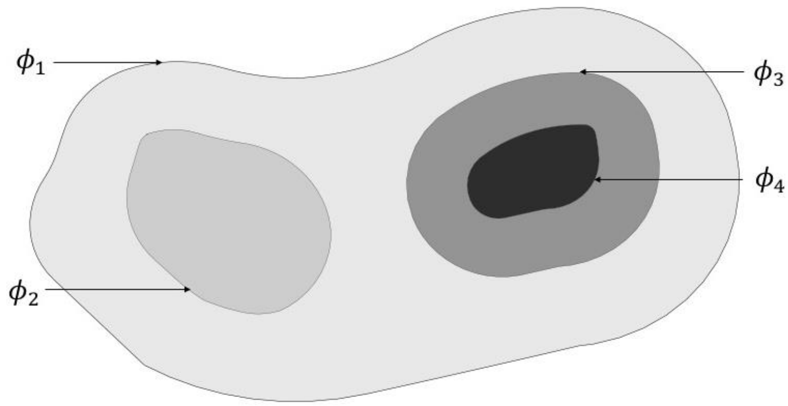

Figure 5.1. Cross section of a prismatic bar comprised of four regions with different elastic properties

If a new center of twist is defined by $x = a$ and $y = b$, where a and b are constants, then the displacements are expressed as $u = -\theta z(y-b)$, $v = \theta z(x-a)$, $w = w(x,y)$. As a consequence, the shear stress components are expressed as

$$\sigma_{xz} = G\left[\frac{\partial w}{\partial x} - \theta(y-b)\right] \qquad \sigma_{yz} = G\left[\frac{\partial w}{\partial x} + \theta(x-a)\right] \tag{5.1}$$

Differentiating these two stress expressions with y and x, respectively, yields

$$\frac{\partial \sigma_{xz}}{\partial y} - \frac{\partial \sigma_{yz}}{\partial x} = -2G\theta \tag{5.2}$$

for each individual region with its own shear modulus.

Since the Poisson's equation, Eq. (2.12), still holds true inside the outermost region bounded by the lateral surface, Fig. (5.1), and the Prandtl's stress function is conventionally set to zero on the surface ($\phi_1 = 0$), the Prandtl's stress function value on the first interfaces counting from the outside, ϕ_2 or ϕ_3, is preserved even if the center of twist is altered. We can further infer that the Prandtl's stress function on every interface including ϕ_4 would not change upon changing the center of twist location. Concomitantly, the shear stress components are not affected since they are defined as partial derivatives of the Prandtl's stress function. Thus, it is confirmed again that the summation of horizontal forces over the cross-sectional area is zero in pure torsion problems involving heterogeneous cross sections. Specifically,

$$\iint p_x \, dxdy = \iint \sigma_{xz} \, dxdy = \iint \frac{\partial \phi}{\partial y} dxdy = \int dx \int_{y_1}^{y_2} \frac{\partial \phi}{\partial y} dy$$
$$= \int [\phi]_{y_1}^{y_2} \, dx = 0 \tag{5.3}$$

where y_1 and y_2 represent the y coordinates of points located on the surface.

Similarly, it may be shown that

$$\iint \sigma_{yz} dxdy = 0 \tag{5.4}$$

As for the resultant torque summed in each region with constant ϕ along its boundary

$$T = \sum_{i=1}^{n} T_i = \sum_{i=1}^{n} \iint \left[(x-a)\sigma_{yz} - (y-b)\sigma_{xz}\right] dxdy$$
$$= \sum_{i=1}^{n} \left(\iint (x-a)\sigma_{yz} dxdy - \iint (y-b)\sigma_{xz} dxdy \right)$$
$$= \sum_{i=1}^{n} \left(-\int dy \int (x-a) \frac{\partial \phi}{\partial x} dx - \int dx \int (y-b) \frac{\partial \phi}{\partial y} dy \right) \tag{5.5}$$
$$= \sum_{i=1}^{n} \left(-\int (x-a) \, [\phi]_{x_{i1}}^{x_{i2}} dy + \iint \phi dxdy \right.$$
$$\left. - \int (y-b) \, [\phi]_{y_{i1}}^{y_{i2}} dx + \iint \phi dxdy \right)$$

where i is the index defining each distinct material region of the *n*-material cross section. Since the Prandtl's stress function is zero on the outermost boundary of the cross section, the above resultant torque expression may be simplified as

$$T = \sum_{i=1}^{n} 2 \iint \phi dxdy \tag{5.6}$$

The above derivation proves that the resultant torque calculated based on the original center of twist does not change when it is translated.

In the investigated cross sections, both concrete and structural steel are assumed to be isotropic materials with shear moduli of 1.8 Msi and 11.5 Msi respectively. Reinforced concrete columns and T-beams are analyzed under pure torsion loading, in spite of the fact that these elements are originally designed for axial compression or flexure in structural engineering applications. When the deformation is small enough, the reinforced concrete would not crack, the resultant torque is linear with the twist, Fig. (5.2). Upon cracking, the torsional resistance of concrete drops to about one-half of the uncracked member, with the remainder resisted by the reinforcement. This redistribution of internal resistance is reflected in the torque-twist curve, which illustrates continued twist at constant torque during cracking until the internal forces have been redistributed from concrete to steel reinforcement. When the section approaches the ultimate status, the concrete outside the reinforcing cage cracks and begins to spall off, no longer contributing to the torsional rigidity of the member. As Saint-Venant's torsion is a linear elasticity problem, only small deformation is allowed, in which a small angle of twist per unit length (0.0001 radian per inch) is applied and analyzed.

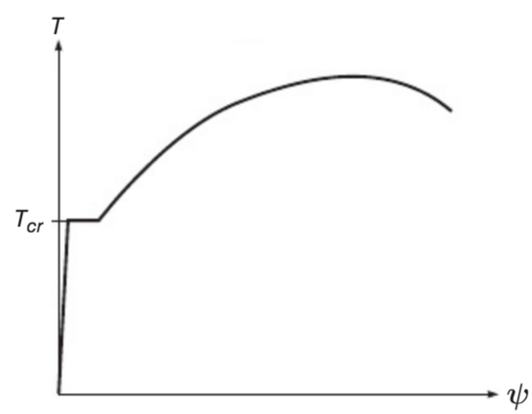

Figure 5.2. A torque-twist response of reinforced concrete members, from Design of Concrete Structures, Darwin et al. (2016).

5.2.1. Reinforced Concrete Column

The column in Fig. (5.3) is reinforced with ten No.11 rebars, whose diameter is 1.41 inch, distributed around the perimeter. This reinforced concrete column is designed to support an eccentric vertical load with an eccentricity e about the strong axis. Suppose there is a pair of torques accidentally applied to the top and bottom ends of this column. In such a scenario, the column's torsional response must be analyzed as combined loading may cause concrete to crack or lead to structural failure.

In this section, the contribution of the longitudinal rebars in resisting torsional loading is analyzed for three different cross sections reinforced with different numbers of rebars, starting with the configuration shown in Fig. (5.3), and gradually removing rebars until only four are left. The results are compared with the unreinforced homogeneous concrete cross section. The mesh density is 400 square subvolumes per square inch, and it is consistently used in all analyzed cross sections.

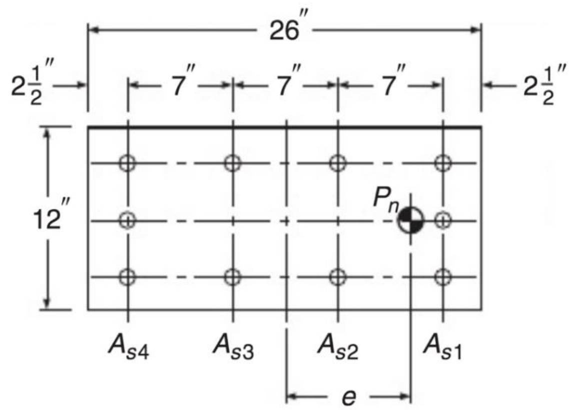

Figure 5.3. The cross section of a short column (Page 228, Design of Concrete Structures).

A) Fig. (5.4) illustrates the subvolume discretization employed in the first cross section with the largest number of rebars, including an enlarged detail of the regions containing single rebar. The cross-sectional area of the ten rebars is 5% of the rectangular column's area, or just 0.05 volume fraction of the composite member using composite materials terminology. This relatively small volume fraction is not expected to produce a large increase in the cross section's torsional rigidity, but the reinforcement's effect on the shear stress distribution and in particular the shear stresses carried by the reinforcing rods are of interest and worthy of quantification.

The shear stress resultant distribution produced by the applied angle of twist of $0.0001\ rad/in$ is shown in Fig. (5.5), and the resulting torque calculated from this distributions is $2033.1\ k \cdot in$. Hence the torsional rigidity, calculated as the ratio of torque and angle of twist, is $2.0331 \times 10^7\ k \cdot in^2$. The presence of the ten reinforcing bars alters the shear stress resultant distributions in the vicinity of the bars as well as in the concrete matrix along the cross section's periphery. This is visible along the long dimensions at the boundary where three local maximum points are evident. Because the shear modulus of the reinforcing steel bars is more than six times greater than that of concrete, substantially greater shear stress resultants are carried by the reinforcement, with the maximum shear stress of $3.22\ ksi$ occurring in the rebar at the steel/concrete interface. The shear stress rapidly decreases to a much smaller value in the concrete matrix directly adjacent to the reinforcing rebars. Nonetheless, it is continuous at the rebar/concrete interface and the transition across the interface is smooth.

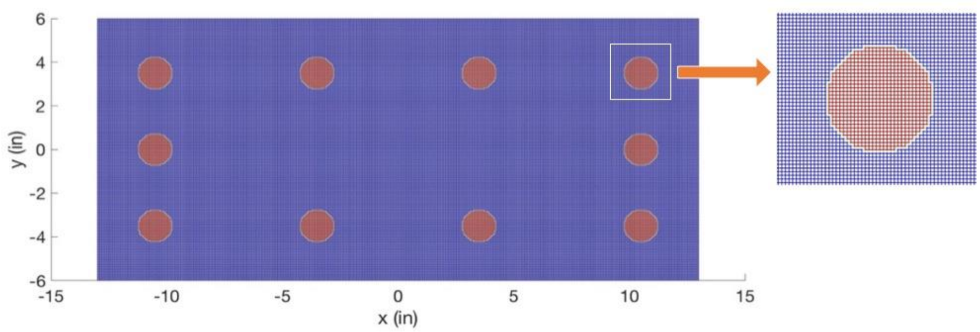

Figure 5.4. Subvolume discretization of the cross section A with ten reinforcing rebars.

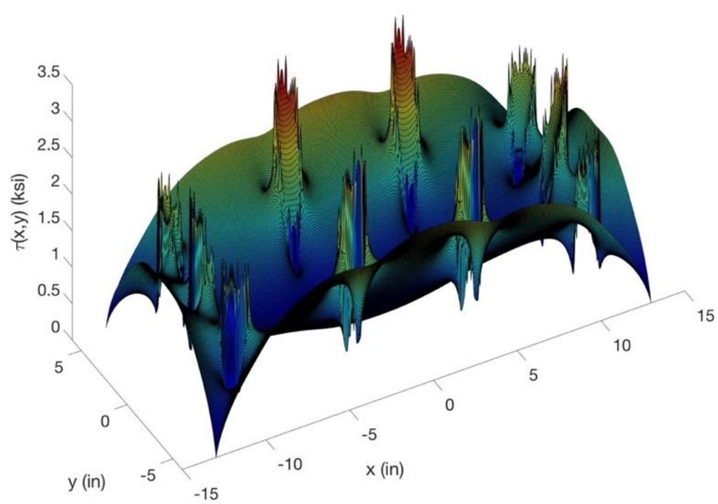

Figure 5.5. The shear stress resultant distribution in the cross section A.

B) Removing four rebars along the long dimension of the cross section and filling their area with concrete, a new rebar arrangement illustrated in Fig. (5.6) is constructed. If this new member is subjected to the same angle of twist as the cross section A, the torque calculated from the shear stress resultant distribution shown in Fig. (5.7) is $1963.8\ k \cdot in$, a small decrease from the torque carried by the cross section A. This produces the concomitantly smaller torsional rigidity of $1.9638 \times 10^7\ k \cdot in^2$. The maximum shear stress that occurs in the middle rebars along the short dimension of the cross section is $2.619\ ksi$ at the steel/concrete interface within the rebars themselves. This is substantially smaller than the maximum value $3.22\ ksi$ in the cross section A because of the difference in the locations which does not allow the shear stress to develop along the short dimension to the same extent as along the long dimension.

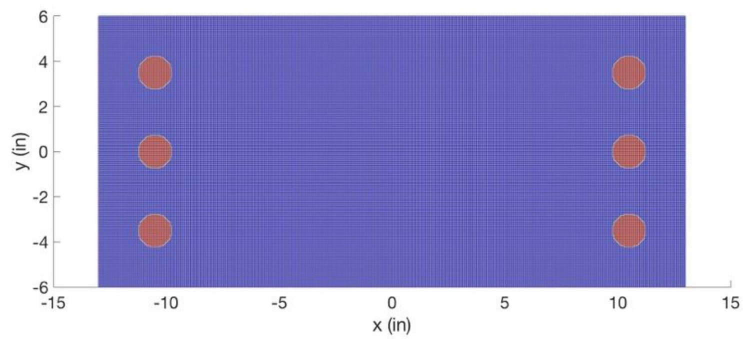

Figure 5.6. Subvolume discretization of the cross section B with six reinforcing rebars.

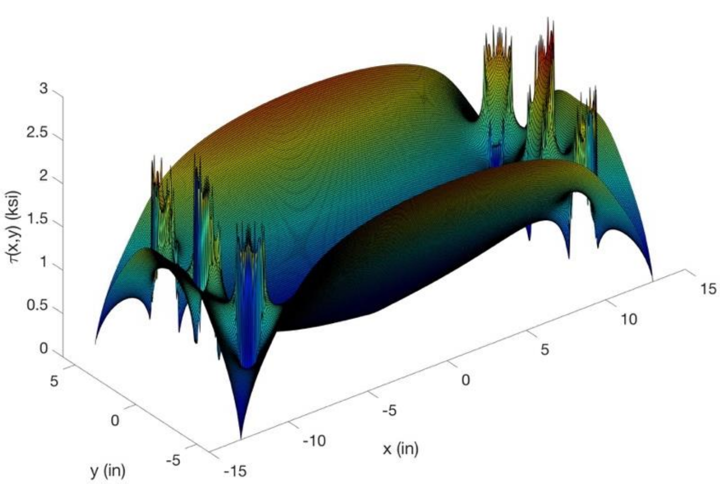

Figure 5.7. The shear stress resultant distribution in the cross section B.

C) Two more rebars are removed from the middle of the short dimension of the rebar arrangement B to produce a new cross section shown in Fig. (5.8). Subjecting this cross section to the same angle of twist as in the preceding cases, maximum shear stress of $2.1714\ ksi$ is obtained. This occurs within the four corner rebars at the steel/concrete interface observed in the shear stress distribution shown in Fig. (5.9). This maximum shear stress is again substantially smaller than the corresponding stress in the cross section B because of the four rebars' proximity to the cross-section's corners where the shear stress resultant vanishes. Hence the maximum magnitude of the shear stress resultant that may be introduced into the rebar reinforcement situated close to the corners is limited. The resulting torque calculated from the shear stress distributions at the applied angle of twist is $1942.4\ k \cdot in$ which produces the torsional rigidity of $1.9424 \times 10^7\ k \cdot in^2$, a small decrease from the rigidity of the preceding cross section.

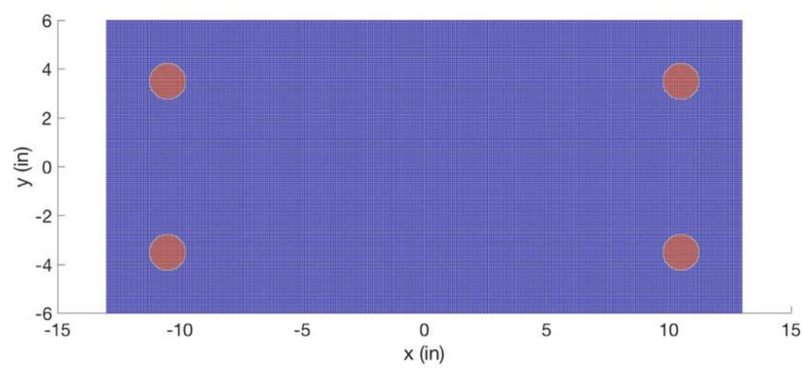

Figure 5.8. Subvolume discretization of the cross section C with four reinforcing rebars.

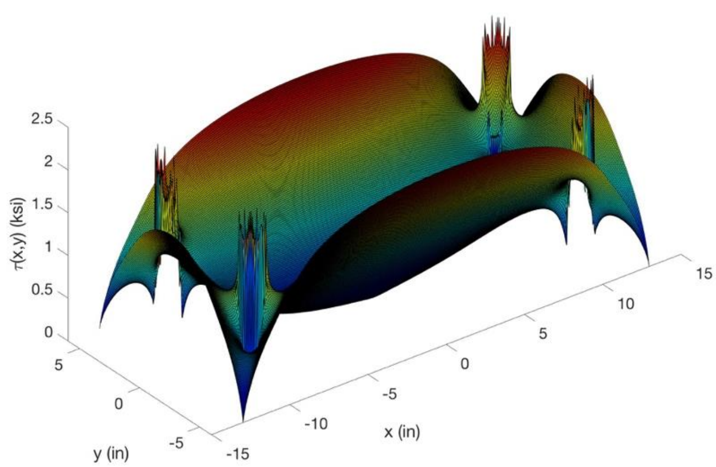

Figure 5.9. The shear stress resultant distribution in the cross section C.

D) Finally, removing the remaining four rebars to produce a homogeneous cross section, and subjecting it to the same angle of twist as before, the maximum shear stress that occurs in the middle of the longer dimension is $2.0360\ ksi$. The resultant torque calculated from the shear stress distribution shown in Fig. (5.10) is $1909.1\ k \cdot in$, yielding the torsional rigidity of $1.9091 \times 10^7\ k \cdot in^2$. This configuration provides a reference against which the results presented in the foregoing may be gauged as discussed in the sequel with regard to the effect of rebar reinforcement of the torsional rigidity of the composite cross section and the concomitant stress distributions.

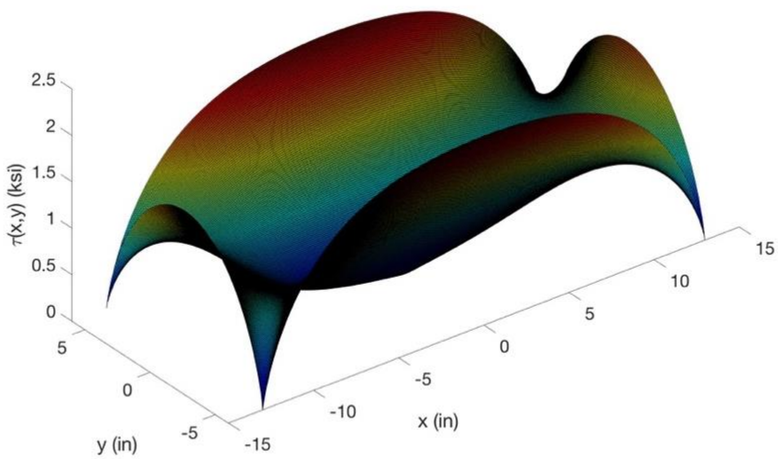

Figure 5.10. The shear stress resultant distribution in the cross section D.

The finite-volume analysis of the four rectangular cross sections with various degrees of rebar reinforcement indicates that the torsional rigidity is enhanced at most by 6.5% when ten longitudinal rebars are employed that take up 5% of the entire cross-sectional area. This is consistent with the known micromechanics reinforcement principles which indicate an initially linear improvement in effective properties of composite materials under shear loading transverse to the reinforcement direction when the reinforcement volume fraction is small. To obtain greater torsional rigidity enhancement, greater reinforcement volume fraction are required. Alternatively, from a structural reinforcement perspective, the small increase in the torsional rigidity implies the importance of the use of stirrups in resisting torsional deformation.

As previously mentioned, reinforced concrete columns are typically designed to resist bending and related shear deformation due to lateral loading. Under such external loading, they carry substantial internal loads due to their high stiffness even at low volume fractions. Hence the stresses that arise in the reinforcement itself are important in the design of these structural components. The additional shear stresses that may arise in the rebars themselves under torsional loading (due to eccentricity, for example) may contribute to failure in the presence of additional stresses cause by primary loads, and hence must be calculated. The results presented in this section indicate that the placement of rebars is important. Specifically, in order to maximize the rebars' contribution to torsional resistance, they must be placed at the outer periphery of the long dimension of the analyzed cross section. Such placement will maximize the shear stresses that the rebars carry, thereby producing the greatest torsional rigidity enhancement.

5.2.2. Reinforced Concrete T-beam

The reinforced concrete T-beam shown in Fig. (5.11) contains two No. 11 rebars near the bottom of the web. Its primary purpose is to increase the beam's bending stiffness in order to prevent large tensile deformations in the concrete matrix. The concrete cover is 2.5-inch thick for the two rebars, which are symmetric about the centerline of the web. Mesh density of 100 subvolumes per square inch is employed to analyze this T-beam cross section, Fig. (5.12).

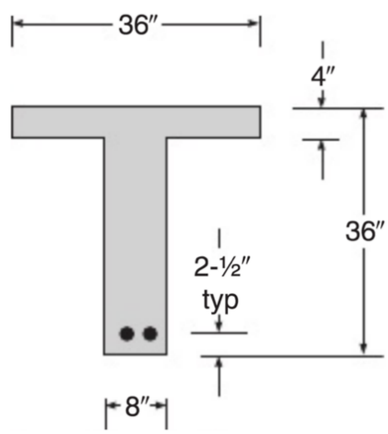

Figure 5.11. The cross section of a T-beam (Page 126, Design of Concrete Structures).

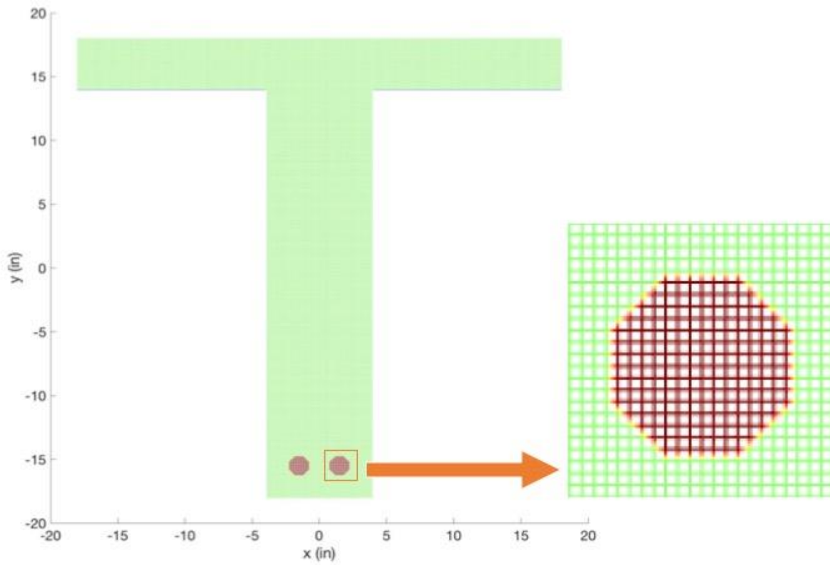

Figure 5.12. The mesh of the cross section of a T-beam.

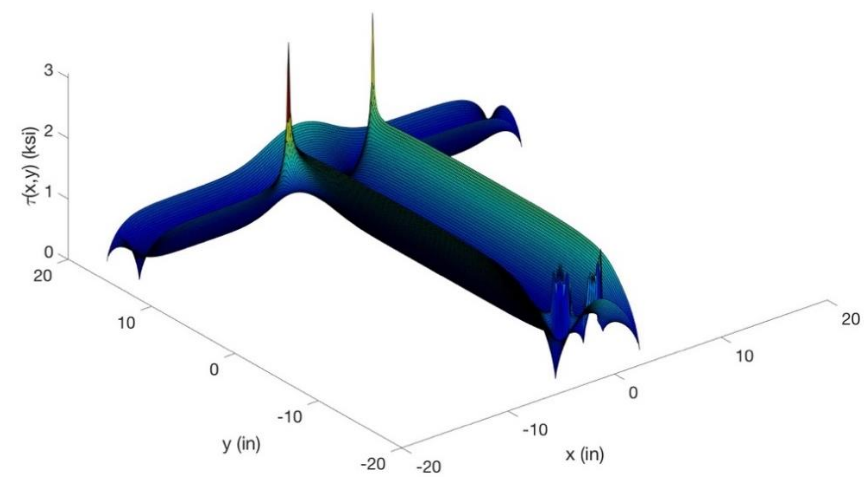

Figure 5.13. The shear stress of the reinforced concrete T-beam cross section.

Fig. (5.13) illustrates the shear stress resultant distribution in the reinforced T-beam's cross section produced by the angle of twist of $0.0001\ rad/in$. The maximum shear stress which occurs at the re-entrant corners is $3.0698\ ksi$ for the employed level of subvolume discretization. Because the stress field is singular in this location, further subvolume discretization would produce a larger magnitude without fundamentally altering the stress distribution features elsewhere. Moreover, as the reinforcing rebars are close to the external bottom corners of the web, the shear stress that develops in the rebars is relatively small. The rebars' presence only alters the shear stress field locally upon comparison with the shear stress distribution in the unreinforced T-beam cross section illustrated in Fig. (5.14), with the maximum shear stress at the re-entrant corners unchanged. The reinforced T-beam carries a torque of $1080.9\ k \cdot in$ when subjected to the aforementioned angle of twist. Thus, the torsional rigidity is calculated as $1.0809 \times 10^7\ k \cdot in^2$. For comparison, the unreinforced T-beam carries the torque of $1.0745\ k \cdot in$, which results in the torsional rigidity of $1.0745 \times 10^7\ k \cdot in^2$. As a result, the torsional rigidity is improved just by 0.60% in the presence of the two longitudinal rebars, which make up 0.78% of the entire cross-sectional area. These two longitudinal rebars clearly do not resist torsional deformation to any significant extent, which reflects the need for additional web reinforcement.

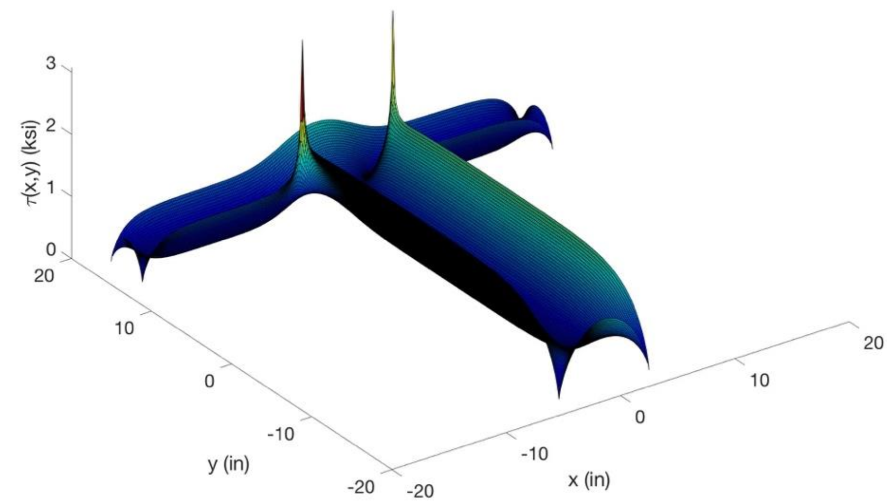

Figure 5.14. The shear stress resultant distribution in the plain concrete T-beam cross section.

5.3. Reinforcement of Closed Cross Sections

The center of twist of a composite orthotropic cross section coincides with its geometric centroid if its layout and material property are symmetric about two orthogonal axes. In this section, we focus on rectangular box-beams with various levels of reinforcement by external wraps. It is obvious that the center of twist of such rectangular composite box-beams should be at the geometric centroid, which is exactly in the middle of these cross sections.

We first analyze the torsional behavior of a plain concrete box-beam which serves as a reference. Then we strengthen it by wrapping layers other than the concrete around its outer boundary, and finally evaluate the enhancement of the torsional resistance capacity due to the wraps. One hundred square subvolumes per square inch are employed consistent with the preceding studies.

5.3.1. Homogeneous Concrete Box-Beam

The reference concrete beam has the wall thickness of 2 inches and outer dimensions of 12×12 inches, Fig. (5.16). The applied angle of twist of $0.0001\ rad/in$ produces maximum shear stress of $2.1472\ ksi$ at the re-entrant corners of the box-beam, Fig. (5.17). For the given angle of twist, this member carries a torque of $399.4035\ k \cdot in$, resulting in the torsional rigidity of $3.9940 \times 10^6\ k \cdot in^2$.

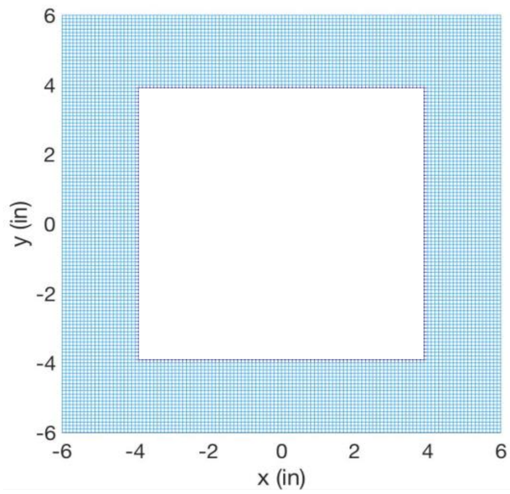

Figure 5.16. Subvolume discretization of the cross section of a plain concrete box-beam.

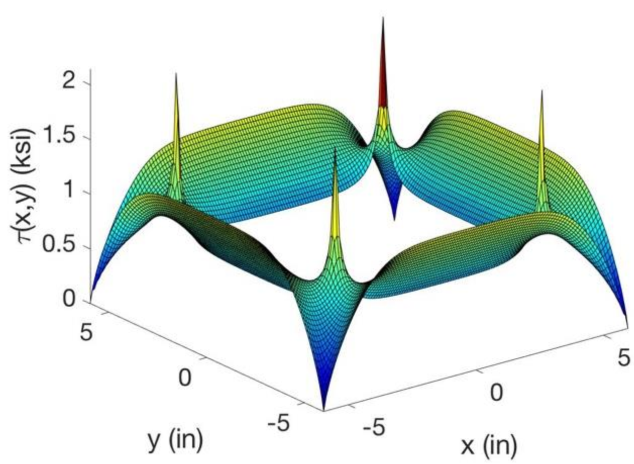

Figure 5.17. The shear stress distribution in the reference homogeneous concrete box-beam.

5.3.2. Glass/Epoxy-Wrapped Concrete Box-Beam

Two sets of layers of unidirectional glass/epoxy composite are wrapped around the outermost surface of the reference concrete box-beam, Fig. (5.18). The orientation of the glass reinforcement in the inner layers is along the axis of the box-beam whereas the outer layers have fibers oriented perpendicular to the beam's axis. The shear moduli of the innermost layer in the two orthogonal planes containing the longitudinal axis are therefore the same along the entire composite wrap, with $G_{xz} = G_{yz} = G_A$, where G_A, is called axial shear modulus in the composite materials community. In contrast, the shear moduli of the outer wrap are different, with the differences depending on whether horizontally or vertically oriented layers are considered. For the horizontally oriented outer layers, $G_{xz} = G_A$, whereas $G_{yz} = G_T$ with G_T called transverse shear modulus. For vertically oriented layers the roles are reversed and $G_{xz} = G_T$ while $G_{yz} = G_A$. The volume fraction of the glass fibers in both sets of layers is 0.60 (60% by volume) and the thickness of each set comprised of 60 layers each is 0.3 inches based on the standard pre-impregnated tape thickness of 0.005 used to lay up the wrap.

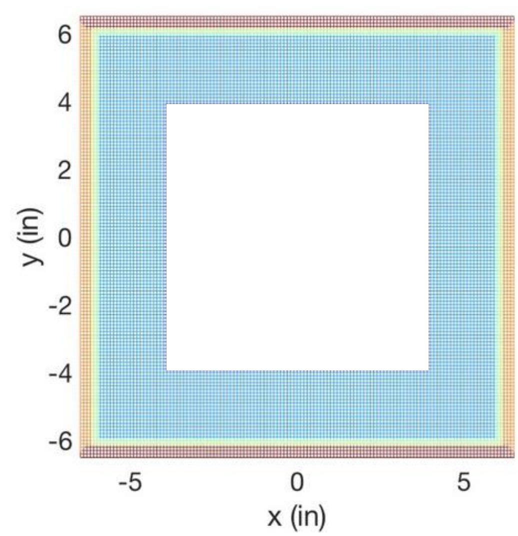

Figure 5.18. Subvolume discretization of the cross section of a glass/epoxy-concrete box-beam.

The two shear moduli of the glass/epoxy composite wraps were determined using the locally-exact homogenization theory originally developed by Drago and Pindera (2007) and further extended by Wang and Pindera (2016). Using the Young's modulus of 10 Msi

and shear modulus of 4 Msi for the reinforcing glass fibers, and Young's modulus of 0.5 Msi and shear modulus of 0.19 Msi for the epoxy matrix, the axial and transverse shear moduli for the glass/epoxy composite with fiber volume fraction of 0.60 are calculated as 0.6828 Msi and 0.4897 Msi. These values were employed in the finite-volume analysis of the composite box-beam.

The shear stress resultant distribution in the composite box-beam due to the applied angle of twist of $0.0001\ rad/in$ are shown in Fig. (5.19). This shear stress distribution produces a torque of $474.3387\ k\cdot in$ which yields the torsional rigidity of $4.7434\times 10^{6}\ k\cdot in^{2}$. This torsional rigidity is 1.19 times that of the reference homogeneous concrete box-beam, due to the larger cross-sectional area given that the composite wrap has much smaller shear moduli than that of concrete at 1.8 Msi. Hence the shear stress carried by the composite wraps in pure torsion is much smaller than that of the concrete itself. It is interesting, however, to note that the maximum shear stress at the re-entrant corners of the composite box-beam is 2.2204 ksi which is a small increase relative to the reference box-beam. Composite wrap reinforcement in the manner considered in this example is more effective in increasing the bending stiffness of the box-beam than torsional stiffness.

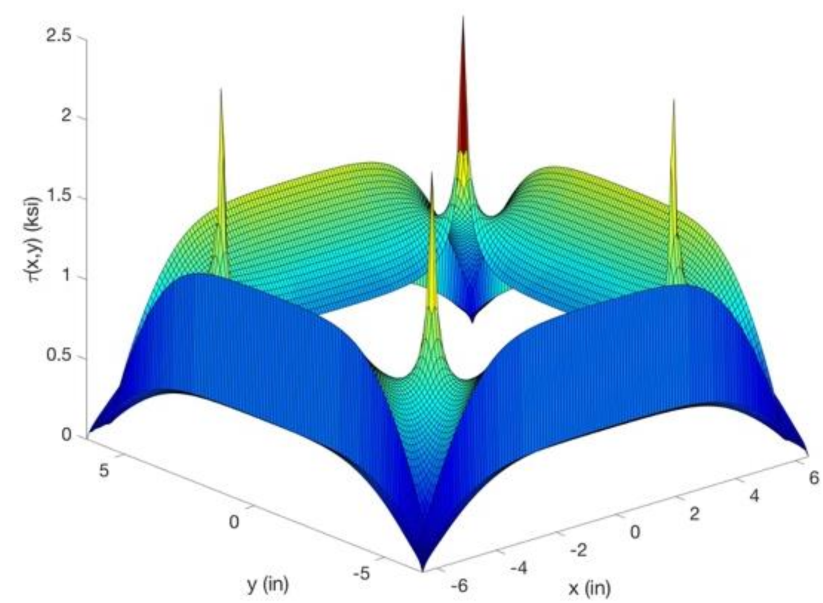

Figure 5.19. The shear stress distribution in the glass/epoxy wrapped concrete box-beam.

5.3.3. Steel-Wrapped Concrete Box-Beam

The above example indicates that in order to effectively increase the torsional rigidity of a concrete box-beam using a wrap, the stiffness of the wrap should be larger than that of concrete. Hence a steel cage may be a good candidate. Thin steel panels may be more effective with concrete than reinforcing rebars, especially when they are wrapped completely around the box-beam to produce an integrated, continuously reinforced structure. This is the configuration analyzed in this section using the finite-volume method. Fig. (5.20) illustrates such a concrete box-beam reinforced with four thin steel panels joined at the corners and tightly adhering to the entire outer surface of the beam, thereby encasing it completely.

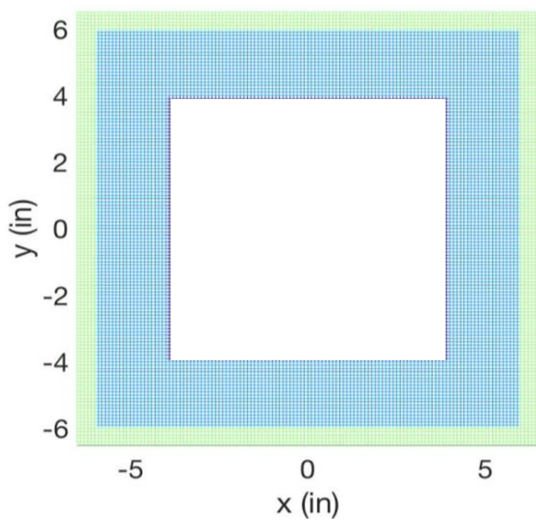

Figure 5.20. Subvolume discretization of the cross section of a steel case-reinforced concrete box-beam.

Fig. (5.21) illustrates the shear stress resultant distribution in the steel case-reinforced concrete box-beam produced by the applied angle of twist of $0.0001\ rad/in$. At this level of subvolume discretization, the maximum shear stress no longer occurs at the re-entrant corners where singular-like behavior continues to be observed with comparable magnitudes as in the preceding two cases. Indeed, the maximum shear stress resultant is $8.6988\ ksi$ and this occurs in the middle of the outer steel layer. As observed, the steel layer carries large magnitudes of the shear stress resultant which contributes to the majority of the resultant torque. Specifically, the torque calculated from the shear stress distributions is $1{,}588.9\ k \cdot in$ for the applied angle of twist. Therefore, the resulting torsional rigidity is $1.5889 \times 10^7\ k \cdot in^2$, which is 3.98 times that of the reference homogeneous concrete box-beam.

It is worthwhile to point out that the shear stress resultant distribution varies continuously within the steel and concrete regions, with a visible jump at the steel/concrete interface due to the large jump in the shear moduli of the two materials.

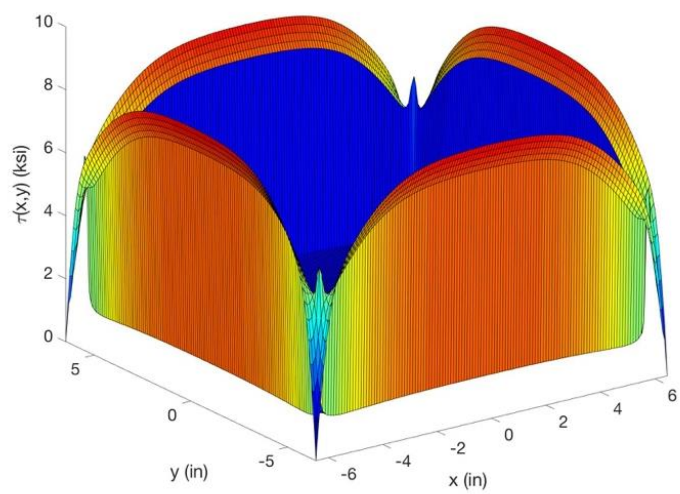

Figure 5.21. The shear stress resultant distribution in the steel case-concrete box-beam.

5.3.4. Glass/Epoxy and Steel-Wrapped Concrete Box-Beam

As stated before, the finite-volume method has been developed specifically for applications involving both heterogeneous materials and structures. Hence the method may be used to analyze the effect of reinforcement of a box-beam by any number of different materials arranged in many different ways. Therefore, it is also possible to use both the glass/epoxy and steel layers wrapped around the concrete box-beam as reinforcement without additional difficulty or changes in the actual coding of the equations underpinning the theory. It is sufficient to simply assign different elastic moduli to different subvolumes that belong to a region characterized by a set of shear moduli through the material assignment matrix. Any number of different materials may be employed to produce cross sections with arbitrary and exotic microstructures.

To demonstrate this capability, Fig. (5.22) illustrates the cross section of the analyzed composite box-beam that combines the reinforcement of the two previous examples. The steel layer placed on the outside is 0.5-inch thick. The glass/epoxy layers between the concrete and steel regions of the composite beam contain two fiber orientations as before. That is, the fiber orientation of the inner glass/epoxy layers is along the box-beam's longitudinal axis, producing the same shear moduli in both in-plane directions. In the outer glass/epoxy plies the fibers are perpendicular to this axis, forming a square pattern resulting in two distinct shear moduli in the orthogonal planes containing the beam's longitudinal axis.

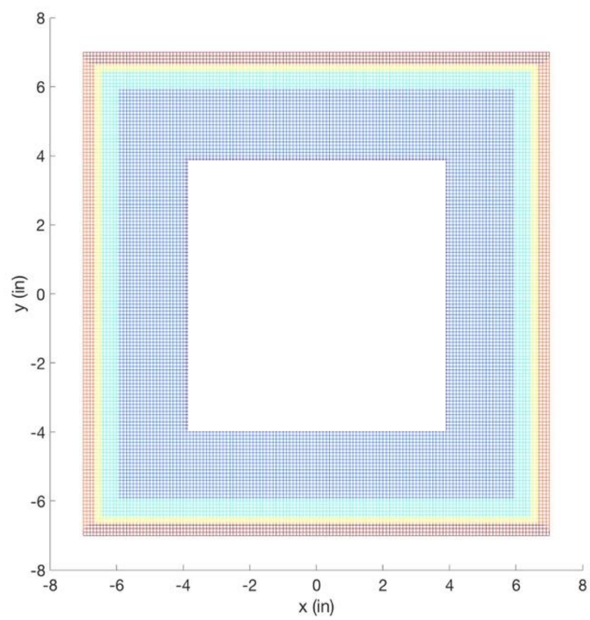

Figure 5.22. Subvolume discretization of the cross section of a glass/epoxy and steel-wrapped concrete box-beam.

Fig. (5.23) illustrates the shear stress resultant distribution produced by the applied angle of twist of $0.0001\ rad/in$. As in the preceding case, the maximum shear stress occurs in the middle of the outer steel layer and its magnitude of 8.6171 ksi is slightly lower. In contrast, the torque carried by the composite beam is higher, $1686.6\ k \cdot in$, yielding the concomitantly larger torsional rigidity of $1.6866 \times 10^7\ k \cdot in^2$, which is 4.22 times that of the reference homogeneous concrete box-beam. The majority of the torque is carried by the outer steel layer.

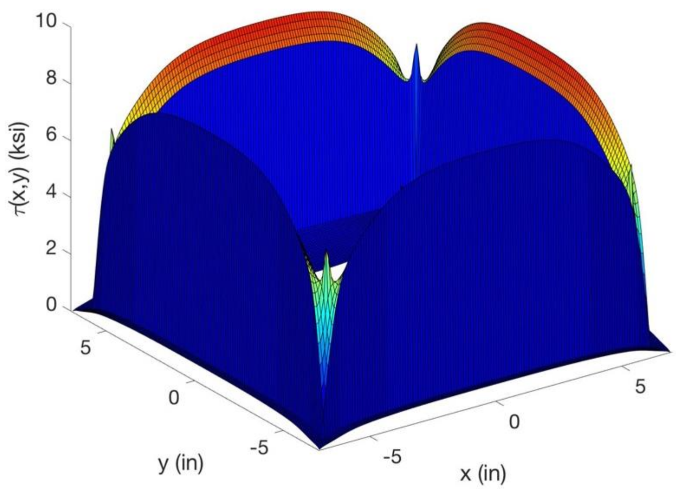

Figure 5.23. The shear stress resultant distribution in the glass/epoxy and steel-wrapped concrete box-beam.

5.4. Summary and Discussion

The examples presented in this chapter demonstrate that the finite-volume method has a great potential for solving Saint-Venant's torsion problems of composite beams comprised of both isotropic and orthotropic regions with high efficiency. Convergence studies of the resultant torque and force equilibrium have not been presented in this chapter. Instead, the focus has been on validating the applicability of the finite-volume technique in applications involving composite cross sections. With this in mind, structural engineering applications have been chosen involving both open and closed cross sections of beams of different cross sections containing discontinuous and continuous reinforcement. Based on the chosen examples, several conclusions listed below are summarized.

Longitudinal rebars do increase the torsional rigidity of concrete structures yet not in a remarkable manner. Web reinforcement is thus necessary to support shear stress and torque to a greater extent in structures subjected to torsional loading. Therefore, it would be a useful effort to construct a three-dimensional version of the finite-volume method to analyze torsional resistance in the presence of web reinforcement in the future. Although some composite materials such as glass/epoxy may not have large shear modulus relative to the concrete itself, they can still increase the torsional rigidity because of additional cross-sectional area. The advantage of composite wraps lies in the low weight gain of the beams due to the additional layers that are relatively easy to add.

In contrast, thin steel layers have a substantially greater impact in strengthening box-beams under torsional loading by increasing the torsional rigidity almost three times in the considered examples. Therefore, wrapping a concrete member with a thin steel layer is an efficient way to resist twist. Actually, wrapping a concrete layer first with thin steel and then glass/epoxy is a win-win strategy, since steel is able to carry a tremendous portion of torque for the entire beam and glass/epoxy can protect the steel from corrosion in the open air.

Chapter 6

6. Contributions and Conclusions

6.1. Summary and Conclusions

Under combined loading, the different deformation modes of structural elements are typically analyzed separately. One of the distinct deformation modes produced by pure torsion, characterized by twisting of a structural element with a constant cross section, plays an important role in structural engineering design. Not only can applied torque produce twisting, but shear stress distributions created by bending deformations can also result in torsional effects. Torsion introduces additional shearing in the structural component's cross section, which may potentially produce failure in concrete structures or damage their serviceability. Therefore, the torsion problem requires critical analysis to ensure stability and safety of structural designs, and to determine whether necessary torsional reinforcement should be taken in order to avoid structural collapse or loss of integrity.

Saint Venant developed an exact elasticity solution framework to torsion problems of prismatic members that reduces a seemingly three-dimensional problem to a two-dimensional one involving just one governing differential equation based on the constancy of the twisting deformation pattern along the members' longitudinal axis. This framework is universally called the semi-inverse method. Torsion problems were defined by the Laplace equation subject to Neumann-type boundary condition which ensured that the lateral surface of the member was traction free. Prandtl subsequently reformulated the torsion problem by introducing a stress function that satisfied equilibrium equations and showed that this stress function must satisfy Poisson's equation. Specifically, Prandtl's stress function satisfies exactly the third equilibrium and simplifies the traction-free boundary condition to a Dirichlet type where the function has a constant value on the cross section's lateral boundary. Due to the pioneering work of Saint Venant and Prandtl, Timoshenko (1970), Boresi and Schmidt (2003), Ugural and Fenster (2003), Sadd (2005) and many others who followed the semi-inverse solution approach made the torsion of prismatic homogenous isotropic bars well established. The developed analytical techniques are limited to a relatively small number of cross sections mainly composed of isotropic materials. It is only recently that prismatic bars made of anisotropic materials and composite cross sections have been studied analytically, cf., Mushkhelishvilli (1975), Savoia andTullini (1993), Swanson (1998) and Chen (2004). For complicated cross sections, however, numerical techniques must be employed.

Three popular numerical methods, namely the finite-difference method (Ely and Zienkiewicz, 1960), the boundary element method (Sapountzkis and Mokos, 2003) and the finite-element method, have been employed to solve torsion problems of composite cross sections. Each class of these methods has its own advantages and disadvantages. The finite-element method is the most widely used technique in the solution of torsion problems based on the warping or stress function approaches, cf., Xiao et al. (1998), Li et al. (2000) and Saygun (2007).

An alternative to the solution of structural problems, including the Saint Venant's torsion problem, is the finite-volume method originally developed for fluid mechanics boundary-value problems, cf. Lveque (2002), Versteeg and Malalasekera (2007). Satisfaction of the governing equilibrium field equations within subvolumes of the discretized domain in an integral sense is its key feature. Three versions of the finite-volume technique can be identified in the analysis of solid mechanics problems, as discussed by Cavalcante et al. (2012). The first two approaches, cell-centered and cell-vertex finite-volume technique, were motivated by the established finite-volume technique for fluid mechanics and elements of the finite-element method. The third approach evolved independently to deal explicitly with heterogenous microstructures, Bansal and Pindera (2003, 2005, 2006) and Zhong et al. (2004). This version employs explicit displacement field approximation within individual subvolumes, and follows an elasticity-based approach in satisfying interfacial displacement and traction continuity conditions in a surface-averaged sense. The main objective and contribution of this thesis were to demonstrate the utility of the finite-volume approach in the solution of Saint Venant's torsion problems of prismatic bars of arbitrary cross section and composition.

In this thesis, the finite-volume theory developed by Pindera and co-workers has been extended to the solution of Saint Venant's torsion problems, assessed, validated and applied to the analysis of cross sections employed in structural engineering problems. The displacement-based formulation has been employed in constructing the solution methodology. In the developed finite-volume approach, subvolumes that make up any shape cross sections are rectangular with their own elastic properties. Each subvolume is in a state of force equilibrium and satisfies traction and displacement continuity with its adjacent neighbors in a surface-averaged sense. In order to provide a standard for comparison and validation of the developed finite-volume method, finite-difference solutions have also been developed using both displacement-based and stress-based formulations. These approaches are well-suited for the solution of Saint Venant's torsion problems involving homogenous linear elastic isotropic material cross sections, and exhibit quick convergence behavior, but are not easily extended to cross sections composed of complicated heterogeneous regions containing different materials. The finite-volume and finite-difference methods have been implemented in MATLAB computer codes capable of generating displacement and shear stress fields, as well as torsional rigidity of the analyzed cross sections.

Both the finite-volume and finite-difference techniques have been validated against the elasticity solution for homogenous isotropic rectangular cross section bars of any aspect ratio based on an infinite Fourier series representation of the Prandtl's stress function. It has been demonstrated that the convergence of the finite-volume predictions with mesh refinement to the elasticity results for a wide range of cross section aspect ratios is slower relative to the finite-difference method, while the differences between the finite-volume and elasticity results are still within an acceptable range. It has also been demonstrated that at any level of subvolume discretization of the analyzed cross section, the horizontal and vertical shear forces produced by the torsion-induced shear stresses vanish, ensuring that the analyzed member is indeed subjected to pure torsion. This is a distinct feature of the finite-volume method which also applies to torsion problems.

The convergence and accuracy of the finite-volume method relative to exact elasticity solutions were also demonstrated for composite cross sections made up of two symmetrically joined rectangular regions filled with different materials. The developed finite-volume technique yielded results which were close to those calculated by the exact elasticity solution of Mushkhelishvilli. The finite-volume method was also demonstrated to be more accurate than some of the finite-element method results available in the literature. The validation of the developed finite-volume method's accuracy in the analysis of both homogeneous and composite cross sections relative to exact elasticity solutions confirms the method's applicability in structural engineering applications.

Prandtl's stress function reformulation also enables an analogy to be drawn between torsion problems and a deflection of a pressurized flexible membrane over an opening of the same shape as the bar's cross section. The analogy demonstrates the physical significance of the mathematical formulation of torsion problems and a means of obtaining approximate solutions. This analogy has been assessed in this thesis for torsion of thin-walled structures for which closed-form results for torsional rigidity are available based on the approximation of torsional shear stresses that develop in thin-walled cross sections. Three typical homogenous cross sections employed in structural engineering, namely T-beams, channel-beams and box-beams, have been analyzed and the accuracy of the membrane analogy was assessed for each cross section using the corresponding results generated by the finite-difference and finite-volume methods. The membrane analogy was shown to be an efficient and accurate tool in estimating the torsional rigidity of open-section members such as T-beams and channel-beams with good accuracy relative to the finite-difference and finite-volume calculations. The torsional rigidity of the box-beam cross section was underestimated by the membrane analogy for larger wall thickness, but the difference became increasingly smaller as the walls became thinner.

The shear stress fields employed in the membrane analogy applied to thin-walled structures, that are used in the torsional rigidity calculations, are approximations that neglect the effect of junctions between different cross section members and the corresponding re-entrant corners that give rise to large stress concentrations which exhibit singular-like behavior. This local singular-like behavior was captured with good accuracy by the finite-volume and finite difference methods upon comparison with an exact elasticity solution, but is outside of the membrane analogy's predictive capability. For closed-section structures like the box-beam, the presence of several such corners affects the torsional rigidity calculations for sufficiently thick walls based on the membrane analogy, leading to the observed differences. These differences are rooted in the substantial differences in the shear stress resultant distributions in the four corner regions. Outside of the stress concentration regions, and regions where the cross-section's members terminate, the shear stress fields predicted by the membrane analogy are generally accurate. Specifically, the non-singular maximum shear stress resultants predicted by the membrane analogy were accurate at the midpoints of the T-beam's web and the three walls of the channel-beam, whereas the maximum shear stress difference decreased with decreasing wall thickness at the midpoint of the T-beam's flange but did not vanish even for the thinnest wall configurations. The difference was affected by the web/flange junction that produced shear stress fields with large deviations from the membrane analogy's approximation.

In summary, the membrane analogy has its place in the design of thin-walled structures subjected to torsion because of easy and simple calculations which yield good estimates of torsional rigidity and non-singular maximum shear stress resultants in the absence of exact elasticity solutions. However, caution must be exercised when identifying potential failure initiation sites produced by large stress concentrations, particularly at re-entrant corners created by junctions of two adjacent members of the cross section.

Finally, the finite-volume method's strength lies in its superior ability to handle heterogeneous microstructures. This strength was demonstrated in this thesis for composite cross sections with isotropic or orthotropic materials in the form of discontinuous and continuous reinforcement of concrete T- beam and box-beam cross sections. This thesis lays the foundation for the implementation of the finite-volume method in a large range of applications involving the design of composite structural elements with complex heterogeneous microstructures.

6.2. Proposed Future Work

Functionally graded materials became popular in recent years, including application to torsion problems. Cross sections comprised of functionally graded regions are easily amenable to analysis using the developed finite-volume method. Xu et al. (2010) and Darilmaz (2017) have generated results for such cross sections subjected to torsional loading using analytic and finite-element methods, providing abundant data for future comparison.

In this thesis, composite cross sections reinforced by circular rebars were mimicked using discretization based on square subvolumes. This is not as efficient as using quadrilateral subvolumes employed in the parametric version of the finite-volume method. The results generated in this thesis provide the foundation for further extension of the developed finite-volume approach to the solution of torsion problems based on the parametric version of the theory. This will facilitate the analysis of torsion problems involving circular, elliptical and other cross sections reinforced by differently shaped materials.

Determination of the shear center of prismatic bars is also essential for thin-walled structure design since resultant loading through this center creates pure bending, thereby avoiding additional torsion that may produce the phenomena of wall buckling. For instance, Natori (2001) computed the shear center of thin-walled cross sections by the finite-element method. The determination of the shear center of composite cross sections is still a largely unexplored area. A three-dimensional version of the finite-volume theory for structural engineering applications is required to accomplish this and this will be pursued in the future.

Appendix A

The coefficients in Eq. (2.36), *Surface-averaged tractions expression with respect to surface-averaged displacements*:

$$L_{11} = C_{66}\frac{4}{h_\beta} - \frac{3C_{66}^2}{C_{66}h_\beta + C_{55}\frac{h_\beta^3}{l_\gamma^2}},\ L_{12} = C_{66}\frac{2}{h_\beta} - \frac{3C_{66}^2}{C_{66}h_\beta + C_{55}\frac{h_\beta^3}{l_\gamma^2}},$$

$$L_{13} = -\frac{3C_{55}C_{66}}{C_{66}\frac{l_\gamma^2}{h_\beta} + C_{55}h_\beta},\ L_{14} = -\frac{3C_{55}C_{66}}{C_{66}\frac{l_\gamma^2}{h_\beta} + C_{55}h_\beta}$$

$$L_{21} = C_{66}\frac{2}{h_\beta} - \frac{3C_{66}^2}{C_{66}h_\beta + C_{55}\frac{h_\beta^3}{l_\gamma^2}},\ L_{22} = C_{66}\frac{4}{h_\beta} - \frac{3C_{66}^2}{C_{66}h_\beta + C_{55}\frac{h_\beta^3}{l_\gamma^2}},$$

$$L_{23} = -\frac{3C_{55}C_{66}}{C_{66}\frac{l_\gamma^2}{h_\beta} + C_{55}h_\beta},\ L_{24} = -\frac{3C_{55}C_{66}}{C_{66}\frac{l_\gamma^2}{h_\beta} + C_{55}h_\beta}$$

$$L_{31} = -\frac{3C_{55}C_{66}}{C_{66}l_\gamma + C_{55}\frac{h_\beta^2}{l_\gamma}},\ L_{32} = -\frac{3C_{55}C_{66}}{C_{66}l_\gamma + C_{55}\frac{h_\beta^2}{l_\gamma}},$$

$$L_{33} = C_{55}\frac{4}{l_\gamma} - \frac{3C_{55}^2}{C_{66}\frac{l_\gamma^3}{h_\beta^2} + C_{55}l_\gamma},\ L_{34} = C_{55}\frac{2}{l_\gamma} - \frac{3C_{55}^2}{C_{66}\frac{l_\gamma^3}{h_\beta^2} + C_{55}l_\gamma}$$

$$L_{41} - \frac{3C_{55}C_{66}}{C_{66}l_\gamma + C_{55}\frac{h_\beta^2}{l_\gamma}},\ L_{42} - \frac{3C_{55}C_{66}}{C_{66}l_\gamma + C_{55}\frac{h_\beta^2}{l_\gamma}},$$

$$L_{43} = C_{55}\frac{2}{l_\gamma} - \frac{3C_{55}^2}{C_{66}\frac{l_\gamma^3}{h_\beta^2} + C_{55}l_\gamma},\ L_{44} = C_{55}\frac{4}{l_\gamma} - \frac{3C_{55}^2}{C_{66}\frac{l_\gamma^3}{h_\beta^2} + C_{55}l_\gamma}$$

Appendix B

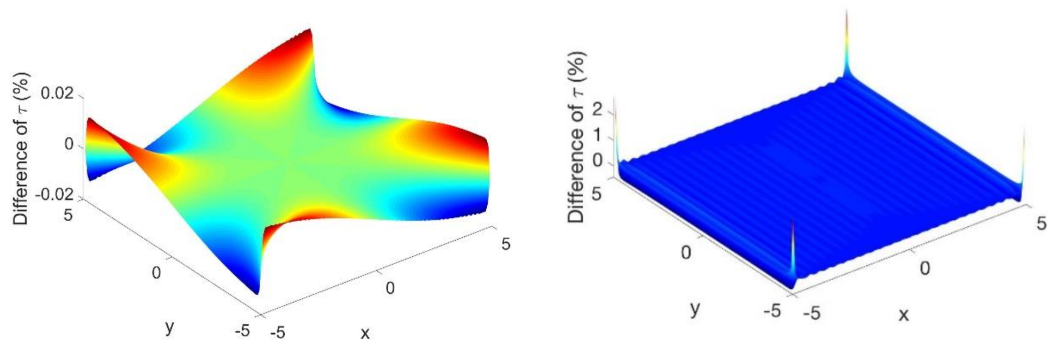

a/b = 1

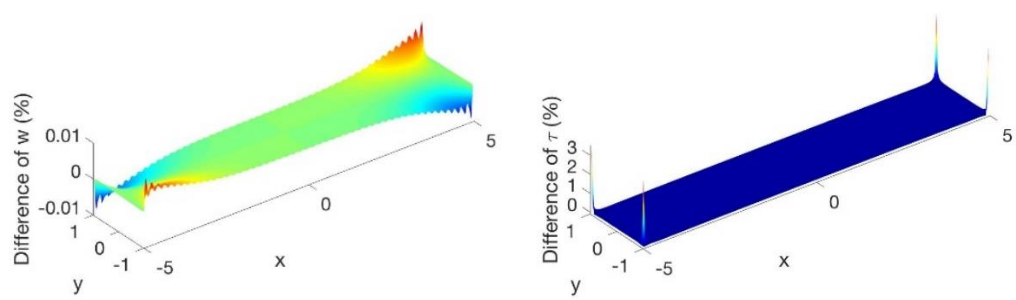

a/b = 5

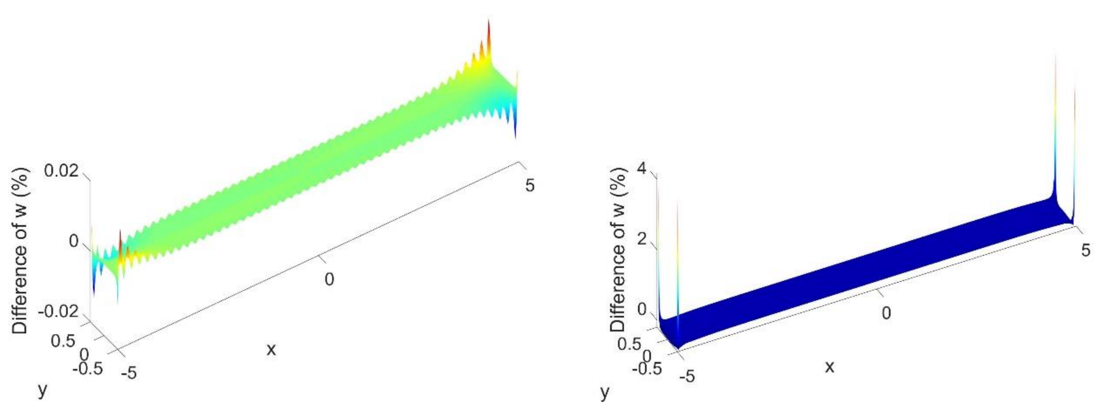

a/b = 10

Figure 3.6. Full-field difference of displacement and shear stress (FDM vs Elasticity).

References

Aboudi, J., Pindera, M. J., & Arnold, S. M. (1999). Higher-order theory for functionally graded materials. Composites Part B: Engineering, 30(8), 777-832.

Aboudi, J., Pindera, M. J., & Arnold, S. M. (2003). Higher-order theory for periodic multiphase materials with inelastic phases. International Journal of Plasticity, 19(6), 805-847.

Bansal, Y., & Pindera, M. J. (2003). Efficient reformulation of the thermoelastic higher-order theory for functionally graded materials. Journal of Thermal Stresses, 26(11-12), 1055-1092.

Bansal, Y., & Pindera, M. J. (2005). A second look at the higher-order theory for periodic multiphase materials. Journal of applied mechanics, 72(2), 177-195.

Bansal, Y., & Pindera, M. J. (2006). Finite-volume direct averaging micromechanics of heterogeneous materials with elastic–plastic phases. International Journal of Plasticity, 22(5), 775-825.

Barretta, R. (2012). On the relative position of twist and shear centres in the orthotropic and fiberwise homogeneous Saint–Venant beam theory. International Journal of Solids and Structures, 49(21), 3038-3046.

Beheshti, A. (2018). A numerical analysis of Saint-Venant torsion in strain-gradient bars. European Journal of Mechanics-A/Solids, 70, 181-190.

Birman, V., & Byrd, L. W. (2007). Modeling and analysis of functionally graded materials and structures. Applied mechanics reviews, 60(5), 195-216.

Boresi, A. P., Schmidt, R. J., & Sidebottom, O. M. (1985). Advanced mechanics of materials (Vol. 6). New York et al.: Wiley.

Bufler, H. (1971). Theory of elasticity of a multilayered medium. Journal of Elasticity, 1(2), 125-143.

Buryachenko, V. (2007). Micromechanics of heterogeneous materials. Springer Science & Business Media.

Cardiff, P., & Demirdžić, I. (2018). Thirty years of the finite volume method for solid mechanics. arXiv preprint arXiv:1810.02105.

Cavalcante, M. A. A. (2006). Modelling of the Transient Thermo-Mechanical Behavior of Composite Material Structures by the Finite-Volume Theory. MS Thesis, Federal University of Alagoas, Maceio, Alagoas, Brazil.

Cavalcante, M. A. A., Marques, S. P. C. and Pindera, M.-J. (2007a). Parametric formulation of the finite-volume theory for functionally graded materials. Part I: Analysis. Journal of Applied Mechanics, 74 (5), 935-945.

Cavalcante, M. A. A., Marques, S. P. C. and Pindera, M.-J. (2007b). Parametric formulation of the finite-volume theory for functionally graded materials. Part II: Numerical Results. Journal of Applied Mechanics, 74 (5), 946-957.

Cavalcante, M. A., Pindera, M. J., & Khatam, H. (2012). Finite-volume micromechanics of periodic materials: past, present and future. Composites Part B: Engineering, 43(6), 2521-2543.

Chan, Y. S., Paulino, G. H., & Fannjiang, A. C. (2008). Gradient elasticity theory for mode III fracture in functionally graded materials—part II: crack parallel to the material gradation. Journal of Applied Mechanics, 75(6), 061015.

Charalambakis, N., & Murat, F. (2006). Approximation by finite elements, existence and uniqueness for a model of stratified thermoviscoplastic materials. Ricerche di matematica, 55(2), 11-58.

Chatzigeorgiou, G., Charalambakis, N., & Murat, F. (2008). Homogenization problems of a hollow cylinder made of elastic materials with discontinuous properties. International Journal of solids and structures, 45(18-19), 5165-5180.

Chen, T., & Wei, C. J. (2005). Saint-Venant torsion of anisotropic shafts: theoretical frameworks, extremal bounds and affine transformations. Quarterly Journal of Mechanics and Applied Mathematics, 58(2), 269-287.

Chen, T., Benveniste, Y., & Chuang, P. C. (2002). Exact solutions in torsion of composite bars: thickly coated neutral inhomogeneities and composite cylinder assemblages. Proceedings of the Royal Society of London. Series A: Mathematical, Physical and Engineering Sciences, 458(2023), 1719-1759

Darılmaz, K., Orakdöğen, E., & Girgin, K. (2018). Saint-Venant torsion of arbitrarily shaped orthotropic composite or FGM sections by a hybrid finite element approach. Acta Mechanica, 229(3), 1387-1398.

Ely, J. F., & Zienkiewicz, O. C. (1960). Torsion of compound bars—A relaxation solution. International Journal of Mechanical Sciences, 1(4), 356-365.

Gattu, M., Khatam, H., Drago, A. S., & Pindera, M. J. (2008). Parametric finite-volume micromechanics of uniaxial continuously-reinforced periodic materials with elastic phases. Journal of Engineering Materials and Technology, 130(3), 031015.

Hashin, Z., & Rosen, B. W. (1964). The elastic moduli of fiber-reinforced materials. Journal of applied mechanics, 31(2), 223-232.

Heinrich, S. M. (1996). Membrane analogy for Saint-Venant torsion: New results. Journal of engineering mechanics, 122(11), 1110-1112.

Horgan, C. O. (2007). On the torsion of functionally graded anisotropic linearly elastic bars. IMA Journal of Applied Mathematics, 72(5), 556-562.

Jog, C. S., & Mokashi, I. S. (2014). A finite element method for the Saint-Venant torsion and bending problems for prismatic beams. Computers & Structures, 135, 62-72.

Karimi, M., Atrian, A., Ghassemi, A., & Vahabi, M. (2017). Torsion analysis of a hollow cylinder with an orthotropic coating weakened by multiple cracks. Theoretical and Applied Fracture Mechanics, 90, 110-121.

Katori, H. (2001). Consideration of the problem of shearing and torsion of thin-walled beams with arbitrary cross-section. Thin-walled structures, 39(8), 671-684.

Khatam, H. and Pindera, M.-J. (2009a). Thermo-elastic moduli of lamellar composites with wavy architectures. Composites: Part B, 40 (1), 50-64.

Khatam, H. and Pindera, M.-J. (2009b). Parametric finite-volume micromechanics of periodic materials with elastoplastic phases. International Journal of Plasticity, 25 (7), 1386-1411.

LeVeque, R. J. (2002). Finite volume methods for hyperbolic problems (Vol. 31). Cambridge university press.

Li, L. Y., & Easterbrook, D. (2014). Free torsion of thin-walled structural members of open-and closed-sections. Applied Mathematics and Mechanics, 35(1), 25-32.

Li, Z., Ko, J. M., & Ni, Y. Q. (2000). Torsional rigidity of reinforced concrete bars with arbitrary sectional shape. Finite Elements in Analysis and Design, 35(4), 349-361.

Malalasekera, W., & Versteeg, H. K. (2007). An introduction to computational fluid dynamics: the finite volume method. PEARSON Prentice Hall.

Muskhelishvili, N. I. (1963). Some basic problems of the mathematical theory of elasticity. Noordhoff, Groningen, 17404.

Pindera, M. J. (1991). Local/global stiffness matrix formulation for composite materials and structures. Composites Engineering, 1(2), 69-83.

Purnomo, J., Tjong, W. F., Wijaya, W. C., & Putra, J. S. (2018). Displacement and Stress Function-based Linear and Quadratic Triangular Elements for Saint-Venant Torsional Problems. Civil Engineering Dimension, 20(2), 70-77.

Romano, G., Barretta, A., & Barretta, R. (2012). On torsion and shear of Saint-Venant beams. European Journal of Mechanics-A/Solids, 35, 47-60.

Rongqiao, X., Jiansheng, H., & Weiqiu, C. (2010). Saint-Venant torsion of orthotropic bars with inhomogeneous rectangular cross section. Composite Structures, 92(6), 1449-1457.

Sadd, M. H. (2009). Elasticity: theory, applications, and numerics. Academic Press.

Sapountzakis, E. J. (2001). Nonuniform torsion of multi-material composite bars by the boundary element method. Computers & structures, 79(32), 2805-2816.

Sapountzakis, E. J., & Mokos, V. G. (2003). Warping shear stresses in nonuniform torsion of composite bars by BEM. Computer Methods in Applied Mechanics and Engineering, 192(39-40), 4337-4353.

Savoia, M., & Tullini, N. (1993). Torsional response of inhomogeneous and multilayered composite beams. Composite Structures, 25(1-4), 587-594.

Saygun, A., Omurtag, M. H., Orakdogen, E., Girgin, K., Kucukarslan, S., & Darilmaz, K. (2007). A Simplified solution of the torsional rigidity of the composite beams by using FEM. Advances in Structural Engineering, 10(5), 467-473.

Sinclair, G. B. (2004). Stress singularities in classical elasticity–I: Removal, interpretation, and analysis. Applied Mechanics Reviews, 57(4), 251-298.

Suquet, P. M. (1985). Elements of homogenization for inelastic solid mechanics, Homogenization Techniques for Composite Media. Lecture notes in physics, 272, 193.

Swanson, S. R. (1998). Torsion of laminated rectangular rods. Composite structures, 42(1), 23-31.

Teimoori, H., Faal, R. T., & Das, R. (2016). Saint-Venant torsion analysis of bars with rectangular cross-section and effective coating layers. Applied Mathematics and Mechanics, 37(2), 237-252.

Timoshenko, S. P., & Goodier, J. (2011). Theory of elasticity.

Troyani, N., Pérez, A., Gomes, C., Baíz, P., & Da Fonseca, Z. (2009). Selective finite element refinement in torsional problems based on the membrane analogy. Finite Elements in Analysis and Design, 45(8-9), 547-554.

Tsai, M. J., & Chen, T. (2012). Saint-Venant’s torsion of composite shafts reinforced with arbitrarily or periodically dispersed coated fibers. International Journal of Engineering Science, 51, 104-116.

Tsiatas, G. C., & Katsikadelis, J. T. (2011). A new microstructure-dependent Saint–Venant torsion model based on a modified couple stress theory. European Journal of Mechanics-A/Solids, 30(5), 741-747.

Ugural, A. C., & Fenster, S. K. (2003). Advanced strength and applied elasticity. Pearson education.

Xiao, Q. Z., Karihaloo, B. L., Li, Z. R., & Williams, F. W. (1999). An improved hybrid-stress element approach to torsion of shafts. Computers & structures, 71(5), 535-563.

Zhong, Y., Bansal, Y., & Pindera, M. J. (2004). Efficient reformulation of the thermal higher-order theory for fgms with locally variable conductivity. International Journal of Computational Engineering Science, 5(04), 795-831.